LIGHT MANAGEMENT IN SILICON NANOSTRUCTURES FOR PHOTOVOLTAICS

by

Baomin Wang

B. S., Tsinghua University, China, 2010

Submitted to the Graduate Faculty of

the Swanson School of Engineering in partial fulfillment

of the requirements for the degree of

Doctor of Philosophy

University of Pittsburgh

2016

UNIVERSITY OF PITTSBURGH

SWANSON SCHOOL OF ENGINEERING

This dissertation was presented

by

Baomin Wang

It was defended on

January 29th, 2016

and approved by

Paul W. Leu, Ph.D., Assistant Professor, Department of Industrial Engineering

Bopaya Bidanda, Ph.D., Ernest E. Roth Professor, Department of Industrial Engineering

Kevin P. Chen, Ph.D., Paul E. Lego Professor, Department of Electrical and Computer Engineering

Young Jae Chun, Ph.D., Assistant Professor, Department of Industrial Engineering

Dissertation Director: Paul W. Leu, Ph.D., Assistant Professor, Department of Industrial Engineering

LIGHT MANAGEMENT IN SILICON NANOSTRUCTURES FOR PHOTOVOLTAICS

Baomin Wang, PhD

University of Pittsburgh, 2016

The main challenge with the use of silicon for photovoltaics is that silicon is not a strong absorber of sunlight in the near-infrared region. Conventional silicon photovoltaics are thus typically of thicknesses 200 to 300 μm to ensure the absorption of most sunlight. However, single crystalline silicon solar cells require expensive manufacturing methods. So current solar cell technology is not as competitive as that of traditional energy sources. To promote and increase the silicon solar cell capacity, costs need to drop below \$1/W. Increasing absorption of light in the absorber layers is critical issue for achieving high efficiency silicon solar cells.

Various light trapping methods have been developed, experimentally and computationally. Light trapping with sub-wavelength nanostructures involves coupling light into localized resonant modes and guided resonance modes in active region to increase absorption. Nanophotonic light trapping strategies have used structuring of the silicon itself or patterning of dielectric materials on front and back of silicon.

In order to continue developing cheap and high efficiency silicon solar cells, we studied several anti-reflection and light trapping structures with lower cost and higher absorption. First of all, tapered nanocone structure was proposed and studied and then fabricated via Bosch process. Secondly, high refractive index nanosphere scheme was investigated as a light trapping strategy which does not create new surface or interface and is easy to fabricate. Then inverse woodpile and woodpile photonic crystal structures were studied and proven to have superior light trapping ability due to the ability to engineer the photonic density of states.

Finally, ultrathin silicon was fabricated via wet etching method, and then high refractive index nanosphere layers were coated and the power conversion efficiency was increased by 26.5%. Furthermore, metal nanomesh was used as front contact to substitute traditional indium tin oxide, and the power conversion efficiency was increased by 53% due to high haze factor and lower sheet resistance of the metal nanomesh. More importantly, with the metal nanomesh as front contact, the ultrathin silicon solar cells showed superior flexibility.

TABLE OF CONTENTS

LIST OF TABLES

LIST OF FIGURES

PREFACE

This work is dedicated to my family.

I would like to thank my advisor Prof. Paul W. Leu for giving me the opportunity to pursue my goal as a Ph.D. student. As his first student, I am grateful for how he has supported and encouraged me over the years. I thank our research funding sources, National Science Foundation and Mascaro Center for Sustainable Innovation. I am thankful to other professors at University of Pittsburgh: my committee members Prof. Kevin P. Chen, Prof. Young Jae Chun, and Prof. Bopaya Bidanda for their insightful comments on my research, and Prof. Bopaya Bidanda as department chair has been always supporting me in life and study through the years; Prof. Jung-Kun Lee and Prof. Di Gao for giving me the access to the equipment in their labs, without which I could not finish my experiments.

I am thankful for the various staff at University of Pittsburgh: in the PINSE Nanoscale Fabrication and Characterization Facility: Dr. Susheng Tan, Mike McDonld and Matthew for the trainings; in the Center for Simulation and Modeling, Kim F. Wong for the help to my computation; Albert Stewart for helping with the scanning electron microscope. I also would like to thank the staff in Nanofabrication Facility at CMU: Chris Bowman, Carsen Kline, Norman Gottron, and Matthew Moneck for the equipment training and useful discussions.

I have had the pleasure to work in Dr. Leu's research group, and I am thankful to the lab members for helping set up equipment and experiments: Miriam, Erica, Donnie, Brendan, Dalton, Rodney, Arpit, Cheng, Ibrahim, Mohamed, Lincoln and Imrul. And my special thank goes to another lab coworker Tongchuan who works most intimately with me over the years and has lot of joys and fun to work with and talk to, and we also have had plenty of useful discussions over each other's research on a daily basis. In addition, he has been a good friend in life here.

One of the most enjoyable things for me here is playing basketball which helps me relax and get vented and fit so that I have better spirit to devote myself to my research, so I want to give my appreciation to all the friends who play on my team on a weekly basis: Ran Zhang, Ning Chen, Jiangyue Zhu, Zhen Zeng, Rui Chen, Zhibo Zeng, Le Yang and Ke Luo.

I also would like to thank many friends I have kept in touch with from Tsinghua and high school over the years, Huijuan Lu, Yaru Li, Xiang Li, Shuai Li, Yunyi Wang, Xiaohao Yang, Fuquan Tu, Long Lin, and Peijun Guo. It is always pleasant to talk with them and see them from now and then.

I also would like to express gratitude to my dear friend Yvonne Guo, my former roommate, who I talk to on a daily basis. It is a great pleasure to know her and have her around since she has been always supporting me and believing in me.

Above all else, I am deepest thankful to my family: Mom, Dad, my older brother, my sister-in-law, my niece and my nephew for their love and patience, and they are the most important part of my life and my biggest support to pursue dreams. Especially, I would like to thank my Dad because it is him who leads me to this path and achieve this accomplishment.

1.0 INTRODUCTION

1.1 SOLAR ENERGY AND SOLAR CELLS

The population of the world is increasing rapidly over the past decades, as a result, there has been a steep increase in global demand for energy. The demand was over 524 quadrillion British thermal units (BTU) in 2010, and it is expected to increase to 630 BTU in 2020 and 820 BTU in 2040 [1] which is mostly obtained from fossil fuels. Thus, other problems coming with extravagant energy consumption are environmental issues. The global energy related CO_2 emissions reached a historic high of 31.6 gigatonnes in 2012, regarded as a suspected cause of serious climate change [2]. Renewable energy is an important approach to solve this situation. Exploiting sustainable, environment friendly and cost-effective energy resource becomes highest priority. Geothermal, wind, hydrowater, bioenergy and solar energy are all renewable energy source. Solar energy is the most attractive one due to the omnipresence and abundance across the whole globe. The sun delivers 23000 TW of energy to the earth per year, which is much higher than annual global energy consumption. More importantly, the energy conversion from solar light is free of pollution, noise and green house emission. As shown in Figure 1, solar energy has much bigger potential than any other renewable energies [3].

Solar energy can be transformed into electricity either thermodynamically [4] or electronically. The first method is indirect since the solar thermal energy, focused in specially designed optical collectors, is used in steam turbines or other heat engines to produce electricity. The other method instead converts the solar energy directly into electricity by opto-electronic devices, called solar cells. Particularly, after decades of research after the first solar battery developed at Bell Labs [5], so efficient production of electricity by different types of solar cells

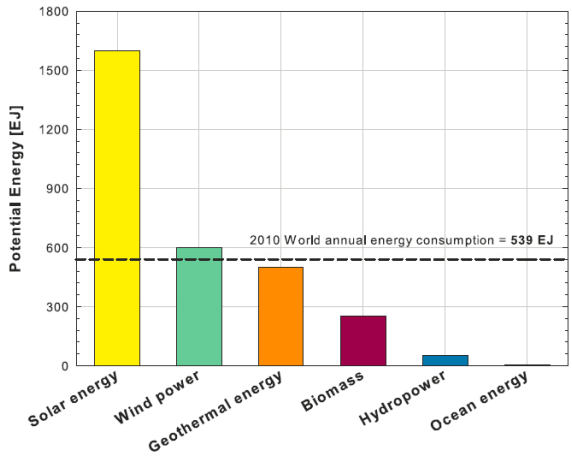

Figure 1: Potential energy production per year of various types of renewable energies. The horizontal line indicates the world energy consumption in 2010.

is current available. Even photovoltaic technologies might be applied anywhere needed, if only the six black circles area in Figure 2 are covered in solar panels of only 8% efficiency, 18 TW of energy could be produced which probably could meet the global electricity demand [6]. It should be noted that many solar cell designs which exceed 8% conversion efficiency have been produced. So solar energy and solar cells technology is the best way to solve energy crisis problem.

1.2 MILESTONES IN SOLAR CELLS

In 1839, Alexandre-Edmond Becquered discovered the photovoltaic effect [7]. His experiments demonstrated that light could introduce current when the interfaces of two liquids was illuminated by sunlight or ultraviolet light. After that, lots of other experiments were setup, including solid equipments with copper or selenium as light sensitive materials [8–10], as a result, plenty of patents were issued about how to set up photovoltaic devices. However, the modern photovoltaic time began after Teal and Little [11] adapted the Czochralski pro-

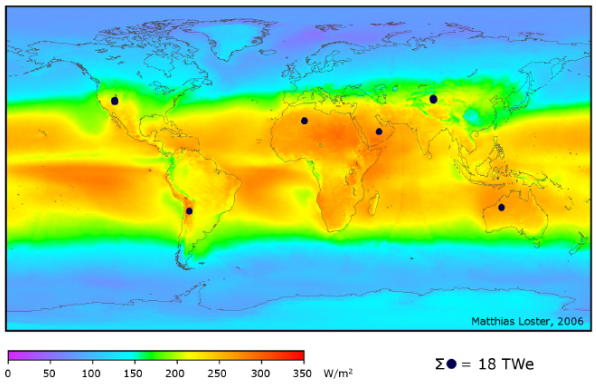

Figure 2: Total primary power density supply from sunlight. The colors show a three year average of solar irradiance.

cess [12] to obtain germanium or silicon crystalline wafers in 1948. Based on lots of previous work on photovoltaics, Fuller, Pearson and Chapin from Bell Labs fabricated the first p-n homojunction silicon solar cell [13] in 1954. In the same year, Reynold et al [14]. fabricated the first CdS based heterojunction photovoltaic device. In 1970, Zhores Alferovs team made the first effective $GaAs$ heterostructure solar cell for space applications. And the first amorphous silicon solar cell with 2.4% conversion efficiency was reported in 1976 by Carlson and Wronski [15]. Entering 1980s, the concept of tandem solar cells, quaternary compounds and novel ternary were introduced to increase the conversion efficiency further. University of Delarware made $CuZnS/CdS$ solar cell with 10% conversion efficiency [16]. Greens team [17] from University of New South Wales reported a solar cell based on silicon wafer breaking 20% conversion efficiency with application of passivation and light management in 1985. In 1990s, lots of different designs of tandem double and triple junctions devices were fabricated based on amorphous silicon, nano-crystalline silicon and alloys [18]. The dye sensiteized solar cell (DSSC) was invented by O'Regan and Gratzel [19] in 1991 aiming for low cost photochemical production. After 2000, solar cell techniques have been improved significantly and lots of the techniques are commercial available. The total solar photovoltaic capacity is approaching 100 GW milestone recently.

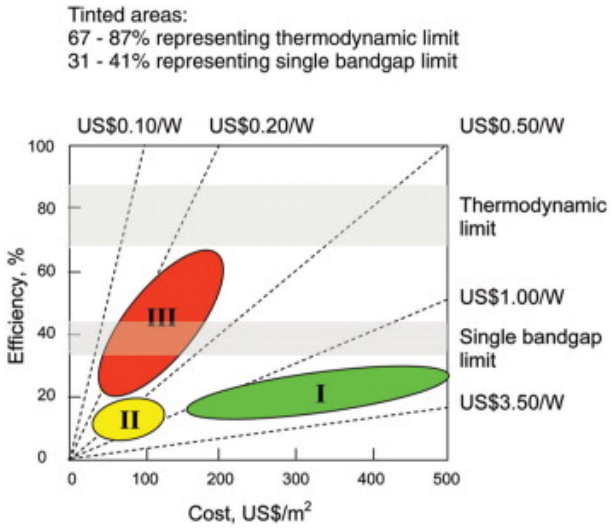

Figure 3: Efficiency and cost projections for first (I), second (II), and third generation (III) PV technologies (wafer-based, thin films, and advanced thin films, respectively).

1.3 CURRENT SOLAR CELLS RESEARCH AND STATUS IN QUO

For current solar cell research, the solar cell technology is typically classified in: first generation, second generation and third generation. Figure 3 shows the efficiency and cost projections for all three generation solar cells [20].

The first generation includes cells consisting of Silicon or Germanium that are doped with Phosphorus and Boron in a pn-junction. Typical examples are like passivated emitter with rear locally diffused cell, panasonic HIT cell and multi-crystalline cell. This generation is dominating the commercial market.

Second generation solar cells are usually called thin-film solar cells because when compared to crystalline silicon based cells they are made from layers of semiconductor materials only a few micrometers thick. The combination of using less material and lower cost manufacturing processes allow the manufacturers of solar panels made from this type of technology to produce and sell panels at a much lower cost. There are basically three types of solar cells that are considered into this category, amorphous silicon, and two that are made from non-

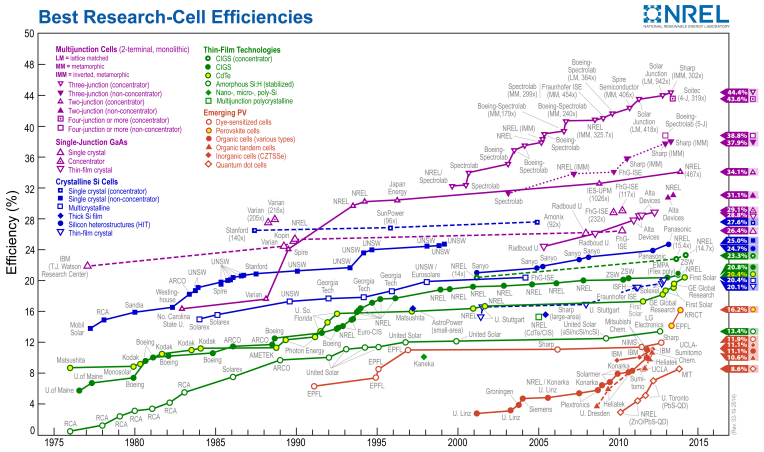

Figure 4: Reported timeline of solar cell energy conversion efficiencies (from National Renewable Energy Laboratory (USA)).

silicon materials namely cadmium telluride ($CdTe$), and copper indium gallium diselenide ($CIGS$). And organic solar cells and $DSSC$ solar cells are other alternative technologies for low cost solar energy devices.

The third generation solar cells intend to combine the high efficiency and low costs. This new generation of solar cells are being made from variety of new materials besides silicon, including nanotubes, silicon wires, solar inks using conventional printing press technologies, organic dyes, and conductive plastics. Enormous researches have been done on third generation solar cells, but it's still in the lab stage. Solar cells have been developed rapidly since invented, and various of types solar cells have been fabricated and made commercial available, in Figure 4 the research record on solar cell efficiency since 1975 is shown.

1.4 SILICON THIN FILM SOLAR CELLS

Silicon is the second most abundant natural element on Earth but is rarely found in its elemental form. Usually extracted from its oxides and silicate, it can be industrially prepared in crystalline or amorphous form. While silicon has an almost-ideal band gap for single p-n

junction photovoltaics, its infrared absorption is poor. Silicon has absorption lengths > 6 µm for photons in the infrared region (energy $E < 1.7$ eV) and absorption lengths > 200 µm for photons with wavelength > 1000 nm ($E < 1.2$ eV). Typical single-crystalline silicon photovoltaics are thus usually several hundred microns thick to absorb sunlight effectively. These silicon solar cells require costly manufacturing processes such as purification, crystallization, and wafer slicing in order to ensure that generated carriers are collected efficiently.

The amorphous silicon (a-Si) is deposited on thin films with chemical vapor deposition (CVD) or plasma assisted CVD methods. a-Si differs from crystalline silicon for its disordered lattice with intrinsically imperfections which serve as recombination centers, thus decreasing the electron and hole diffusion length compare to crystalline silicon. The introduction of hydrogen atoms during the deposition can partially improve this problem. The hydrogenated amorphous silicon (a-Si:H), behaves similarly to a direct band gap semiconductor with band gap varying 1.6 eV to 1.9 eV depending on deposition recipes. The defects density is 2 or 3 orders of magnitude higher in doped a-Si:H due to the thermal equilibrium between dopants and defect creation, so a higher recombination rate for charge carriers. Therefore a conventional p-n junction, as used in c-Si solar cells will not work adequately because most charge carrier are lost during the silicon layers before they can be extracted from solar cells. However, a p-i-n junction can solve this problem. The sandwiched intrinsic layer between doped layers serve as the main light absorber. The doped layers induce electric fields separate and push carrier toward the terminals to be collected. Figure 5 shows typical p-i-n junction and n-i-p junction solar cells with front transparent conductive oxide (TCO), junction, back TCO and back reflector.

Diluting silane or disilane with increasing flows of hydrogen and spanning regimes of high pressure and high power result in the formation of a crystalline phase within the amorphous tissue called hydrogenated nano-crystalline silicon (nc-Si:H) with a band gap close to that of crystalline silicon. Nc-Si:H shows higher absorption in infrared part of the spectrum and higher electron mobility with fewer defects. It's also less sensitive to the light induced degradation. By now, the highest reported and certified nc-Si:H single junction cell efficiency is 10.1% [21].

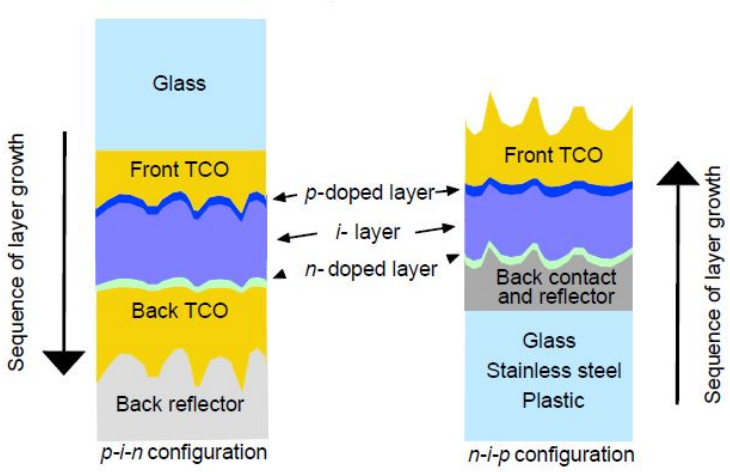

Figure 5: Schematics of thin-film silicon solar cells in the p-i-n and n-i-p configuration.

2.0 COMPUTATION METHODOLOGY

2.1 SOLAR SPECTRUM

The solar spectral irradiance is shown as the green line in Figure 6 provides the power density used to calculate the conversion efficiency of a solar cell. The emitted photon flux density per unit area per unit solid angle per unit frequency which is derived later on from the Bose-Einstein Distribution and the density of states is

$$b_\Omega(E)dEd\Omega = \frac{2n^2}{h^3c^2}\frac{E^2}{\exp\left(\frac{E-\mu}{kT}\right)-1}dEd\Omega \tag{2.1}$$

And irradiance or power flux density $I(E)$ can be calcualted as,

$$\boxed{I(E) = Eb_s(E)} \tag{2.2}$$

where $b_s(E)$ is the photon flux density. $\int_0^\infty I(E)dE = 1,000$ W/m^2 for AM1.5 Global which is used for testing flat panels.

2.2 OPTICAL PROPERTIES SIMULATION METHODS

Simulation methods are vital to the development of next-generation solar cells such as plasmonic, organic, nanophotonic, and semiconductor nanostructure solar cells. Simulations are predictive of material properties such that they may be used to rapidly screen new materials and understand experimental results.

Most simulations have focused on analyzing and improving the solar absorption of the silicon active region. Nanostructured solar cells have feature sizes smaller than the wavelengths

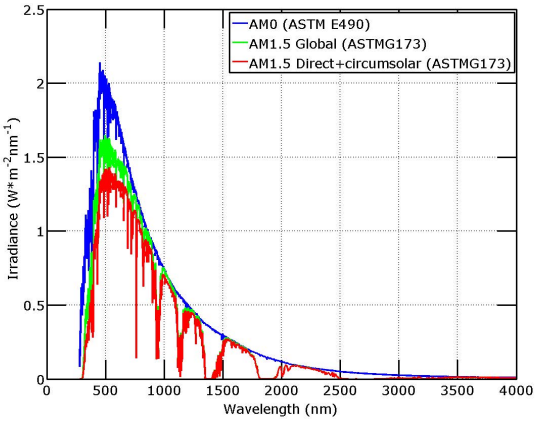

Figure 6: Solar spectrum, the green line is the AM1.5 Global.

of most of the solar spectrum. Geometrical optics is no longer applicable at these length scales and ray-tracing methods are thus, inaccurate. Instead, simulation methods which capture the wave-like nature of light must be utilized such that effects such as interference and diffraction are properly captured. The absorption, transmission, and reflection spectra of most nanomaterials can be predicted from a completely classical theory of electromagnetism. This involves solving Maxwell's equations:

$$\begin{aligned} \nabla \cdot \mathbf{E} &= \frac{\rho}{\epsilon_0} \\ \nabla \cdot \mathbf{B} &= 0 \\ \nabla \times \mathbf{E} &= -\frac{\partial \mathbf{B}}{\partial t} \\ \nabla \times \mathbf{B} &= \mu_0 \mathbf{J} + \mu_0 \epsilon_0 \frac{\partial \mathbf{E}}{\partial t} \end{aligned} \tag{2.3}$$

where $\mathbf{E}$ and $\mathbf{B}$ are the electric and magnetic fields, and ρ and $\mathbf{J}$ are the free charge and current densities. The materials may be parameterized through phenomenological material parameters such as the complex valued refractive index, $n(\omega) = n_r(\omega) + n_i(\omega)$ or the complex permittivity $\epsilon(\omega) = \epsilon_r(\omega) + \epsilon_i(\omega)$. Simulations agree well with experiments, and typically semiclassical treatments (where light is treated classically and the material is treated quantum mechanically) or full quantum treatments are unnecessary. For example, silicon has a

Bohr exciton radius of about 2 nm, such that silicon nanostructure dielectric constants are not modified by quantum mechanics.

A variety of electrodynamic simulation methods have been used in studying the interactions of electromagnetic radiation with nanostructures including the transfer matrix method (finite difference frequency domain),[22–24] finite element method,[25, 26] rigorous coupled mode analysis (fourier modal method),[27, 28] and finite difference time domain methods.[29, 30] Electrodynamic simulation methods can be generally classified into time-domain simulations or frequency-domain response methods, and frequency-domain eigensolvers. Common discretization schemes are finite differences, finite elements, and spectral methods.

Finite difference frequency domain methods such as the transfer matrix method comprise of solving for the electric field $\mathbf{E}(\mathbf{r})\exp^{-i\omega t}$ in terms of the current source $\mathbf{J}(\mathbf{r})\exp^{-i\omega t}$ in Maxwell equations:

$$\left[(\nabla\times\nabla-\frac{\omega^2}{c^2}\epsilon(\mathbf{r})\right]\mathbf{E}(\mathbf{r})=i\omega\mu_0\mathbf{J}(\mathbf{r}). \tag{2.4}$$

The finite difference or finite element method may be applied to this linear equation to discretize it. These equations must be solved for at every frequency, where a table of experimental dielectric constants may be used.

In time domain methods, the full time dependent Maxwell equations are solved for in both space and time. The most common implementation for time-domain simulations is the finite-difference time-domain method (FDTD technique) which divides space and time into a grid of discrete points and approximate the derivatives in Maxwell equations by finite differences.[31] A Yee grid is used in which the different field components are associated with different locations on the grid.[32] Many frequencies can be computed with a single computation, by taking the Fourier transform of the response to a short pulse. This is the method we use in our research, and a commercial-grade simulator based on the finite-difference time-domain method was used to perform the calculations, [33] capable of analyzing the interaction of UV, visible, and IR radiation with complicated structures employing wavelength scale features.

Appropriate boundary conditions can be used to reduce the simulation cell. For example, periodic boundary conditions are used to model semi-infinite arrays. Symmetric and anti-symmetric boundary conditions may also be used to reduce the simulation size. Perfectly

matched layers (PML) are typically used for certain boundaries of the computational region to ensure that fields radiate to infinity instead of reflecting when they interact with the edge of the simulation cell.[34] Simulations where the only absorbing material is the active region may use $A(E) = 1 - R(E) - T(E)$ to calculate the absorption spectra. In plasmonic solar cells or other architectures which involve other parasitically-absorbing materials other than the photoactive active region, the position-dependent absorption must be calculated. The position dependent absorption per unit volume may be calculated from the divergence of the Poynting vector $\vec{P}$ which will be discussed in details in next part.

2.3 SOLAR CELL PERFORMANCE CALCULATIONS

There are several important parameters to characterize the optical performance of a cell solar, such as absorption and absorption length and ultimate efficiency. Meanwhile, electrical properties such as short circuit current density, electrical field and generation rate are also used to evaluate and analyze the performance of a solar cell. Here gives out the formulas to calculate these parameters under the solar spectra AM1.5. The index of refraction is $n = n_r - jn_i$, where $n_i > 0$ corresponds to loss. For non-magnetic media, the absorption coefficient is defined as

$$\alpha \equiv \frac{1}{I}\frac{d}{dz}I. \tag{2.5}$$

$$\boxed{\alpha = \frac{2\omega|n_i|}{c} = \frac{4\pi}{\lambda}|n_i|}. \tag{2.6}$$

The time-averaged power flux varies from cross-section to cross-section as $\exp(-\alpha z)$.

$$I(z) = |\mathbf{E}|^2 = I(0)\exp(-\alpha z) \tag{2.7}$$

where $I(0)$ is the intensity of the electromagnetic radiation at $z = 0$.

The absorption length is

$$\boxed{L_\alpha \equiv \frac{1}{\alpha}}. \tag{2.8}$$

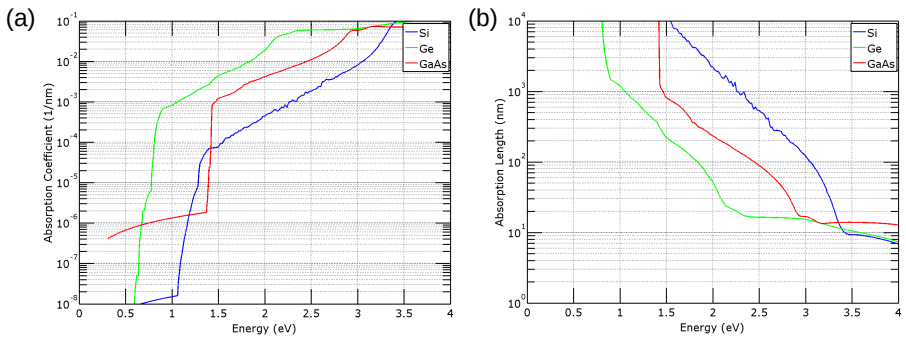

Figure 7: (a) Absorption coefficient and (b) absorption length versus energy of different semiconductor materials Si, Ge and $GaAs$.

Figure 7 plots the absorption coefficient and absorption length for three different semiconductor materials Si, Ge and $GaAs$.

With the experimental or computational absorption spectra of a solar cell, the integrated absorption may be calculated from

$$A_i = \frac{\int b_s(E)A(E)dE}{\int b_s(E)dE} \tag{2.9}$$

where A_i is the integrated absorption, and $A(E)$ is the absorption as a function of energy (E) or corresponding wavelength.

The ultimate efficiency is defined as

$$\boxed{\eta_{ue} = \frac{\int_0^{\lambda_g} I(\lambda)A(\lambda)\frac{\lambda}{\lambda_g}d\lambda}{\int_0^{\infty} I(\lambda)d\lambda} = \frac{\int_{E_g}^{\infty} I(E)A(E)\frac{E_g}{E}dE}{\int_0^{\infty} I(E)dE}} \tag{2.10}$$

where E_g is the band gap and λ_g is the wavelength corresponding to the band gap and $A(\lambda)$ or $A(E)$ is the absorption at a particular wavelength or energy. Ultimate efficiency assumes that the temperature of the cell $T_c = 0$ K such that there is no recombination. Under this

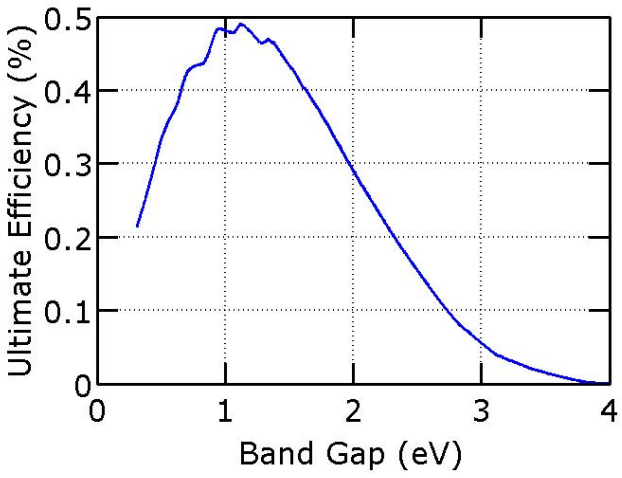

Figure 8: Ultimate efficiency versus band gap energy with perfect absorption and no recombination.

circumstance, if the solar cell is assumed to be perfectly absorbing, non-reflecting material such that the (external) quantum efficiency is

$$QE(E) = A(E) = \begin{cases} 1, E \geq E_g \\ 0, E < E_g \end{cases} . \tag{2.11}$$

Each photon with energy greater than the band gap produces one electron-hole pair, and these carriers are collected without recombination. The ultimate efficiency can be plotted depending on band gap of the material, as shwon in Figure 8.

For a solar cell, electric field intensity is

$$|\mathbf{E}(\mathbf{r}, \mathbf{E})|^2 = |\tilde{\mathbf{E}}(\mathbf{r}, E)|^2 \frac{I(E) Area}{P_{in}(E)}. \tag{2.12}$$

where $|\tilde{\mathbf{E}}(\mathbf{r}, E)|^2$ is the electric field intensity of the simulation, $Area$ is the area of the simulation, and P_{in} is the power of the simulation.

The weighted electric field intensity is

$$|\mathbf{E}(\mathbf{r})|^2 = \int_0^\infty |\mathbf{E}(\mathbf{r}, E)|^2 \frac{I(E) Area \; dE}{P_{in}(E)}. \tag{2.13}$$

The position dependent absorption per unit volume may be calculated from the divergence of the Poynting vector $\vec{P}$:

$$\tilde{A}(\mathbf{r}, E) = \frac{1}{2}\text{real}\{\vec{\nabla} \cdot \vec{P}\} = \frac{1}{2}\epsilon_i(E)\frac{E}{\hbar}\left|\tilde{\mathbf{E}}(\mathbf{r}, E)\right|^2 \tag{2.14}$$

Assuming the absorption of each photon results in one electron-hole pair, the generation rate is calculated from

$$\tilde{G}(\mathbf{r}, E) = \frac{1}{2E}\text{real}\{\vec{\nabla} \cdot \vec{P}\} = \frac{\epsilon_i(E)\left|\mathbf{E}(\mathbf{r}, E)\right|^2}{2\hbar}. \tag{2.15}$$

The position-dependent generation is

$$G(\mathbf{r}) = \int_0^\infty \frac{I(E)Area\ \tilde{G}(\mathbf{r}, E)}{P_{in}(E)}dE = \int_0^\infty \frac{b_s(E)Area\ \tilde{A}(\mathbf{r}, E)}{P_{in}(E)}dE \tag{2.16}$$

2.3.1 Efficiency limiting

Now we consider a solar cell under light,

$$0 = J_s + J_{th} - J_{rad} - J \tag{2.17}$$

where J_s is the current from solar generation, J_{th} is generation from ambient temperature, J_{rad} is from radiative recombination, and J is from the extraction of electrons and holes.

This equation may be reorganized as

$$J = J_s - [J_{rad} - J_{th}] \tag{2.18}$$

where the term in brackets is the current in the dark.

The total current is

$$\boxed{J(V) = J_{sc} - J_{dark}(V)} \tag{2.19}$$

where $J_{sc} = J_s$ and $J_{dark}(V) = J_{rad} - J_{th}$.

The short-circuit current density is

$$\boxed{J_{sc} = q\int_0^\infty b_s(E)A(E)dE.} \tag{2.20}$$

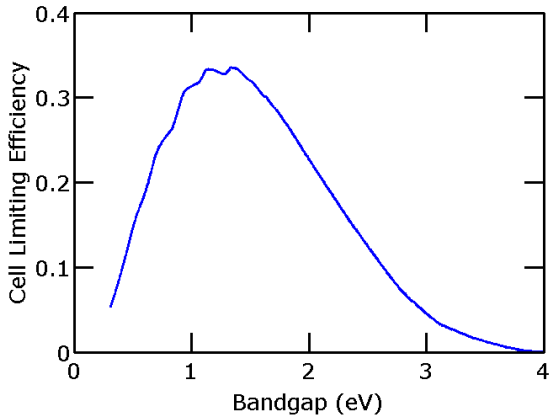

Figure 9: Limiting Efficiency versus Band gap energy.

The dark current may be determined from

$$J_{dark}(V) = q \int_0^\infty \left[b_e(E, \Delta\mu)\epsilon(E) - b_e(E, 0)A(E) \right] dE. \tag{2.21}$$

where $\epsilon(E)$ is the emission. The emission out of the solar cell is equal to the absorption in the dark, and can shown to be still equal under constant $\Delta\mu$. Thus,

$$\boxed{J_{dark}(V) = q \int_0^\infty \left[b_e(E, \Delta\mu) - b_e(E, 0) \right] A(E) dE.} \tag{2.22}$$

The quasi Fermi level is assumed to be constant throughout the cell. The difference in quasi Fermi level between the excited and ground states is $\Delta\mu = qV$.

The extracted power is calculated from

$$P = VJ(V) \tag{2.23}$$

and the limiting efficiency as plotted in Figure 9 is

$$\eta = \frac{\max(VJ(V))}{P_s} \tag{2.24}$$

where $P_s = \int_0^\infty I(E)dE$. This is refered as Shockley-Queisser limit [35] considering radiative recombination of electron-hole pairs through spontaneous emission.

3.0 LIGHT MANAGEMENT IN SILICON THIN FILM SOLAR CELLS

Due to the silicon properties discussed above, the main challenge with the use of silicon for photovoltaics is that silicon is not a strong absorber of sunlight in the near-infrared region. Conventional silicon photovoltaics are thus typically of thicknesses 200 to 300 µm to ensure the absorption of most sunlight. However, single crystalline silicon solar cells require expensive manufacturing methods, such as the Siemens method for solar grade purification, Czochralski method for crysallization, and wafer slicing. So current solar cell technology is not as competitive as that of traditional energy sources. To promote and increase the silicon solar cell capacity, costs need to drop below $1/W. Increasing absorption of light in the absorber layers is critical issue for achieving high efficiency silicon solar cells. Different light management strategies are thus important for increasing the photon optical length, the distance a photon travels in silicon before escaping, in order to increase absorption for a particular thickness of silicon.

In 1982 Yablonovitch and Cody [36] calculated the upper limit for light intensity in a dielectric slab with refractive index n and sandviched in vacuo. With the application of roughened surfaces which scatter or randomize the light upon reflection. Because Lambertian surfaces may be utilized to randomize light [37]. The mean path length of light inside the material may be increased from $2L$ to $4n^2L$ where n is the index of refraction. The absorption is

$$A(E) = \frac{\alpha(E)}{\alpha(E) + \frac{1}{4n^2L}} \tag{3.1}$$

3.1 LIGHT MANAGEMENT TECHNIQUES IN SILICON THIN FILM SOLAR CELLS

Various of light trapping methods have been developed recently both experimentally and computationally. Light trapping with sub-wavelength nanostructures involves coupling light into localized resonant modes and guided resonance modes in the active region to increase absorption. Nanophotonic light trapping strategies have used structuring of the silicon itself or patterning of dielectric materials on the front and back of the silicon. Plasmonic light trapping has involved using different metal nanostructures on the back and front of the active region to increase absorption.

Many innovative silicon structures have been experimentally demonstrated for the active region in solar cells, including ultrathin microcells[38], crystalline silicon nanowire arrays[39–47], horizontal silicon nanowire arrays,[48] crystalline silicon single nanowires[49–51], amorphous nanopillar and nanocone arrays [52, 53], crystalline silicon nanoholes[54] and silicon photonic crystals[55]. Photonic crystals have also been used next to the silicon active region to enhance absorption by coupling light into guided resonance modes. This has been demonstrated in crystalline silicon[56], nanocrystalline[57], and amorphous silicon[58].

Plasmonic nanostructures have also been experimentally demonstrated as an effective way to increase absorption in silicon. In thin-film silicon photovoltaic cells, metallic nanostructures may utilize plasmons for light trapping by sub wavelength scatterering, coupling to localized surface plasmons, or coupling into propagating surface plasmon polaritons[59].

Photonic crystals have been used to trap light through a variety of different strategies. Several simulation studies involving structuring the silicon active region into a photonic crystal [27, 28, 60–63]. Numerous simulation papers have studied photonic crystals as high-quality back reflectors for light trapping [64–67]. A number of studies have evaluated plasmonic solar cells. The shape, size, particle material, and dielectric environment of metal nanoparticles have been systematically evaluated in determining the effect of light scattering [68–70]. By modify the geometries of the nanoparticles, the surface plasmon resonances may be tuned to couple light into the silicon active region.

In summary, enhancing light absorption in the absorber layers of photovoltaic devices is mainly performed in two ways: coating anti-reflection (AR) layers on the surface or confining light inside the absorber layer.

4.0 ANTI-REFLECTION NANOSTRUCTURE COATINGS

4.1 ANTI-REFLECTION METHODS

The concept of AR coatings (ARCs) was conceived in the 19th century by Lord Raileigh. He found that glass with tarnished surfaces could increase the transmission of incident light [71]. After long time of research, the most commonly used ArCs in the industry are the quarter-wavelength-thick dielectric layer due to low cost and efficient fabrication. However, it is very obvious that single quarter-wavelength ARCs has best performance only for a single wavelength. Furthermore, if the incident light is oblique, the anti-reflection effect will also be compromised. Thus, lots of research about multiple layered ARCs have been done, but the anti-reflection effect is still not sufficient due to lack of materials with refractive index close to that of air [72–74]. So nanostructures have become hot topic for anti-reflection, such as nanowires have been studied thoroughly [75–77].

4.2 TIO_2 PHOTONIC CRYSTAL AS ANTI-REFLECTION

In my work, I study the anti-reflection effect of a woodpile structure made of TiO_2. The geometries of the woodpile structure is investigated.

4.2.1 TiO_2 optical properties

For the refractive index TiO_2 has high n values (2.5) and low k values (near 0), which makes it a good candidate for anti-reflection coatings without absorption of the light. The optical

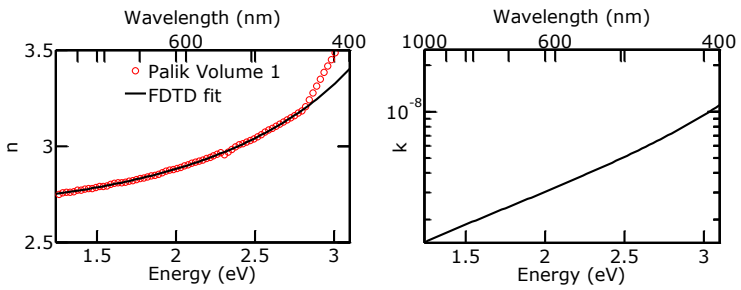

Figure 10: Plots of the (a) real n and (b) imaginary part k of the TiO_2 refractive index. Values from Palik Volume 1 [78] and FDTD fitted values are shown.

constants of TiO_2 from *Handbook of Optical Constants of Solids* [78] and fitting values in FDTD are both shown in Figure 10.

4.2.2 Calculated results

In my work we propose a TiO_2 woodpile structure 2D photonic crystal made of TiO_2 as shown in Figure 11 which can be fabricate by our collaborator Dr. Kevin P. Chen from Electrical Engineering department. The parameters of the structure are the thickness of the silicon layer t, the diameter d of the TiO_2 nanorod and the pitch a of lattice. The diameter is equal or smaller than the lattice pitch $d \leq a$. The pitch of the lattice varies from 100 to 1000 nm. The Ag layer serves as a back reflector and the thickness is 100 nm.

We evaluated the optical properties over the energy range of the solar spectrum from 1.24 eV to 3.1 eV (wavelengths from 1000 to 400 nm). A uniform mesh of 20 nm $\times$ 20 nm $\times$ 20 nm was utilized where the ultimate efficiency was found to have converged within 1%. Perfectly matched layer boundary conditions were used for the upper boundary of the simulation cell [34], and Metal boundary condition was used for the lower boundary os the simulation cell as a back reflector and appropriate boundary conditions were used for the side boundaries to model the periodic nature of the arrays. We systematically optimized the geometry for the greatest ultimate efficiency for 1000 nm and 2000 nm thick silicon thin film.

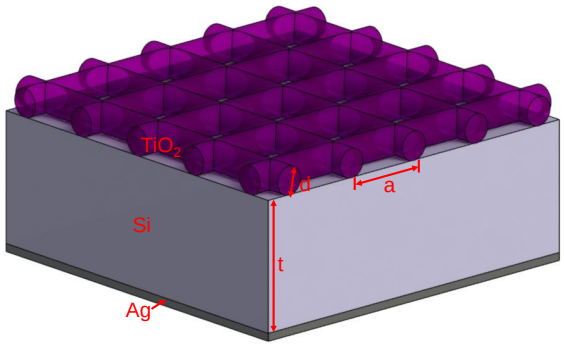

Figure 11: Schematic of the TiO_2 anti-reflection structure on silicon thin film.

Figure 12(a) and (b) utilize contour plots to illustrate the dependence of ultimate efficiency on the diameter and pitch of the TiO_2 nanorod and pitch of the lattice for 1000 nm and 2000 nm thick silicon, respectively. Silicon thin film with TiO_2 thin film anti-reflection layer structure is also simulated to optimize the thickness of TiO_2 layer for different thickness silicon films (a) 1000 nm and (b) 2000 nm as shown in Figure 13. The optimal TiO_2 thickness for both thickness silicon is 40 nm.

For 1000 nm thick silicon, the optimal efficiency is 30.33% with $d = 220nm$ and $a = 600nm$. For bare silicon thin film with same thickness the efficiency is only 14.44% and 18.09% with 40 nm thick TiO_2 thin film as anti-reflection layer. So with the woodpile structure anti-reflection layer, the efficiency is increased by 67.66% compare with the traditional thin film anti-reflection structure. Even compare with double pass of same thickness thin film which is 20.78%, the efficiency is still increased by 46%, so the improvement is quite significant.

For 2000 nm thick silicon, the optimal efficiency is 31.25% with $d = 260nm$ and $a = 600nm$. For bare silicon thin film with same thickness the efficiency is only 18.08% and 22.59% with 40 nm thick TiO_2 thin film as anti-reflection layer. So with the woodpile structure anti-reflection layer, the efficiency is increased by 38.33% compare with the traditional thin film anti-reflection structure. Even compare with double pass of same thickness thin film which is 26.46%, the efficiency is still increased by 16%, so the improvement is still

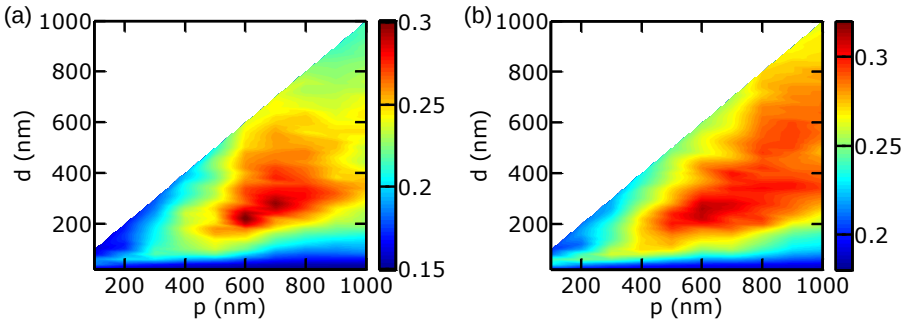

Figure 12: Contour plots of ultimate efficiency against nanorod diameter d and lattice constant a for (a) 1000 nm and (b) 2000 nm silicon thin film.

quite significant though the improvement is weakened by the increase of the thickness of the silicon.

In order to show the optical performance advantages of woodpile structure anti-reflection layers, the absorption and reflection spectra of three representative structures (thin film with woodpile anti-reflection, optimal with thin film anti-reflection layer and double pass) are plotted in 14 for 1000nm thick silicon film and 15 for 2000 nm thick silicon film. From the plots we can find that, the reflection of woodpile anti-reflection coating is much lower than that of thin film anti-reflection coating almost in the entire wavelength range for both thicknesses. And the absorption is higher than that of thin film ideal double pass when the energy is smaller than 2.36 eV for 1000 nm thickness and 2.22 eV for 2000 nm thickness.

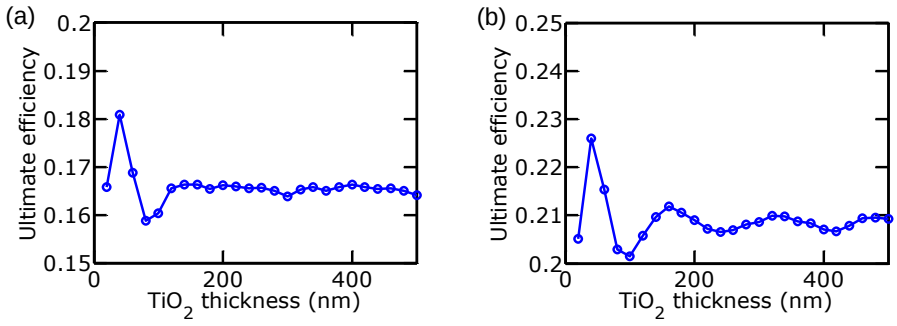

Figure 13: Plots of ultimate efficiency against TiO_2 thickness for (a) 1000 nm and (b) 2000 nm silicon thin film.

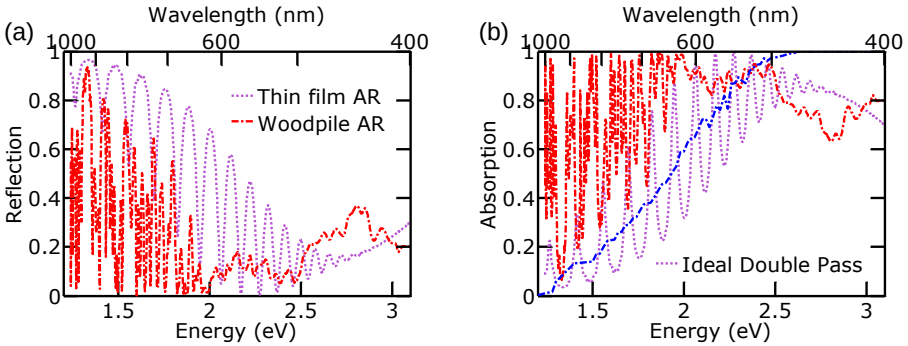

Figure 14: Plots of reflection and absorption for three representative structures for 1000 nm thickness.

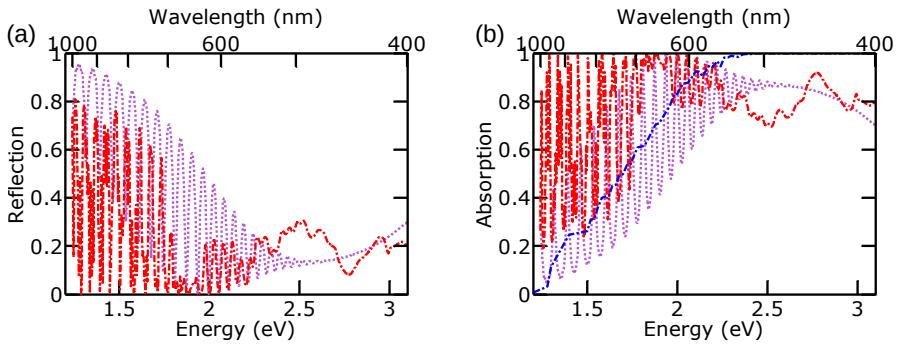

Figure 15: Plots of reflection and absorption for three representative structures for 2000 nm thickness.

5.0 LIGHT TRAPPING IN SILICON THIN FILM NANOSTRUCTURES

5.1 LIGHT TRAPPING METHODS

With the ARCs, we can induce more light into the solar cells, but the light need to be absorbed more efficiently by the active layer. Light trapping is an important way to confine light inside the active layer of the solar cells, as discussed above, lots of light trapping method have been developed, mainly including light scattering and resonance. Increasing the optical path length is pretty desirable for the solar cells, and light scattering can improve absorption for wide range of wavelengths by enhancing the light medium interaction. Silicon nanowires or similar nanostructures show significant light trapping effects due to collective resonances and optical density of states change [44, 46, 76, 79].

The resonance modes have been found in dielectric microspheres and nanospheres structures. The dielectric nanospheres like silica [80] can induce whispering gallery modes and thus the light absorption is significantly enhanced.

Photonic crystals can server as a absorber to confine light inside the structure, so it's a potential approach to control light propagation and localization in the solar cells. Photonic crystals can achieve almost perfect reflectivity and light confining for range of wavelengths within the photonic bandgap due to the spectral selectivity.

All of the three types of structures above are systematically studied in my research as presented below.

5.2 ENHANCED ABSORPTION IN SILICON TAPERED NANOCONES STRUCTURES

Recently, silicon nanocones or tapered nanowires have been experimentally fabricated by metal-assisted electroless etching [81] and a Langmuir-Blodgett assembly and etching technique [52, 53]. These structures have been suggested as candidates for solar cells due to reduced reflection over a broad range of wavelengths through a graded effective refractive index. In this work, we perform detailed numerical investigations of the optical properties and solar conversion efficiencies of nanocone solar cells for a variety of geometries and compare them to nanowire arrays. We found significant enhancements to absorption and conversion efficiencies in silicon nanocone arrays.

Figure 16 shows the schematic of the silicon nanocone arrays studied () [82]. The parameters of the structure are the length L, the period a of the square lattice, and the top diameter d_{top} and the bottom diameter d_{bot}. We evaluated the optical properties over the entire energy range of the solar spectrum from $E = 0.3$ to 4.4 eV (wavelengths from 4000 to 280 nm). The optical constants for silicon were taken from experimental measurement results in Palik's *Handbook of Optical Constants of Solids* [78]. We utilized a uniform mesh of 20 nm $\times$ 20 nm $\times$ 20 nm where the ultimate efficiency was found to have converged within 1%. Perfectly matched layer boundary conditions were used for the upper and lower boundary of the simulation cell [34], while appropriate boundary conditions were used for the side boundaries to model the periodic nature of the arrays.

5.2.1 Calculated results

In our studies, we focused on a variety of different geometries for silicon nanocones with fixed pitch $a = 600$ nm, since this pitch has been shown to be optimal for silicon nanowires [26, 76]. The efficiencies of nanocones and nanowires were compared at a variety of lengths, though we initially focused on nanocones and nanowires with length $L = 2.33$ µm. Figure 17 shows the results of these studies. Figure 17(a) shows the ultimate efficiency as a function

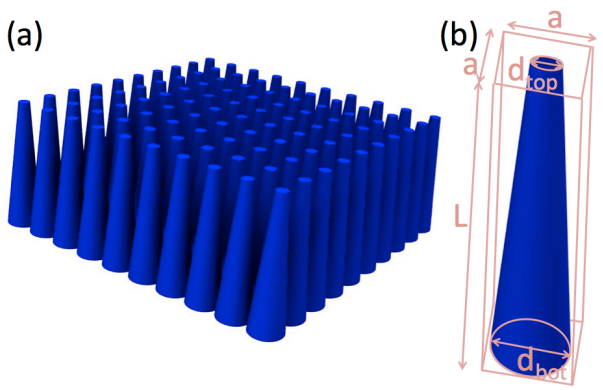

Figure 16: (a) Schematic of the silicon nanocone array structure. (b) The parameters for the array are the length L, the period a, the top diameter d_{top}, and the bottom diameter d_{bot}.

of diameter d for vertical nanowire arrays. The optimal ultimate efficiency was found to be 29.8% when $d = 560$ nm or the fill fraction $f = 0.68$. The ultimate efficiency is $> 27\%$ when $d > 400$ nm (or $f > 0.35$).

However, significant superior ultimate efficiencies may be achieved with silicon nanocones. Figure 17(b) utilizes a contour plot to illustrate the dependence of ultimate efficiency on the geometry of the silicon nanocone. The parameters d_{top} and d_{bot} were varied from 40 to 600 nm in 40 nm increments and values between data points were obtained by triangle-based linear interpolation. Nanowires are special instances of nanocones, where the diameter is constant across the entire length of the structure or $d = d_{top} = d_{bot}$, and a dotted line is plotted in the contour plot to indicate this geometry. In our studies, we found that nanocones with $d_{top} < d_{bot}$ may be utilized to achieve better ultimate efficiencies than nanowires. The optimal ultimate efficiency was 36.2% for $d_{top} = 200$ nm and $d_{bot} = 600$ nm, which is about 22% higher than that of the optimal single diameter nanowire array. One of the advantages of nanocones that may be observed from the contour plot is that the ultimate efficiency is not particularly sensitive to d_{top}. For example, ultimate efficiencies greater than 31% may be achieved for nanowires with $d_{bot} = 600$ nm and $d_{top} < 520$ nm. Optimal nanocone structures are robust in deviations from idealized geometries and not particularly sensitive to variation or imperfections in manufacturing techniques.

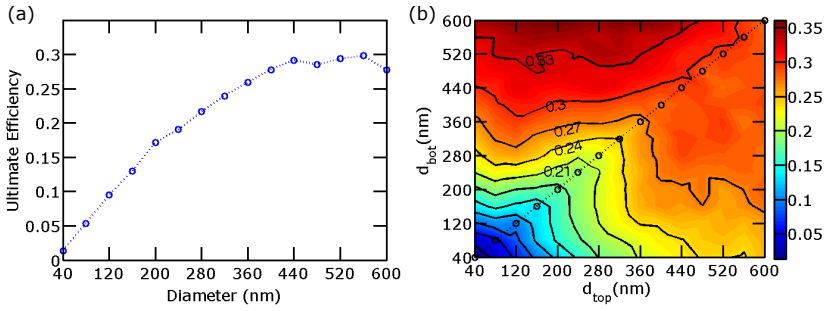

Figure 17: Ultimate efficiency of silicon nanowires and nanocones where the length $L = 2.33$ µm and pitch $a = 600$ nm. (a) Ultimate efficiency as a function of the diameter d for nanowire arrays. (b) Contour plot of ultimate efficiency for silicon nanocone arrays as a function of d_{top} and d_{bot}. The dotted line indicates $d_{top} = d_{bot}$, which is the geometry of nanowire arrays.

Based on the results of our investigations into different nanocone and nanowire geometries, we chose several representative nanowire and nanocone systems to compare their reflection, transmission, and absorption spectra. Figure 18 illustrates the (a) reflection, (b) transmission and (c) absorption as a function of energy for three representative systems. The optimum efficiency nanowire with $d = 560$ nm and optimum nanocone with $d_{top} = 200$ nm and $d_{bot} = 600$ nm are shown. Furthermore, we plot the spectra of the nanowire with $d = 200$ nm, since this is the top diameter of the optimal nanocone. In Figure 18(c), the absorption was calculated from $A(E) = 1 - R(E) - T(E)$, and the global 37° tilt Air Mass 1.5 spectrum is shown on the right y-axis. Single diameter nanowire systems exhibit a tradeoff between reflection and transmission. Smaller diameter nanowires such as the one illustrated with $d = 200$ nm have less reflection because there is less fill factor or area for light to reflect off the top of the nanowires. However, they also have higher transmission throughout the entire solar spectrum because there is less silicon to absorb the light. On the other hand, larger diameter nanowire arrays, such as the optimal single diameter system with $d = 560$ nm exhibit higher reflection due to higher fill factor and smaller transmission since there is more material to absorb the light. Larger diameter nanowire arrays have better absorption in the infrared range, but poorer absorption in the ultraviolet range.

Silicon nanocone arrays address the tradeoff between reflection and transmission with a smaller d_{top} and a larger d_{bot}. The optimal silicon nanocone array, with $d_{top} = 200$ nm and $d_{bot} = 600$ nm, especially in the visible and ultraviolet range, has reflection about the same of the small single diameter nanowire array with $d = 200$ nm. The larger base results in a transmission that is almost zero in the visible and ultraviolet regime. In the infrared range, the silicon nanocone array has absorption characteristics comparable to that of the best single diameter nanowire array. However, in the visible and ultraviolet range, the absorption is significantly improved with absorption from about 80% to 95% compared to 40% to 80% for the best single diameter structures. Table 1 lists the fraction of photons absorbed in different regions of the solar spectrum for these three representative nanowire and nanocone systems. The visible region is from 380 to 740 nm (1.7 to 3.3 eV), the ultraviolet region is from 280 to 400 nm (3.1 to 4.4 eV), and the infrared region (above the silicon band gap) is from 740 nm to 1100 nm (1.1 to 1.7 eV). The total solar region shown only includes the range above the silicon band gap energy from 280 to 1100 nm (1.1 to 4.4 eV). The silicon nanocone arrays have enhanced absorption compared to silicon nanowire arrays over the entire spectral range due to antireflection and low transmission in the visible and ultraviolet ranges.

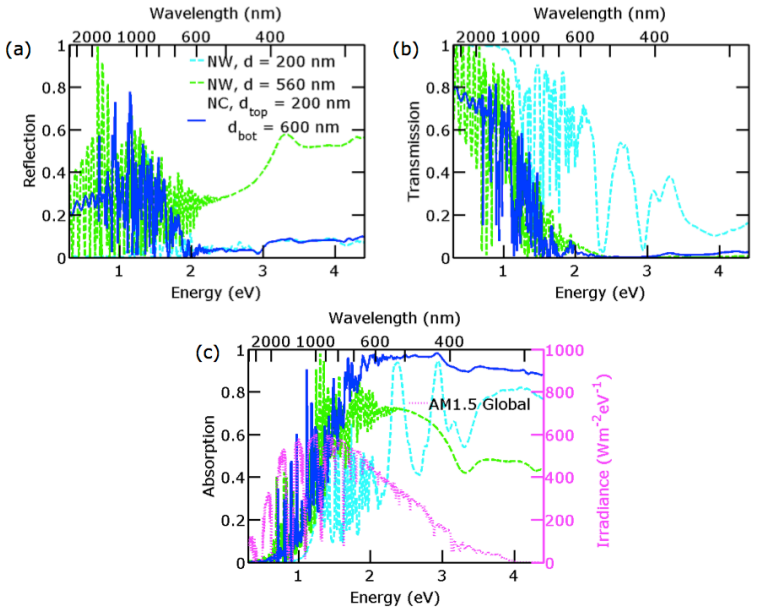

Figure 18: Optical properties of three different silicon nanostructures: single diameter nanowire (NW) arrays with $d = 200$ nm and $d = 560$ nm and nanocone (NC) arrays with $d_{top} = 200$ nm and $d_{bot} = 600$ nm. (a), (b), and (c) show the reflectance, transmittance, and absorption respectively. The irradiance of the Air Mass 1.5 solar spectrum is shown in the right y-axis of (c).

Table 1: Absorption in different wavelength regimes. The infrared and total solar regions are calculated for those portions of the regions that are above the silicon band gap ($E > 1.12$ eV).

Spectrum Region	**NW, d = 200 nm**	**NW, d = 560 nm**	**NC, $\mathbf{d_{top}}$ = 200 nm $\mathbf{d_{bot}}$ = 600 nm**
Infrared	21%	52%	54%
Ultraviolet	67%	46%	91%
Visible	45%	69%	93%
Total Solar	35%	61%	74%

In order to understand the propagation of light in the nanowire and nanocone arrays, we simulated the electrical field intensity $|\mathbf{E}(\mathbf{r}, E)|^2$ and calculated the generation rate within the arrays from

$$G(\mathbf{r}, E) = \frac{\epsilon_i(E)\,|\mathbf{E}(\mathbf{r}, E)|^2}{2\hbar} \tag{5.1}$$

where $\epsilon_i(E)$ is the imaginary part of the dielectric constant, $\hbar$ is the reduced Planck constant, and $\mathbf{E}(\mathbf{r}, E)$ is the energy and position-dependent electric field. By normalizing this quantity over the simulation power, and integrating over the the solar spectrum energies as weighted by the solar irradiance $I(E)$, we obtained the solar-spectrum-weighted generation rate. Figure 19 shows the cross-sectional (a) solar-spectrum-weighted electrical field intensity $|\mathbf{E}(\mathbf{r})|^2$ and (b) solar-spectrum-weighted generation rate $G(\mathbf{r})$ of the three representative nanowire and nanocone arrays for normal incident light integrated over photon energies $E = 0.83$ to 2.75 eV (or wavelengths $\lambda = 1500$ to 450 nm). This energy range encompasses about 86% of the power density available for absorption by silicon. The electric field of the incoming electromagnetic wave was out of the plane of the paper in these simulations. The left column illustrates single diameter nanowire arrays with $d = 200$ nm, the middle column shows the optimal single diameter nanowire arrays with $d = 560$ nm, and the right column illustrates the optimal nanocone arrays with $d_{top} = 200$ nm and $d_{bot} = 600$ nm. Dotted white lines indicate the edges of these silicon nanostructures.

In the 200 nm diameter nanowire arrays, a large portion of the electromagnetic (EM) waves propagates outside the Si nanowire. The EM waves decay in the radial direction, such that a significant portion of the carrier generation is near the surface. While the reflection is low in these nanowire arrays due to their small diameter, the transmission is also higher since there is less silicon to absorb the light, and the intensity of the electric field can be seen to be still significant near the bottom of the nanowire.

In the 560 nm diameter nanowire arrays, most of the carrier generation occurs in the center of the nanowire away from the nanowire surface. There is more silicon in the larger diameter nanowire arrays to absorb the EM waves, such that the electric field intensity is close to 0 at the bottom of the nanowire. However, because of the large fill factor or the large top of the nanowire, the reflection is substantial.

In the nanocone array, the EM field is seen to propagate further into structure. The small diameter d_{top} results in smaller reflection, while the larger base contains more silicon to absorb the light. The electric field intensity is seen to decay to very small values near the bottom of the nanocone array, indicative of small transmission. The nanocone arrays have the advantage that the carrier generation, similar to the larger diameter nanowires, occurs near the center of the nanocones, such that carriers are less likely to be affected by surface recombination. Furthermore, the carrier generation is more uniform along the length of the nanowire, such that photoexcited carriers are less likely to recombine, since the recombination rate is directly proportional to the local excess concentration of electrons and holes. Guided resonance modes (also called leaky-mode resonances) have been shown to play

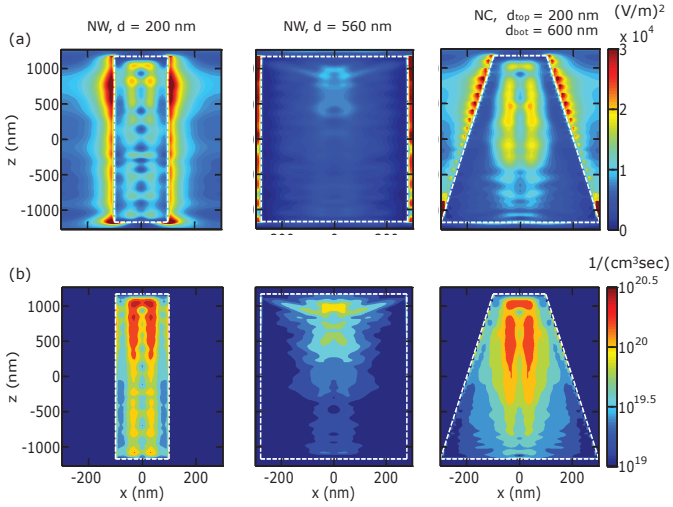

Figure 19: The (a) solar-spectrum-weighted electrical field intensity $|\mathbf{E}(\mathbf{r})|^2$ and (b) solar-spectrum-weighted generation rate $G(\mathbf{r})$ for three representative silicon nanowires and nanocones. From left to right, the systems shown are nanowire arrays with $d = 200$ nm, nanowire arrays with $d = 560$ nm, and nanocone arrays with $d_{top} = 200$ nm and $d_{bot} = 600$ nm.

a significant role in light absorption by nanowires [76, 83]. Nanowire arrays exhibit a mirror-symmetry plane at $z = 0$, such that modes must be either symmetric or antisymmetric

about the plane. TE-like modes are odd with respect to z and TM-like modes are even with respect to z. Distinct peaks may be seen in the absorption spectrum of nanowire arrays corresponding to the coupling of incident light with these guided resonance modes. These guided resonance modes may be tuned for the detection of particular energies or frequencies in photodetectors for example [83]. In photovoltaics however, it is generally desirable for absorption to occur over a broad range of energies. By tapering the nanowires or forming nanocones, the mirror symmetry is removed and the absorption spectrum is broadened such that the overall absorption may be enhanced over that of nanowire arrays.

In order to evaluate the performance of non-tracking photovoltaics, we simulated the angle-dependent optical properties of the optimal silicon nanocone array as compared to the optimal nanowire array. The integrated absorption averaged of TE and TM modes is plotted as a function of the zenith angle θ from 0 to 60 degrees in Figure 20. We found little variation in absorption with the azimuthal angle below 35 degrees for nanocone arrays. And the performance of nanocone array was always better than that of nanowire array.

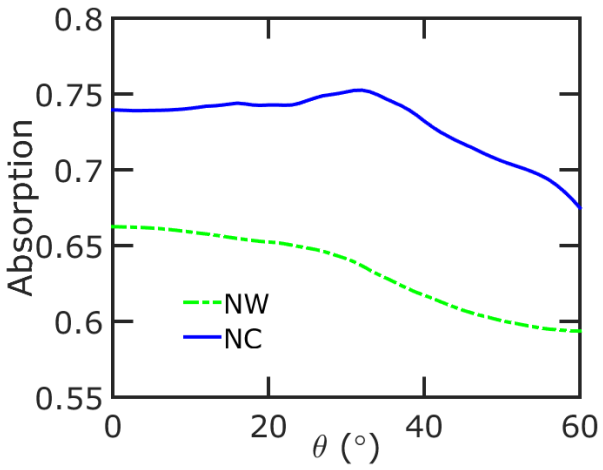

Figure 20: Relationship between integrated absorption and zenith angle θ of optimal nanowire and nancone arrays for average of TE and TM modes.

Finally, we considered different geometries of nanocone and nanowire arrays for a wide range of lengths. In addition to the length $L = 2330$ nm, we further compared nanocones

and nanowires for L from 50 to 10000 nm for fixed pitch $a = 600$ nm. The optimal ultimate efficiency and short circuit current for nanocone and nanowire arrays were obtained from these simulations and plot in Figure 21. We found that nanocone arrays have better efficiencies and short circuit currents than nanowires across a wide range of lengths. The efficiency enhancement (which is the same as the short circuit current enhancement for perfect carrier extraiont) of the optimal nanocone array over the nanowire array is plot on the right y-axis in Figure 21. The ultimate efficiency enhancement is greater than 20% for $L > 500$ nm. For the smallest length $L = 50$ nm, the amount of silicon is little such that the best structure is a nanowire with $d = a = 600$ nm. Most of the loss is through transmission, such that nanocones do not have an advantage over nanowires. However, for longer lengths, nanocones have significant advantages over nanowires when d_{top} is less than d_{bot}.

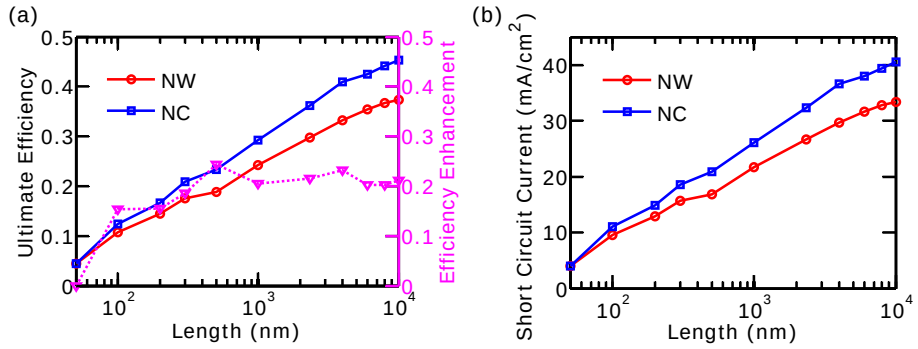

Figure 21: Optimal ultimate efficiency of silicon nanowires and nanocones with different length L.

This novel tapered nanocones structure can obtain enhanced absorption due to anti-reflection from the small tip and lower transmission due to the larger base. Nanocones may be fabricated by well-developed techniques, and are not particularly sensitive to specific geometry, which should facilitate their fabrication.

5.2.2 Experimental fabrication of silicon tapered nanocones

To fabricate the tapered nanocone structure, we use PS nanospheres monolayer as the mask, Bosch process (STS Multiplex ICP RIE in CMU) is employed to etch the silicon without nanospheres mask cover. we can modify the diameter of the nanospheres with oxygen RIE to control the final diameter of nanowires we get and the pitch of the nanocones or nanowires array is decided by the original diameter of PS nanosphere. The bosch process cycle works in two segments, at first SF_6 is flowing in and etch the exposed silicon, and secondly C_4F_8 is flowing in as the passivation gas to smoothy the surface of the etched silicon. Through controlling the number of cycles, we can control the length of nanowire or nanocones we get. Samples with SF_6 130 sccm for 6s and C_4F_8 85 sccm for 4s and 30 cycles are shown in Figure 22. The surface of the nanowire is with spiral structure, it is because the separation of the etching and passivation process. Thus we perform the two separated segments at the same cycle which is called pseudo bosch process and get vertical nanowire or nanocones without spiral structures as shown in Figure 23. Nanowires (Nanocones and tapered nanocones) with different aspect ratio are shown in 24 which are fabricated according the etch rate table.

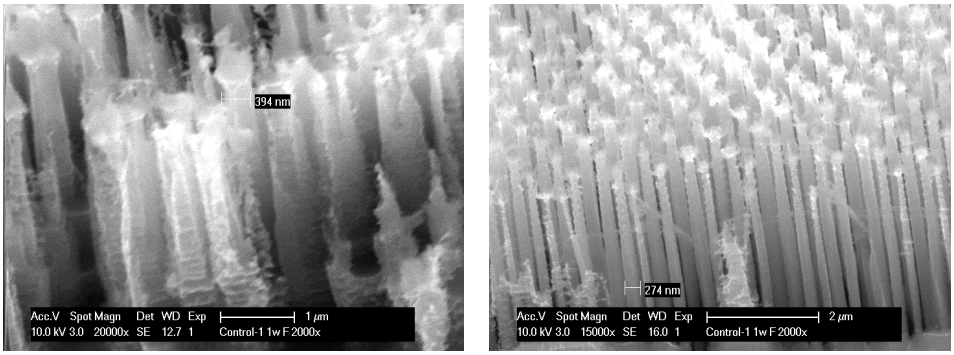

Figure 22: Side view of the silicon nanowires after 30 cycles etching.

In order to get tapered nanocones with different d_{top} and d_{bot}, we investigate the effect of gas ration between SF_6 130 and C_4F_8 on the final shape of nanocones. We compare the final d_{top} and d_{bot} of nanocones with the diameter of nanospheres and get the undercutting

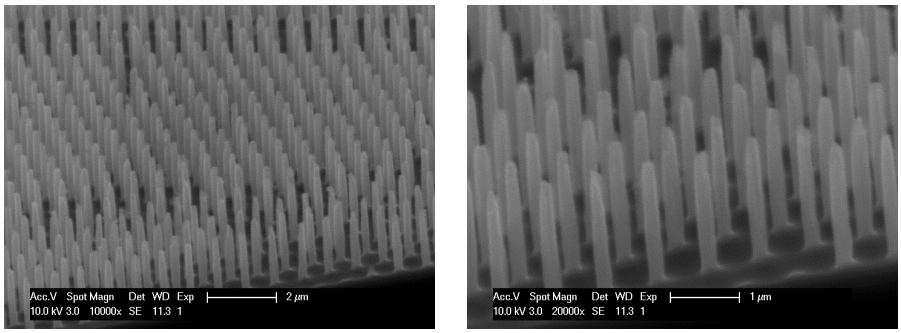

Figure 23: Side view of the silicon nanocones fabricated with pseudo bosch process.

for both top and bottom of the nanocones. The vertical height is also calcuated in order to get the etching ratio between etching ratio between horizontal and vertical orientations. The calcuations of different gas ratios are listed in Table 2. With the increase of concentration of passivation gas C_4F_8, the etch rate become smaller for both horizontal and vertical directions due to smaller concentration of etching gas. And the etching rate ratio between horizontal direciton and vertical direction (H/V) also becomes smaller which means the undercutting becomes smaller. When the ratio is 33:110, the undercutting is nearly 0 for both top and bottom, so the final shape will be vertical nanowires.

Table 2: Etch rate comparison of different gas ratio.

Orientation SF_6**:**C_4F_8	**Horizontal top**	**Horizontal bottom**	**Vertical**	**H/V ratio**
33:57	0.8	0.4	2.56	0.3
33:66	0.48	0.2	2.22	0.2
33:82.5	0.19	0.06	1.81	0.1
33:110	0.06	0	1.43	0.04

More importantly, we also employed a self mask method to fabricate black silicon on both bulk wafer and ultrathin substrate via the Bosch process as shown in Figure 25. Figure 25(a)

is the comparison between the silicon wafer and the black silicon. Figure 25 (b) is the reflection measurement of the bulk black silicon and ultrathin black silicon, and we can see that both have reflection lower than 4% over from 400 nm to 100 nm, and the reflection of the bulk black silicon is even lower than 2%. The morphology of the black silicon is shown in Figure 25.

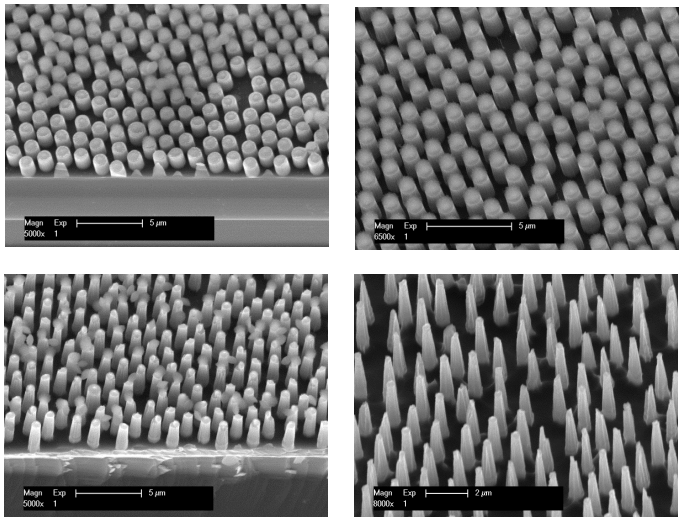

Figure 24: Nanowires with different aspect ration.

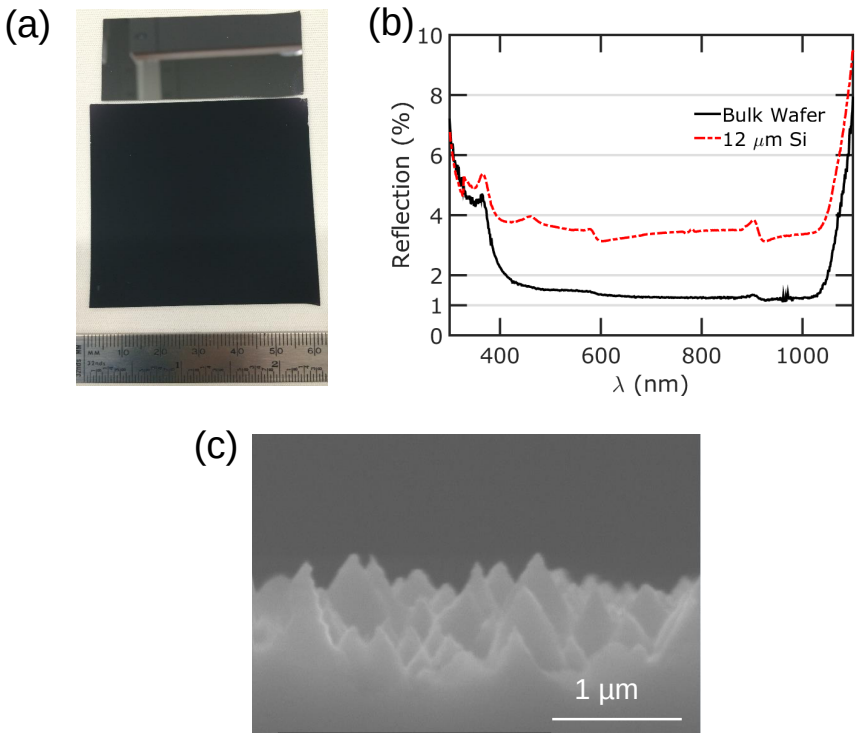

Figure 25: (a) Optical pictures of bare silicon wafer and bulk black silicon. (b) Measured reflection of bulk and ultrathin black silicon. (c) Side view SEM pictures of the black silicon.

5.3 APPLICATION OF TAPERED NANOCONE TECHNIQUE

5.3.1 GaAs tapered nanocones structures

Based on the advantage of tapered nanocone we find in silicon, we also apply this superior structure on GaAs [84]. Gallium is a rare and expensive material and the processing costs associated with GaAs are high, so light trapping is particularly important for GaAs solar cells. In this work, the schematics of the structures are the same with those of silicon, however, instead of fixing the pitch a, this time we also optimized the pitch. We studied GaAs nanocones and nanowires for a wide variety of lengths from $L = 100$ to 1000 nm. GaAs is a direct band gap material with absorption lengths > 1 µm for photons with wavelength

$\gtrsim 840$ nm ($E \lesssim 1.47$ eV). Thus, the lengths studied were smaller than 1000 nm, where light trapping may have significant benefit.

5.3.2 Enhanced absorption in GaAs tapered nanocones structures

Figure 26(a) plots the optimal ultimate efficiency for GaAs nanocone, nanowire, and thin films as a function of active region length L. The GaAs thin films consist of a GaAs layer without any antireflection coatings. For reference, we also plot the ultimate efficiency of single pass thin films. The absorption for single pass thin films under normal incidence light is

$$A(E) = 1 - \exp[-\alpha(E)L] \tag{5.2}$$

where $\alpha(E)$ is the energy dependent absorption coefficient of GaAs. The single pass thin film assumes perfect antireflection where the light passes through the material only once with no light trapping. The short circuit current is shown on the right y-axis of Figure 26(a). The short circuit current is linearly proportion to the ultimate efficiency under the assumption of perfect collection. Figure 26(b) plots the efficiency and short circuit current density enhancement of the nanowires and nanocones for each length compared to the single pass thin film. We found that while GaAs nanocones exhibit enhanced efficiencies and short circuit current densities over single pass thin films over all the lengths studied, GaAs nanowire arrays only have enhancements for lengths $L \leq 400$.

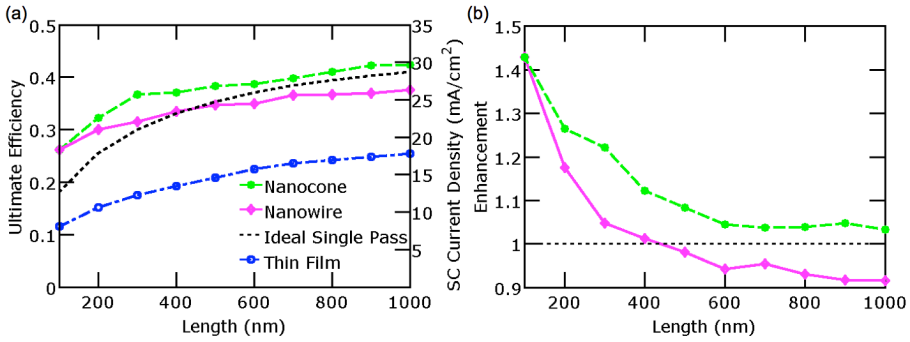

Figure 26: (a) Optimal ultimate efficiency of GaAs nanowires and nanocones as compared with thin film and ideal single pass thin film. The short-circuit (SC) current density is shown on the right y-axis. (b) The ultimate efficiency enhancement from GaAs nanowires and nanocones compared to ideal single pass thin film.

Figures 27(a) and 27(b) plot the parameters for optimal nanowire and nanocone arrays at different lengths L respectively. For nanowire arrays, the optimal pitch varied between 500 nm and 700 nm, and the optimal diameter was between 400 and 600. These optimal parameters for vertical GaAs nanowire arrays are similar to those determined in Huang *et. al* for $L \leq 1000$ nm [85]. The volume filling factor (FF) of the nanowire arrays is $\frac{\pi d^2}{4a^2}$, and for the nanocone arrays $FF = \frac{\pi(d_{top}^2 + d_{top} * d_{bot} + d_{top}^2)}{4a^2}$.

For nanocone structures, the optimal pitch was $a = 600$ nm for all lengths except when $L = 100$ nm. For $L = 100$ nm, the optimal nanocone array was the same as the nanowire array with $d_{top} = d_{bot} = d = 520$ nm. However, for lengths $L > 100$ nm, the optimal d_{top} was a small value between 200 nm and 400 nm and $d_{bot} = a$.

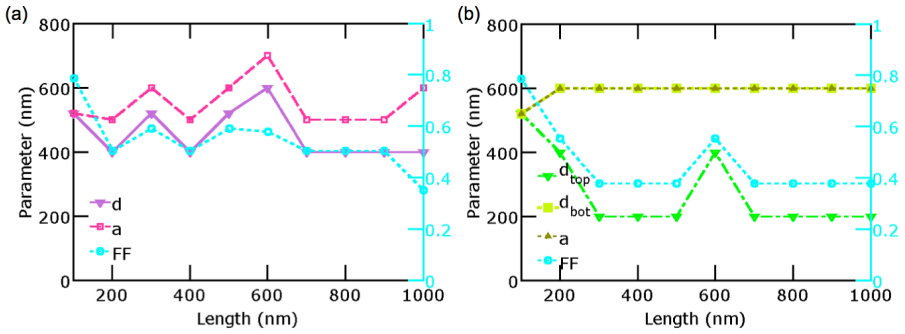

Figure 27: Optimal parameters for GaAs (a) nanowire and (b) nanocone for each length L, respectively. The volume filling factor of the optimal structure is shown on the right y-axis of both plots.

We chose several representative nanowire and nanocone systems with $L = 300$ nm to compare their reflection, transmission, and absorption spectra. Figure 28 plots the (a) reflection $R(E)$, (b) transmission $T(E)$, and (c) absorption $A(E)$ spectra as a function of energy E for a small diameter nanowire array ($d = 200$ nm and $a = 600$ nm), the optimal nanowire array ($d = 520$ nm and $a = 600$ nm) , and the optimal nanocone array ($d_{top} = 200$ nm, $d_{bot} = 600$ nm, and $a = 600$ nm). The absorption was calculated by $A(E) = 1 - R(E) - T(E)$. The absorption of an ideal single pass thin film with $L = 300$ nm is also plot in Figure 28(c) as calculated from Eq. (5.2). The reflection and transmission data shown for $E < E_g = 1.43$ eV were obtained through an additional FDTD simulation, where the imaginary part of the GaAs refractive index was set to 0 to account for the numerical error in the FDTD fit.

The ultimate efficiency for the single pass thin film is 30.0%. The optimal nanowire and nanocone arrays exhibit ultimate efficiencies of 31.4% and 36.6% respectively or enhancements of 4.7% and 22.0% respectively compared to that of the single pass thin film. The ultimate efficiency of the nanocone array is 16.5% higher than that of the nanowire array. The reflection, transmission, and absorption spectra of the nanowire system with $d = 200$ nm and $a = 600$ nm is also plotted, since this is the d_{top} of the optimal nanocone system.

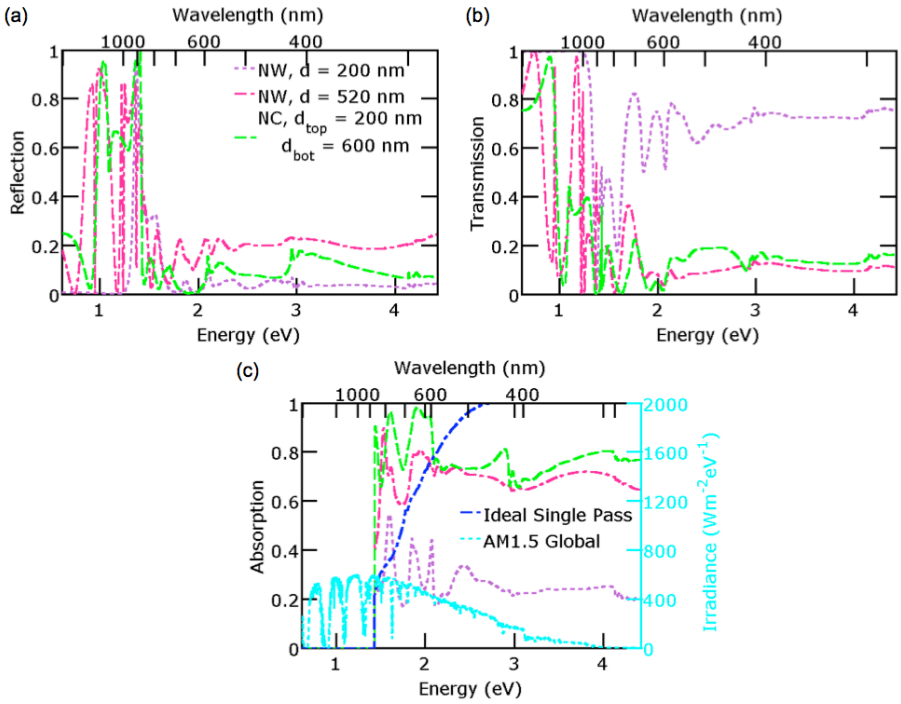

Figure 28: Optical properties of three different GaAs nanostructures: nanowire (NW) arrays with $d = 200$ nm and $d = 520$ nm and nanocone (NC) arrays with $d_{top} = 200$ nm and $d_{bot} = 600$ nm. $a = 600nm$ in all three systems. (a), (b), and (c) show the reflectance, transmittance, and absorption spectra respectively. The absorption spectrum of the ideal single pass thin film is also plot in (c). The irradiance of the Air Mass 1.5 global solar spectrum is shown in right y-axis of (c).

Nanowire systems exhibit a tradeoff between reflection and transmission. Smaller diameter nanowire arrays such as the one illustrated with $d = 200$ nm have less reflection because there is less filling factor for light to reflect off the top of the nanowires. $FF = 0.09$ in these nanowire arrays. However, they also have higher transmission throughout the entire solar spectrum because there is less GaAs to absorb the light. Smaller diameter nanowires have better absorption in the infrared regime (< 1.67 eV), but poorer absorption in the ultraviolet regime (> 3.1 eV). On the other hand, larger diameter nanowire arrays, such as the optimal single diameter system with $d = 520$ nm exhibit higher reflection due to higher filling factor ($FF = 0.59$) and smaller transmission since there is more material to absorb

the light. Larger diameter nanowire arrays have better absorption in the ultraviolet range, but slightly poorer absorption in the infrared range.

GaAs nanocone arrays address the tradeoff between reflection and transmission with a smaller d_{top} and a larger d_{bot}. The optimal GaAs nanocone array, with $d_{top} = 200$ nm and $d_{bot} = 600$ nm has reflection about the same of the small single diameter nanowire array with $d = 200$ nm, particularly in the visible and ultraviolet range. The larger base results in a transmission that is also low in the visible and ultraviolet regime. The GaAs nanocone array has absorption characteristics comparable to that of the best single diameter nanowire array in the ultraviolet range. However, in the visible and infrared range, the absorption is significantly improved. Table 3 lists the fraction of photons absorbed in different regions of the solar spectrum for these three representative nanowire and nanocone systems as well as the ideal single pass thin film. The ultraviolet region is from 3.1 to 4.4 eV (280 to 400 nm), the visible region is from 1.67 to 3.1 eV (400 to 740 nm), and the infrared region (above the GaAs band gap) is from 1.43 to 1.67 eV (740 to 867 nm). The total solar region shown only includes the range above the GaAs band gap energy from 1.43 to 4.4 eV (280 to 867 nm). The GaAs nanocone arrays have enhanced absorption compared to GaAs nanowire arrays over the entire spectral range due to anti-reflection and low transmission in the visible and ultraviolet ranges. Compared to the single pass thin film, the GaAs nanocones arrays have higher absorption except in the ultraviolet range.

In order to understand the propagation of light in the nanowire and nanocone arrays, we simulated the electric field intensity $|\mathbf{E}(\mathbf{r}, E)|^2$ and calculated the generation rate within the arrays. Figure 29 shows the (a) solar-spectrum-weighted electric field intensity $|\mathbf{E}(\mathbf{r})|^2$ and (b) solar-spectrum-weighted generation rate $G(\mathbf{r})$ of the three representative nanowire and nanocone arrays for normal incident light integrated over photon energies $E = 1.43$ to 2.75 eV (or wavelengths $\lambda = 867$ to 450 nm). This energy range encompasses about 83% of the power density available for absorption by GaAs. The contour plots show a cross-section through the center of the nanowire or nanocone. The electric field of the incoming electromagnetic wave was out of the plane of the paper in these simulations. The left column illustrates the optimal nanowire arrays with $d = 520$ nm, the middle column shows nanowire arrays with $d = 200$ nm, and the right column illustrates the optimal nanocone arrays with

d_{top} = 200 nm and d_{bot} = 600 nm. a = 600 nm in all three systems. Dotted white lines indicate the edges of these GaAs nanostructures.

Table 3: Absorption in different wavelength regimes. a = 600 nm in all three systems. The infrared and total solar regions are calculated for those portions that are above the GaAs band gap ($E > 1.43$ eV).

Spectrum Region	**NW d = 200 nm**	**NW d = 520 nm**	**NC, $\mathbf{d_{top}}$ = 200 nm $\mathbf{d_{bot}}$ = 600 nm**	**Single Pass**
Ultraviolet (%)	23	68	73	100
Visible (%)	27	71	81	77
Infrared (%)	35	67	83	32
Total Solar (%)	29	70	81	66

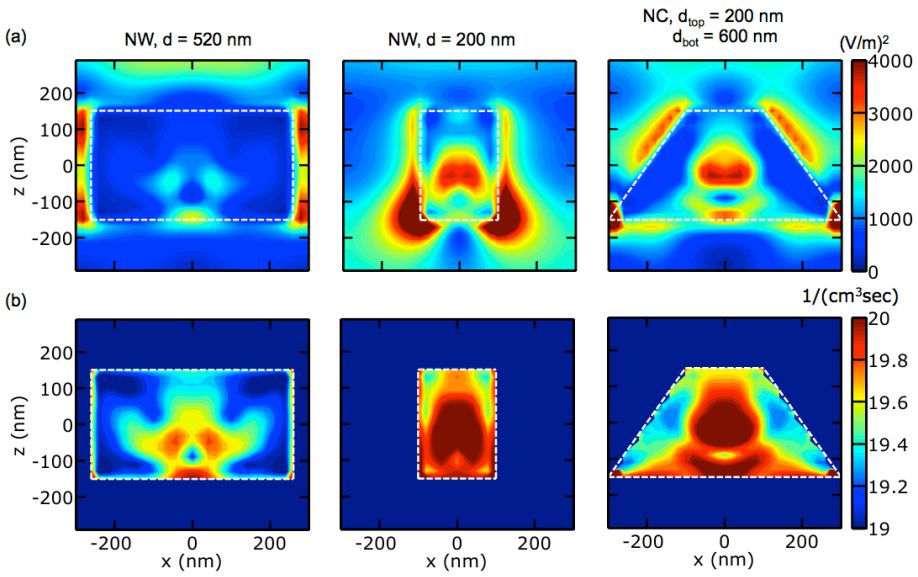

Figure 29: The (a) electric field intensity $|\mathbf{E}(\mathbf{r})|^2$ and (b) solar-spectrum-weighted generation rate $G(\mathbf{r})$ for three representative GaAs nanowires and nanocones. From left to right, they are nanowire arrays with $d = 520$ nm, nanowire arrays with $d = 200$ nm, and nanocone arrays with $d_{top} = 200$ nm and $d_{bot} = 600$ nm. $a = 600$ nm in all three systems.

In the 200 nm diameter nanowire arrays, a large portion of the electromagnetic (EM) waves propagates outside the GaAs nanowire. The EM waves decay in the radial direction, such that a significant portion of the carrier generation is near the surface. While the reflection is low in these nanowire arrays due to their small diameter, the transmission is also higher since there is less GaAs to absorb the light, and the intensity of the electric field can be seen to be still significant near the bottom of the nanowire. In the 520 nm diameter nanowire arrays, most of the carrier generation occurs in the center of the nanowire away from the nanowire surface. There is more GaAs in the larger diameter nanowire arrays to absorb the EM waves, such that the electric field intensity is close to 0 at the bottom of the nanowire. However, because of the large filling factor or the large top of the nanowire, the reflection is substantial. In the nanocone array, the EM field is seen to propagate further into structure. The small diameter d_{top} results in smaller reflection, while the larger base contains more GaAs to absorb the light. The electric field intensity is seen to decay to very

small values near the bottom of the nanocone array, indicative of small transmission. The nanocone arrays have the advantage that the carrier generation occurs near the center of the nanocones, such that carriers are less likely to be affected by surface recombination. The carrier generation is still significant at the bottom of the nanocone. Furthermore, the carrier generation is more uniform along the length of the nanocone, such that photo-excited carriers are less likely to recombine, since the recombination rate is directly proportional to the local excess concentration of electrons and holes.

By tapering the nanowires or forming nanocones, the mirror symmetry is removed and the photonics crystal properties are lost. The absorption spectrum is broadened such that the overall absorption may be enhanced over that of nanowire arrays. This mechanism works the same in the silicon structures.

Finally, we simulated the angular dependence of the absorption spectrum of the optimal GaAs nanocone array as compared to the optimal nanowire array. Figure 30 plots the integrated absorption as a function of the zenith angle θ from 0 to 35 degrees for both TE and TM illumination. We found little variation in absorption with the azimuthal angle. The results show that for both transverse-electric (TE) polarization and transverse-magnetic (TM) polarization, the absorption of GaAs nanocone arrays and nanowire arrays increase a little bit and then decrease slightly, but that generally the absorption variation is small. The variation is about 5% for the nanocone array and about 8% for the nanowire array. In the low angle range (0 to 35 degrees), the absorption of both nanowire and nanocone arrays are not affected much by the angle of the incident light. With higher incidence angles, the difference in absorption between nanowires and nanocones become smaller as the vertical symmetry of nanowires is also broken at nonnormal incidence angles. Nanocone arrays are slightly less sensitive than nanowire arrays to variation of incident light angle.

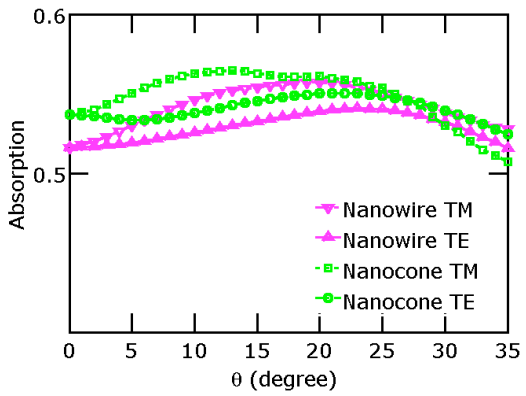

Figure 30: Relationship between absorption and zenith angle θ of optimal nanowire and nancone arrays for TM and TE illumination.

5.3.3 Conclusions

In summary, we have studied the optical performances of silicon and $GaAs$ nanocone arrays for photovoltaic application, and compared them with nanowire arrays across different diameters and lengths. This novel structure can obtain enhanced absorption due to anti-reflection from the small tip and lower transmission due to the larger base. Nanocones may be fabricated by well-developed techniques, and are not particularly sensitive to specific geometry, which should facilitate their fabrication. We have also evaluated the solar-spectrum-weighted electric field intensity and generation rate in nanocone arrays and determined advantages of nanocone arrays over nanowire arrays in where carriers are photoexcited. Breaking the vertical mirror symmetry of nanowires results in broader absorption spectrum such that overall efficiencies may be enhanced. These efficiencies are also superior over a broad range of incident angles. We proved that tapered nanocone structures worked for different materials solar cells, so we can promote this structures to other similar semiconductor materials for solar cells. Compared to the anti-reflection coatings like sol-gel method, the nanostructures have several advantages. First of all, we do not need to synthesis new solutions to fabricate the coatings. Secondly, the fabrication process is faster. Last but not least, the nanostructures are cheaper to fabricate than other anti-reflection coatings.

5.4 TUNABLE ABSORPTION IN SILICON NANOWIRES STRUCTURE

In our previous work, we demonstrate that leaky modes resonances in horizontal silicon nanowires may be used to manage spectral absorption. The nanowire acts as an optical antenna such that when incident light couples to a leaky mode resonance, there is an enhanced electromagnetic field in the nanowire and thus, increased absorption. In this work, we demonstrate that vertical nanowires exhibit tunable resonant absorption features that may be useful for photodetectors or sensors where high absorption and high spectral selectivity are desired. While single horizontal nanowire photodetectors have been demonstrated to absorb light at several resonant wavelengths, the horizontal device geometry suffers from poor quantum efficiency and responsivity due to weak absorption. Vertical nanowires may overcome the poor absorption in horizontal nanowires because the direction of incident light wave propagation is along the axis of the nanowire as opposed to in the radial direction.

5.4.1 Calculated results

The square vertical nanowire arrays are illustrated in Figure 31(a) and defined by pitch a, diameter d, and length L. We considered vertical nanowires with length $L = 3800$ nm and pitch $a = 700$ nm [86].

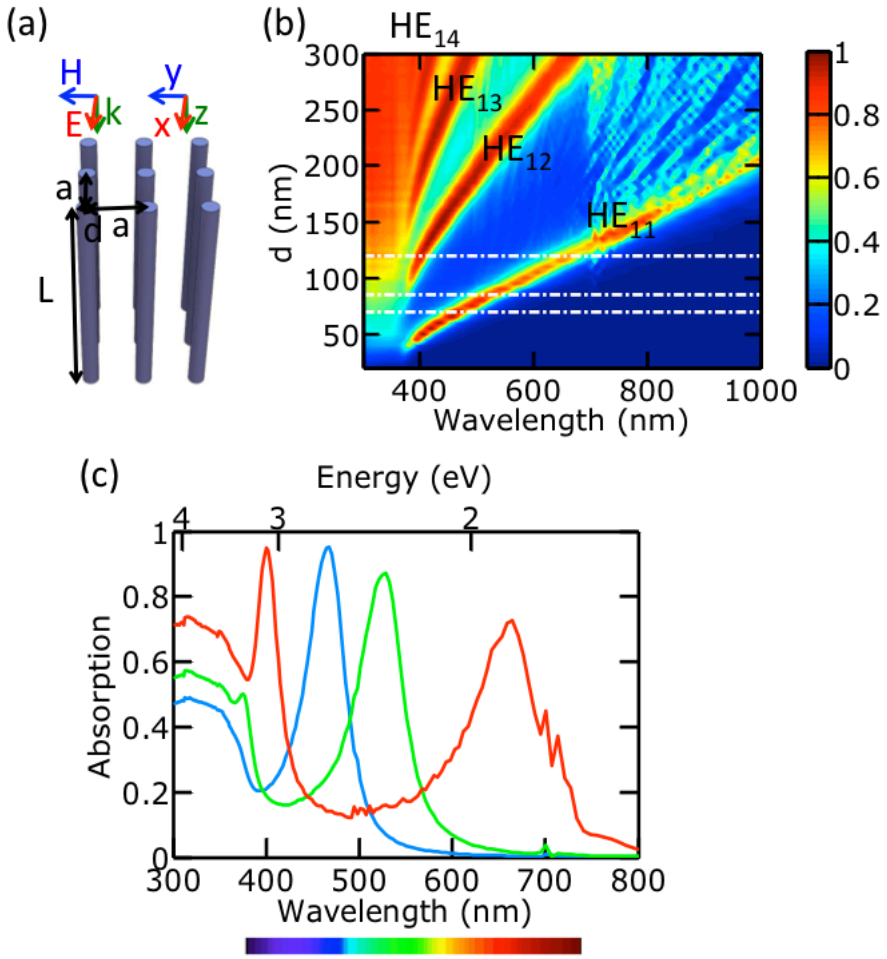

Figure 31: (a) Vertical nanowires array schematic. (b) Contour plot of absorption as a function of photon wavelength and nanowire diameter for vertical Si nanowire arrays. The dash-dotted white lines indicate nanowires illustrated in (c). (c) Absorption spectrum of nanowires with $d = 70, 85$, and 120 nm for blue, green, and red photodetectors.

Figure 31(b) utilizes a contour plot to illustrate the dependence of optical absorption on the diameter of the silicon nanowires and the photon wavelength. Due to the sub-wavelength size of the nanowires, only a few leaky modes are supported. Leaky modes in step-index optical fibers satisfy the following dispersion relation[87]:

$$\left(n_1^2\frac{J_v'(u)}{uJ_v(u)}+n_0^2\frac{K_v'(w)}{wK_v(w)}\right)\times\left(\frac{J_v'(u)}{uJ_v(u)}+\frac{K_v'(w)}{wK_v(w)}\right)= \left(\frac{1}{u^2}+\frac{1}{w^2}\right)^2\left(\frac{\beta v}{k_0}\right)^2. \quad (5.3)$$

u and w are the normalized transverse wave numbers inside and outside the cylinder: $u = \kappa\frac{d}{2} = \frac{d}{2}\sqrt{k_0^2n_1^2-\beta^2}$ and $w = \sigma\frac{d}{2} = \frac{d}{2}\sqrt{\beta^2-k_0^2n_0^2}$. n_1 and n_0 are the index of fraction inside and outside the cylinder. β is the propagation constant in the cylinder along the axis and k_0 is the wavenumber in air. Generally, u, w, and β are complex. J_v and K_v are the vth-order Bessel function of the first kind and modified Bessel function of the second kind and the prime denotes derivative with respect to its argument. $n_0 = 1$ for air and n_1 is a function of λ and complex for absorbing media. For silicon, the optical constants n_1 were taken from experimental results in Palik *et. al* [78]. The leaky modes of optical fibers are generally hybrid with both H_z and E_z components. The solutions to Eqn. 5.3 result in two classes of equations that are designated HE and EH for when the mode is TM and TE-dominant respectively. Each mode is labelled with the integer subscripts v and m where v is the order and m is the mth root of the eigenvalue equation, which also corresponds to the radial mode number. The distinct peaks in the absorption spectra correspond to particular leaky mode resonances. We find that the strongest absorptions peaks in our simulations correspond to HE_{vm} transverse resonance modes with $v = 1$.

To understand why only HE_{1m} leaky modes result in absorption enhancements, we consider the symmetry of the different modes. For incident light polarized with electric field in the x-direction, the electric field is antisymmetric under reflection about the yz plane. Only modes that are antisymmetric under mirror reflection about the yz plane can couple to this incident light. The electric fields must satisfy $\hat{O}_{M_x}\mathbf{E}(\mathbf{r}) = M_x\mathbf{E}(M_x\mathbf{r}) = -\mathbf{E}(\mathbf{r})$[88]. $\hat{O}_{M_x}$ is a mirror reflection operator about the yz plane, which operates on a vector field by applying M_x to both the input and output vector. M_x flips the x-unit vector $\hat{\mathbf{x}}$ to $-\hat{\mathbf{x}}$, while leaving $\hat{\mathbf{y}}$ and $\hat{\mathbf{z}}$ alone. E_x must be symmetric about the yz plane or equivalently, the mode must have no azimuthal symmetry. HE modes have azimuthal number $l = v-1$, while EH modes have $l = v+1$[87]. Thus, the only modes with no azimuthal variation or the proper antisymmetry

are the HE_{1m} modes. These are doubly degenerate modes that are antisymmetric about the yz or the xz plane, where one of the modes satisfies the required symmetry condition.

In Figure 31(b), additional weaker resonant modes begin to appear for nanowires larger than 120 nm diameter for $\lambda > 670$ nm. These are longitudinal resonances associated with the HE_{1m} modes and the finite length of the nanowire. Hybrid leaky modes in nanowires are characterized by propagation constant β as defined by Eqn. 5.3. Longitudinal resonances form when the guided wave picks up a round-trip phase change, $\beta_r = \frac{q\pi}{L}$ where β_r is the real part of β and q is a positive integer. At shorter wavelengths, the absorption length of silicon is small enough such that the electromagnetic field intensity decays completely by the time it reaches the end of the nanowire. The long length of the nanowires is also why the absorption enhancement from these resonances are much weaker than the transverse resonances, These longitudinal resonance modes can also couple to transverse resonance modes leading to interference between the modal fields as can be seen in the absorption spectra at larger wavelengths. since the light can make a fewer number of round trips before attenuating away.

The HE_{11} transverse resonance mode can be continuously tuned across the visible and near-infrared wavelengths and is separated from that of the HE_{12} mode by a large spectral gap. Three different nanowires indicated by the dashed white lines in Figure 31(b) are highlighted in (c) to illustrate the tunability of the HE_{11} transverse resonance mode. The blue and green resonances at 470 and 530 nm are characterized by the Lorentzian function, but the red peak at 670 nm is characterized by some small additional peaks from longitudinal resonances. Due to the large spectral gap between the HE_{11} and HE_{12} transverse resonances, the nanowires also exhibit high wavelength-selectivity. For example, the wavelength spacing between these two neighboring resonant peaks, called the free spectral range, is about 270 nm for the 120 nm diameter nanowires. The red, green, and blue photodetectors thus have minimal spectral cross talk.

In Figure 32, we plot the electric field intensity $|\mathbf{E}(\mathbf{r})|^2$ for the 120 nm diameter vertical silicon nanowire at their tranverse resonant wavelengths. The HE_{1m} modes are dipole-like and primarily dominated by the E_x component. The HE_{11} mode shown here has distinct maxima along the length of the nanowire. On the other hand, for the HE_{12} state,the ab-

sorption length for silicon at $\lambda = 400$ nm is only about 80 nm such that the guided wave attenuates rapidly and does not reach the bottom of the nanowire. While we have simulated square arrays of nanowires of a particular pitch, the HE_{11} and HE_{12} leaky modes are concentrated in and around the nanowire and thus, should not be affected by the order or position of vertical nanowires, as long as the nanowires are not too close together. When the nanowires are close, the modes couple together and the absorption peaks begin to broaden. We found that down to pitch $a \approx 500$ nm, the absorption resonances do not shift or split much. This is approximately the radial extent of the HE_{11} and HE_{12} guided resonance modes.

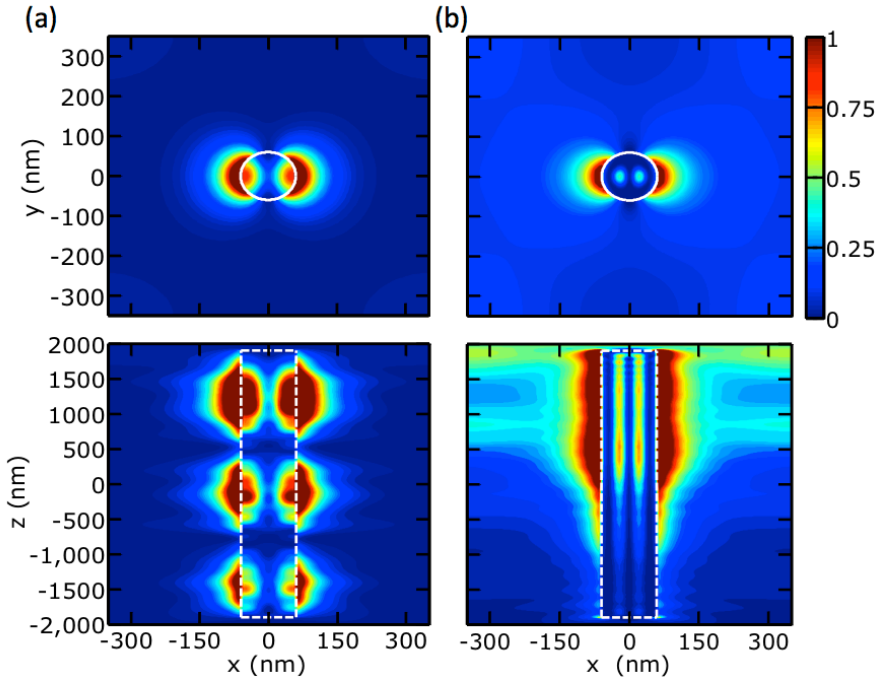

Figure 32: Electric field intensity plots of leaky mode resonances for $d = 120$ vertical nanowires at (a) $\lambda = 670$ and (b) 400 nm which correspond to the HE_{11} and HE_{12} modes respectively. The top row illustrates the top view of $|\mathbf{E}(\mathbf{r})|^2$ at $z = 0$ nm, while the bottom row shows a side view at $y = 0$. White lines indicate the edges of the nanowire.

We plot the angular dependence of the 120 nm diameter vertical nanowires for both TE and TM-polarized light for incident angle θ from 0 to 25° in Figure 33. For $\theta \leq 5°$,

the nanowires still primarily couple the to the HE_{1m} leaky modes. However, for $\theta > 5°$, other absorption peaks can be seen for both polarizations of incident light. Additional leaky modes with azimuthal mode number $l > 0$ in addition to the $l = 0$ modes are excited and thus, the absorption spectra no longer has a large free spectral range. We recently also demonstrated that tapering vertical nanowires breaks their symmetry, resulting in more broadband absorption, which is advantageous for photovoltaics [86].

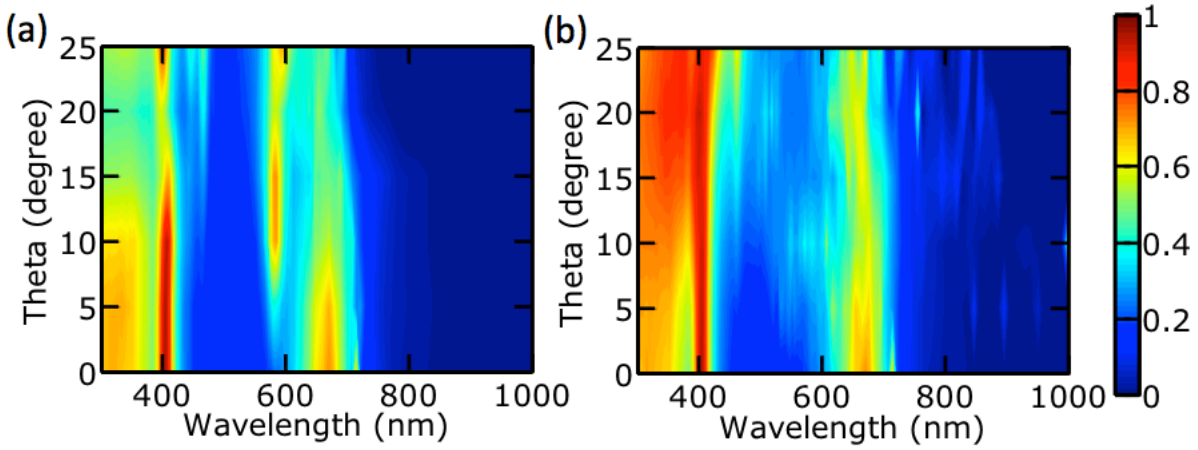

Figure 33: Angular dependence of absorption for (a) TE- and (b) TM-polarized light.

5.4.2 Conclusions

We have utilized waveguide theory to explain the spectral tunability and selectivity of absorption resonances in vertical nanowires. In particular, incident light can only couple into HE_{vm} modes where $v = 1$, resulting in distinct absorption peaks separated by a large spectral gap. This demonstrates the use of leaky mode resonances and their symmetry for engineering spectral selectivity in vertical nanowires. These mechanisms may be useful for a variety of optoelectronic applications such as photodiodes, photodetectors, phototransistors, optical modulators, optical amplifiers, light emitting diodes, and lasers.

5.5 DIELETRIC NANOSPHERE RESONANCES ENHANCEMENT

Dielectric nanospheres have emerged as a promising candidate for enhancing absorption in thin film photovoltaics. In this paper, we utilize numerical electrodynamic simulations to investigate the absorption enhancements achievable in crystalline Si (c-Si) thin films of thicknesses from 100 to 2000 nm from 2-dimensional close-packed silica (SiO_2), silicon nitride (Si_3N_4), and titania (TiO_2) nanosphere array coatings. We demonstrate that dielectric nanospheres can enhance the absorption in c-Si thin films by coupling incident light to TE waveguide modes in the c-Si thin film. While SiO_2 nanosphere arrays may achieve enhancements of less than 10% compared to ideal double pass c-Si thin films, higher index of refraction nanospheres confine light more strongly such that more nanosphere resonances may couple to waveguide modes in the c-Si.

5.5.1 Enhanced absorption with nanospheres monolayer

Two of the main approaches to wave-optics light trapping in c-Si thin film solar cells has involved (1) structuring the active region and (2) using metal nanostructures. The first approach of structuring the photoactive region may be used to tune guided mode profiles to allow for greater field concentration inside the c-Si. New c-Si structures which use this approach have been demonstrated including nanowire arrays [39–47], nanocone arrays [53, 82], nanohole arrays [54], and photonic crystals [55]. The second major approach involves the use of metal nanostructures for plasmonic light trapping through high near-fields, surface plasmon polaritons, and/or plasmonic scattering. Metal nanoparticles have been utilized to enhance optical absorption in single-crystalline silicon [89] and silicon-on-insulator [90] solar cells.

Structures such as metal gratings [91, 92], nanoparticle arrays [93], and nanogrooves [94] have also been shown to exhibit light trapping through simulations. However, both approaches to light trapping involve the use of additional manufacturing processes that may not be scalable. Metal nanostructures introduce additional reflection and parasitic absorption losses.

We demonstrate significant efficiency enhancements in c-Si thin films with high index of refraction nanosphere arrays. The nanosphere arrays allow light to couple to TE waveguide modes in the silicon. We perform simulations on close-packed silica (SiO_2), silicon nitride (Si_3N_4), and titania (TiO_2) nanosphere arrays to demonstrate that higher index of refraction nanospheres may achieve better light trapping. The higher index of reftaction nanospheres exhibit stronger optical confinement and thus, more resonance modes may couple to TE waveguide modes in the c-Si. The periodicity and nanosphere resonances introduce wave vector components along the in-plane directions, which allow light to couple to waveguide modes. We show that SiO_2 nanosphere arrays may achieve enhancements of less than 10% compared to an ideal double pass c-Si thin film. In contrast, higher index of refraction nanospheres such as Si_3N_4 may improve efficiency enhancements over 40% for c-Si thicknesses $t \leq 800$ nm and TiO_2 by over 50% for $t \leq 700$ nm. Si_3N_4 and TiO_2 nanospheres improve efficiencies by about 50% and over 100% respectively for c-Si thin films with $t = 100$ nm.

Figure 34(a) shows a schematic of our simulated structure. A close packed monolayer of nanospheres with diameters d sits on top of a crystalline silicon (c-Si) thin film of thickness t. The nanosphere monolayer forms a hexagonal lattice. The lattice vectors are defined by $|\mathbf{a}_1| = |\mathbf{a}_2| = a$, and the angle between the two lattice vectors $\varphi = 60°$. We assume the nanospheres are close-packed or $d = a$. We study a range of c-Si thicknesses t from 100 to 2000 nm (in increments of 100 nm) and nanosphere diameters d from 200 to 2000 nm (in increments of 20 nm). The c-Si sits on top of a perfectly electric conductor (PEC). We studied SiO_2, Si_3N_4, and TiO_2 nanospheres and the real part of the index of refraction n is shown in Figure 34(b). The optical constants for c-Si, SiO_2, and Si_3N_4 are taken from data in Palik's *Handbook of Optical Constants of Solids* [78]. The optical constants for TiO_2 were also taken from the same source, though the optical constants are extrapolated out to 280 nm. SiO_2, Si_3N_4, and TiO_2 have indices of refraction of approximately 1.4, 2, and 3 respectively. The SiO_2 and Si_3N_4 are amorphous, while the TiO_2 is the rutile crystal structure. The imaginary part of the index of refraction for these three materials is 0, so that the nanospheres do not absorb any light. While TiO_2 does exhibit some absorption below 440 nm, the imaginary part of the index of refraction of TiO_2 was assumed to be 0 to simplify the analysis and focus the study on the effect of index of refraction change.

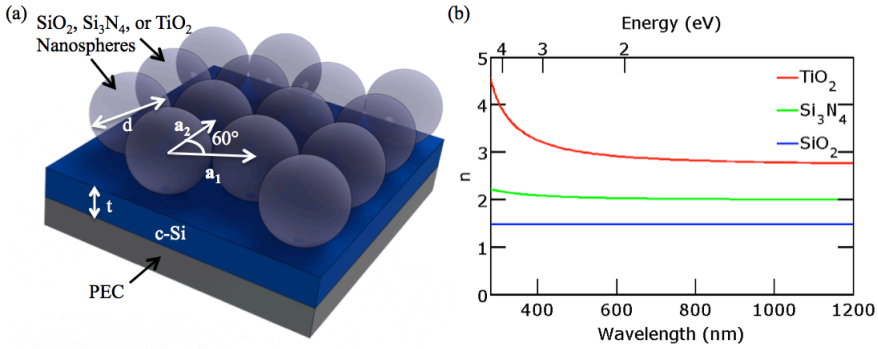

Figure 34: (a) Schematic of the dielectric nanosphere solar cell. The crystalline silicon (c-Si) thin film has thickness t and sits on top of a perfectly electrical conductor (PEC). A hexagonal close packed-monolayer of nanospheres lie on top of this thin film. The diameter of the nanospheres equals the pitch $d = a$. (b) Real part of the index of refraction n for the three nanospheres studied.

Appropriate symmetric and anti-symmetric boundary conditions were used to ensure the periodicity of the unit cell. From the simulations, we obtained the energy dependent reflection $R(E)$ and the absorption spectra was calculated from $A(E) = 1 - R(E)$. In order to evaluate the absorption performance of silicon solar cells across the solar spectrum, we calculated the ultimate efficiency from

$$\eta = \frac{\int_{E_g}^{\infty} I(E)A(E)\frac{E_g}{E}dE}{\int_0^{\infty} I(E)dE} \tag{5.4}$$

where $E_g = 1.12$ eV is the band gap of c-Si and $I(E)$ is the solar irradiance under the global 37° tilt Air Mass 1.5 spectrum [95]. We investigated the optical properties over the wavelength range from 280 to 1200 nm.

To begin with, we focused on simulating $t = 200$ nm thick c-Si thin films and SiO_2 nanosphere arrays. In these simulations, we used a uniform grid size of $5 \times 5 \times 5$ nm. Figure 35(a) illustrates the absorption spectra for a 200 nm thick c-Si film. Resonant absorption peaks are found in the c-Si thin film on metal when the following condition is satisfied

$$\tan(nkt) = -ni \tag{5.5}$$

where k is the free space wave number and n is the silicon index of refraction. The leaky modes of planar films are TEM modes labelled with mode number m as TEM_m. Interference leads to a resonant Fabry-Perot cavity effect within the film. These resonant modes are characterized by $m/2+1/4$ wavelengths in the transverse direction of the planar film, where the electric field intensity is at a maximum at the front surface and 0 at the back metal interface. The thin film absorption resonances for $m = 1$ to 4 are shown and marked with the white dotted lines. Then, we introduced SiO_2 nanospheres on top of this c-Si thin film. Figure 35(b) plots the absorption contour for the close-packed SiO_2 nanospheres as a function of diameter on top of the 200 nm thick c-Si film. Several additional absorption peaks that increase in wavelength with increasing nanosphere diameter can be seen. The best efficiency enhancement for the silica nanospheres on top of 200 nm thick c-Si is with $d = a = 900$ nm, which is indicated with the black dashed line in Figure 35(b). Figure 35(c) plots the absorption spectra for these optimized SiO_2 nanospheres in blue. The green curve shows the absorption spectra for the 200 thick c-Si film without the nanospheres. The best efficiency enhancement occurs where there are many resonances just above the Si band gap, $E_g = 1.12$ eV (or wavelengths slightly below $\lambda_g = 1110$ nm).

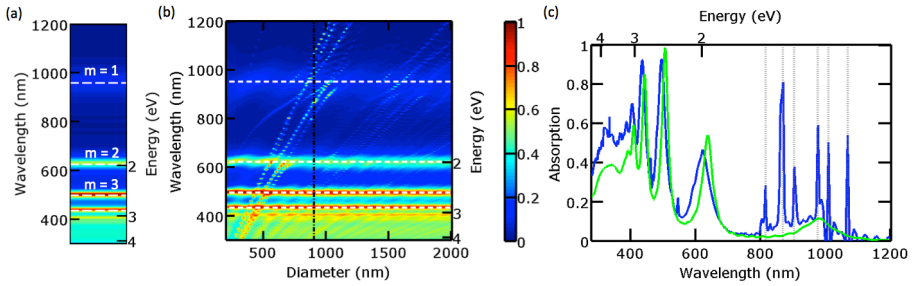

Figure 35: Absorption of (a) 200 nm thick c-Si and (b) 200 nm thick c-Si with different diameter close-packed SiO_2 nanosphere arrays on top. Thin film TEM_m modes are marked with white dashed lines. The optimal ultimate efficiency occurs for $d = a = 900$ nm, marked with the black dash-dotted line. (c) Absorption spectra of the optimal SiO_2 nanosphere array in blue compared with the absorption spectra of 200 nm thick bare c-Si.

The nanosphere coatings result in several additional resonance peaks in the absorption spectra. These resonance peaks are marked in Figure 35(c) with vertical light gray dotted lines. In order to understand the absorption enhancement at these thin films, we performed additional electric field intensity simulations. Figure 36 plots the real part of the electric field in the $x-$direction at the wavelengths associated with these modes. The incident light is polarized with electric field in the $x-$direction, and the real part of the electric field in the $x-$direction is plot at $\lambda =$ (a) 814, (b) 868, (c) 902, (d) 975, (e) 1008, and (f) 1067 nm. The top row plots a cross-section in the $x-z$ plane through the center of a nanosphere ($y = 0$ nm). The edges of the nanosphere and c-Si thin film are shown with black dashed lines. The bottom row plots a cross-section in the $x-y$ plane through the center of the silicon ($z = 100$ nm). The edges of the close-packed nanosphere array are shown with black dashed lines as well in these plots. The introduction of nanosphere arrays on the front of the c-Si thin film allows for the excitation of TE waveguide modes. In particular, the waveguide modes shown here are TE_1 waveguide modes, which are characterized by 3/4 wavelengths along the thickness of the c-Si, and E_x is a minimum at the back metal surface. Higher order TE_m waveguide modes are also excited at $\lambda = 545$ and 460 nm for $m = 2$ and 3 respectively, as can be seen in Figure 35(c) though these peaks are relatively small. Dielectric nanospheres may excite TE_m waveguide modes only, in contrast with metallic nanostructures, which can excite both TE_m and TM_m waveguide modes [92, 93]. When the reciprocal lattice vector of the nanosphere array or the k-vector of the nanosphere resonances matches the k-vector of the c-Si waveguide mode, incoming radiation may be coupled into these waveguide modes, which enables light trapping.

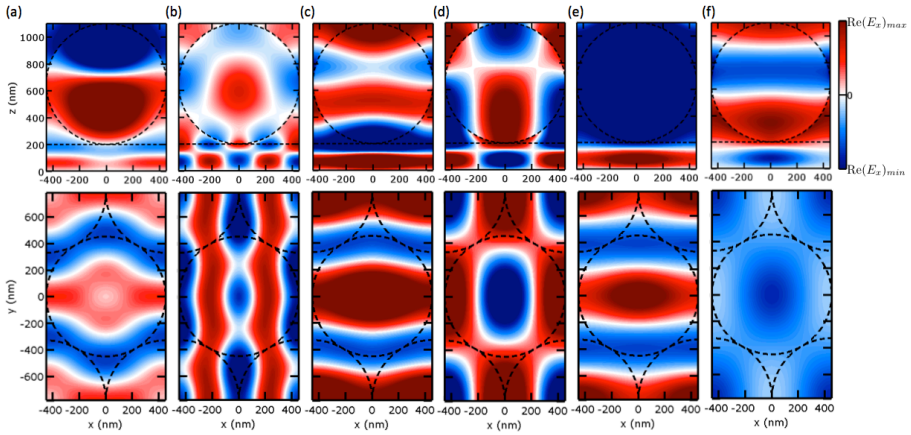

Figure 36: Real part of E_x for $\lambda =$ (a) 814, (b) 868, (c) 902, (d) 975, (e) 1008, and (f) 1067 nm. The top row plots a cross-section in the $x-z$ plane through the center of a nanosphere ($y = 0$ nm). The bottom row plots a cross-section in the $x-y$ plane through the center of the silicon ($z = 100$ nm). The edges of the close-packed nanosphere array and c-Si thin film are shown with black dashed lines. The modes shown are TE_1 waveguide modes.

Higher index of refraction nanospheres more strongly confine light so that there are more whispering gallery modes for a particular nanosphere diameter. Thus, we next investigate the absorption enhancement with silicon nitride (Si_3N_4) and titanium oxide (TiO_2) nanospheres. Figure 37(b) and (c) plot the absorption contour for close-packed Si_3N_4 and TiO_2 nanospheres respectively as a function of pitch on top of the 200 nm thick c-Si film. A larger number of optical dispersion lines corresponding to a larger number of modes appear for Si_3N_4 and TiO_2. The best efficiency enhancement for the Si_3N_4 nanospheres on top of 200 nm c-Si film is with $d = a = 720$ nm. The absorption spectrum for this structure is shown in Figure 37(c) in blue, where the green curve again shows the absorption spectrum for the 200 nm c-Si film. The best efficiency enhancement for the TiO_2 nanospheres is with $d = a = 1040$ nm. The absorption spectrum for this structure is shown in Figure 37(d) in blue, where the green curve again shows the absorption spectrum for the 200 nm c-Si film. The overall absorption is enhanced with the Si_3N_4 and even more with the TiO_2 nanospheres due to

larger number of modes present. Table 4 shows the ultimate efficiency η, short circuit current J_{sc}, and solar absorption A_{solar} of the 200 nm c-Si thin film on back metal, ideal double pass c-Si, and 200 nm c-Si with optimized SiO_2, Si_3N_4, and TiO_2 nanospheres. The short circuit current is calculated from $J_{sc} = q\int_{E_g}^{\infty} b_s(E)A(E)dE$ and the solar absorption from $A_{solar} = \int_{E_g}^{\infty} b_s(E)A(E)dE$ where $b_s(E)$ is the photon flux density of the global Air Mass 1.5 spectrum [95].

The absorption of the ideal double pass thin film is

$$A(E) = 1 - \exp[2\alpha(E)t] \tag{5.6}$$

where $\alpha(E)$ is the energy dependent absorption coefficient of c-Si. The ideal double pass thin film assumes perfect antireflection at the front surface, $R(E) = 0$, and perfect reflection at the back surface, $R(E) = 1$. All nanosphere coatings exhibit light trapping properties with better absorption and ultimate efficiency than the ideal double pass and thin film Si. We also show in Table 4 the efficiency enhancements G_1 and G_2 of the various structures to thin film c-Si and ideal double pass c-Si respectively. Efficiency enhancements of over 50% or more are possible with Si_3N_4 and TiO_2 nanospheres compared to the ideal double pass c-Si thin film.

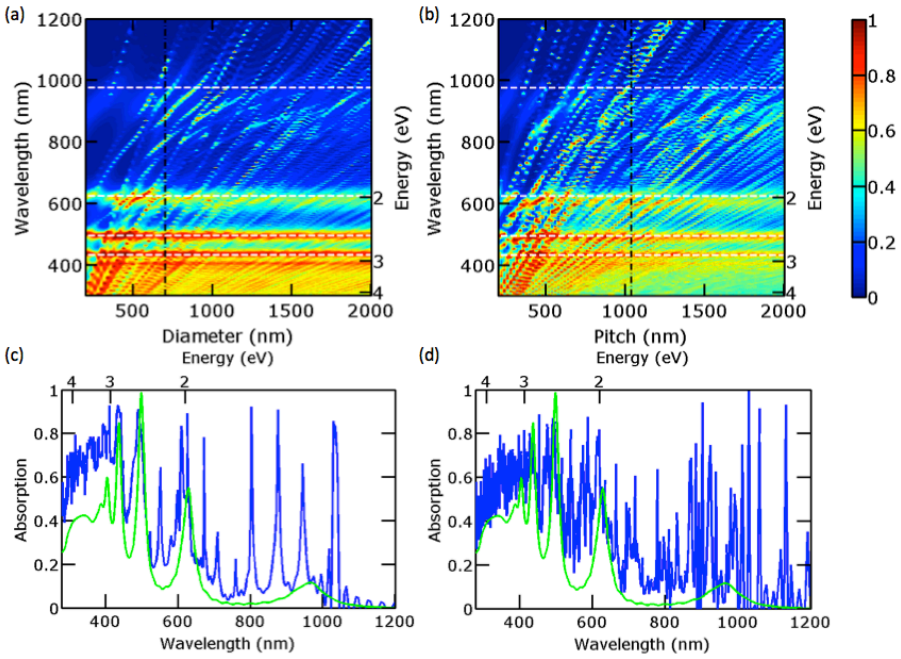

Figure 37: Absorption of 200 nm thick c-Si with different diameter close-packed (a) Si_3N_4 and (b) TiO_2 nanosphere arrays on top. The optimal ultimate efficiency occurs for $d = a = 700$ nm and for $d = a = 1040$ nm for the Si_3N_4 and TiO_2 nanospheres respectively, which is marked with the black dash-dotted lines. Absorption spectra of the optimal (c) Si_3N_4 and (d) TiO_2 nanosphere arrays in blue compared with the absorption spectra of 200 nm thick bare c-Si.

Table 4: Comparison of the performance of 200 nm c-Si film on metal under different photon management schemes. η (%), J_{sc} (mA/cm^2), A_{solar} (%), and G_1, G_2.

Structure	$\boldsymbol{\eta}$	$\boldsymbol{J_{sc}}$	$\boldsymbol{A_{solar}}$	$\boldsymbol{G_1}$	$\boldsymbol{G_2}$
Thin Film	8.0	7.2	10.4	1.00	0.80
Ideal Double Pass	10.0	9.0	13.0	1.25	1.00
With SiO_2 Nanospheres	11.1	9.9	14.2	1.38	1.10
With Si_3N_4 Nanospheres	15.1	13.5	19.4	1.88	1.50
With TiO_2 Nanospheres	17.5	15.6	22.1	2.18	1.74

Finally, we evaluated the efficiency enhancements possible with nanosphere coatings over a range of c-Si thicknesses from $t = 100$ to 2000 nm. These simulations were performed with a uniform grid size of 20 $\times$ 20 $\times$ 20 nm, due to the large number of simulations that were performed. The ultimate efficiency was found to have converged within 2% with this grid size. Figure 38(a), (b), and (c) utilize contour plots to illustrate the dependence of ultimate efficiency on the thickness of the c-Si and nanosphere diameter (which equals the pitch) of the SiO_2, Si_3N_4, and TiO_2 nanosphere arrays respectively. The optimal ultimate efficiencies for each thickness of c-Si are marked with black circles in the contour plots. Figure 38(d) plots the optimum diameter for each c-Si thickness for the three different types of nanospheres. The best diameter for the SiO_2 nanospheres is about 900 nm and TiO_2 nanospheres is about 800 nm across the different thicknesses evaluated, while for for Si_3N_4, the best diameter tends to increase with increasing c-Si thickness. In addition, based on the contour plots, we note that the efficiency is not that sensitive to the nanosphere diameter so long as the nanospheres are larger than some minimum diameter (about 700 nm).

In Figure 38(e), we plot the best ultimate efficiencies of the c-Si thin film, ideal double pass c-Si, and the best nanosphere coatings as a function of c-Si thickness. The short-circuit current is plot on the right y-axis. The optimal ultimate efficiency enhancement G_2 of the different types of nanosphere coatings compared to the ideal double pass c-Si thin film are plot in Figure 38(f) for different c-Si film thicknesses. While the efficiency enhancement for SiO_2 is under 10% for all c-Si thicknesses, Si_3N_4 nanospheres may improve efficiencies by over 40% for c-Si thicknesses $t \leq 800$ nm and TiO_2 nanospheres by over 50% for $t \leq 700$ nm. The efficiency improvements decrease for larger c-Si thicknesses and are 1%, 23%, and 24% for SiO_2, Si_3N_4, and TiO_2 respectively for $t = 2000$ nm. These simulations suggest that high index of refraction nanospheres may exhibit better light trapping properties than metal nanostructures, which have demonstrated enhancements of 43% in 50 nm [92] and 22% in 100 nm [93] thick c-Si. While metal nanostructures may enhance absorption by coupling incoming light into both TE_m and TM_m waveguide modes as well as the excitation of localized surface plasmon resonances, they also exhibit parasitic absorption and enhanced reflection.

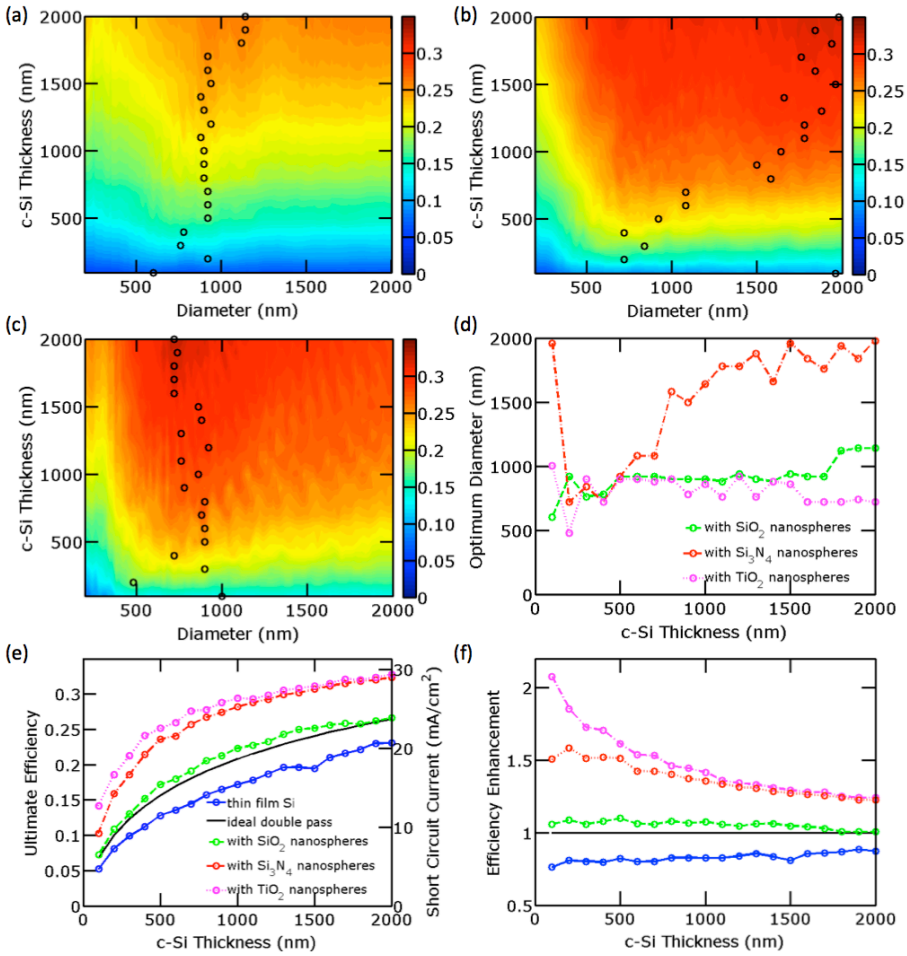

Figure 38: Ultimate efficiency η of c-Si thin film with (a) SiO_2, (b) Si_3N_4, and (c) TiO_2 close-packed nanospheres as a function of the c-Si thickness t and diameter d (which equals the pitch a). The maximum efficiency of the solar cells for each thickness is shown with black circles. (d) Optimum diameter for different thicknesses of c-Si. (e) The maximum ultimate efficiency of various thickness c-Si solar cells as compared to an ideal double pass c-Si thin film and thin film c-Si on top of a perfect reflector. The short circuit current is shown on the right y-axis. (f) The ultimate efficiency enhancement G_2 from nanosphere coatings as compared to the ideal double pass thin film.

5.5.2 Fabrication of nanosphers layers

We developed a new self-assembly method shown in Figure 39, whereby we can coat different layers of nanospheres onto large area solar cells. This slide shows our self-assembly method. The n anospheres with methanol and deposit the solution into water. The nanospheres float on top of the water and form a close packed monolayer. By dipping our silicon substrate into the nanospheres and than gently pulling the wafer out of the solution, we can form a monolayer of nanospheres over large areas. This self assembly method can be applied on different nanospheres and microspheres such as polystyrene (PS) and silica.

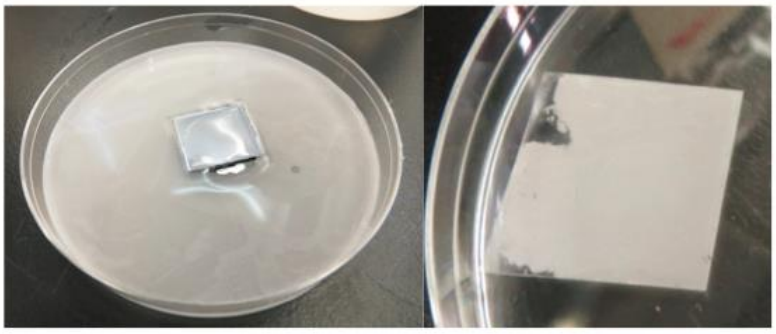

Figure 39: Self-assembly method.

Figure 40 shows monolayer SEM pictures of (a) PS and(b) silica. The results are with good uniformity and the nanosphere coating is close packed with some point defects, which are missing nanospheres, and some grain boundaries.

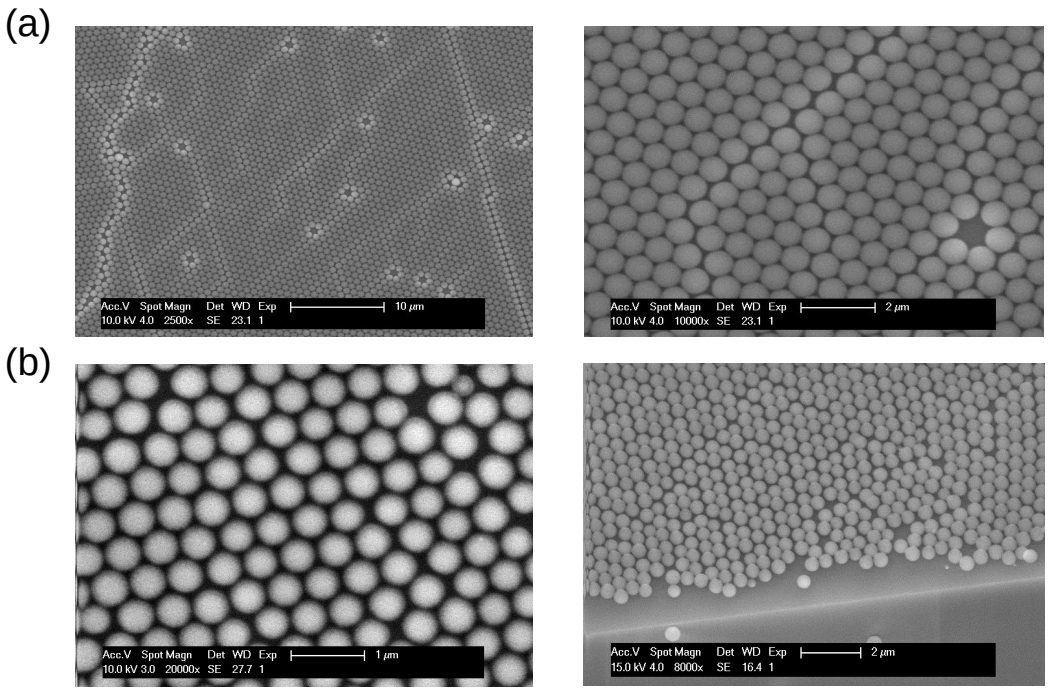

Figure 40: Monaolyer coatings of different nanosphers, (a) PS nanospheres and (b) silica nanospheres.

By repeating the process multiple times, we can obtain multiple layers with good repeatability and uniformity. The left side shows 3 layers and the right side shows 5 layers as shown in Figure 41

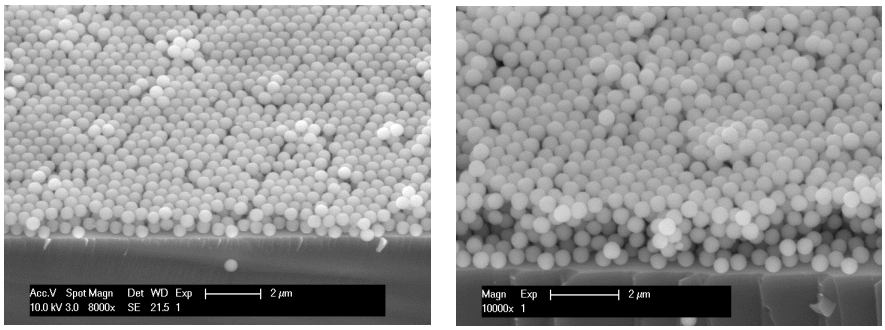

Figure 41: Multiple layers of nanosphere coatings. 2 layers (left) and 5 layers (right).

More importantly, we can also coat flexible substrates with the nanospheres. Here, in Figure 42 we present our results on plastic polyethylene terephthalate (PET) substrates. This result means we can do the self assembly process on ultrathin silicon film which is usually flexible.

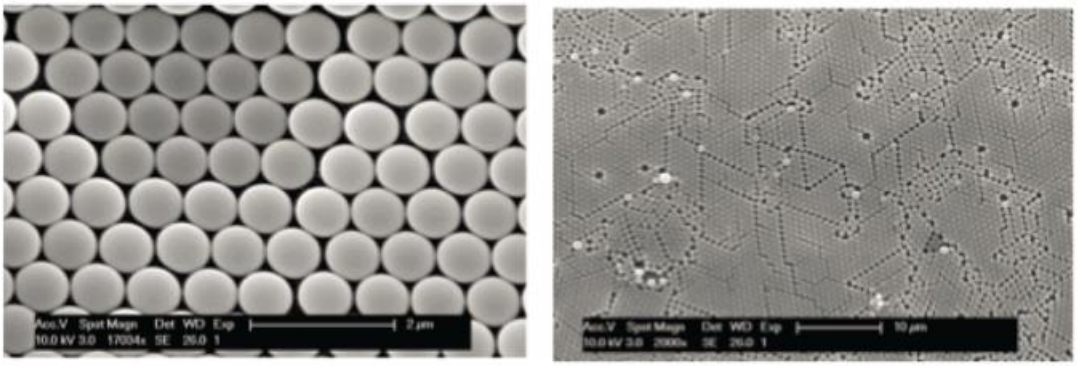

Figure 42: Nanospheres coated onto flexible PET substrates.

5.5.3 Conclusions

We investigated 2-dimensional periodic closed-packed SiO_2, Si_3N_4, and TiO_2 nanosphere arrays on c-Si thin films for enhancing the absorption in the c-Si photoactive region. By evaluating the electric field of absorption peaks in the nanosphere coated systems, we demonstrate that enhanced light trapping is due to the coupling of incident light to waveguide modes. We demonstrate that higher index of refraction nanospheres may achieve better light trapping since they have more resonant modes due to stronger optical confinement. Enhancements over 100% can be obtained on 100 nm thick c-Si films with TiO_2 nanospheres, though the enhancements decrease with thicker cells. This light trapping mechanism improves efficiencies without introducing new surfaces or interfaces that increase surface recombination as exhibited by other nanophotonic or plasmonic light trapping strategies. And the monolayer structures can be fabricated with facile and scalable methods.

5.6 LIGHT TRAPPING IN PHOTONIC CRYSTAL

Recently, the author Chen's group has demonstrated the ability to fabricate photonic crystal templates through interference lithography and one or two laser exposures, akin to traditional photolithography processes [96–98]. These templates may be used to form woodpile (WP) or inverse woodpile (IWP) photonic crystals by infiltrating the polymer with nanocrystalline silicon (nc-Si) which has a similar band gap and higher effective absorption coefficient compared with crystalline Si [99]. Therefore, we present detailed numerical electrodynamic investigations of WP and IWP photonic crystal nc-Si solar cells for a variety of geometries and compare them to thin film structures. We analyze the achievable absorption enhancement across the solar spectrum and found these structures exhibit improved light trapping over thin film structures.

5.6.1 Inverse woodpile and woodpile structures

Figure 43 shows schematics of the (a) IWP and (b) WP photonic crystal structures studied. The active layer consists of nanocrystalline silicon (nc-Si) placed on top of a perfectly electric conductor (PEC). The IWP photonic crystal is formed by stacking N layers of air cylinders in nc-Si, where each layer is rotated by 90° from the layer below. N is constrained to be an integer. The stacking pattern is a four layer sequence where the third and fourth layers have the same orientation as the first and second layers respectively, but are offset by half of the horizontal lattice constant. The WP photonic crystal has the same stacking pattern, but consists of a lattice of nc-Si cylinders surrounded by air.

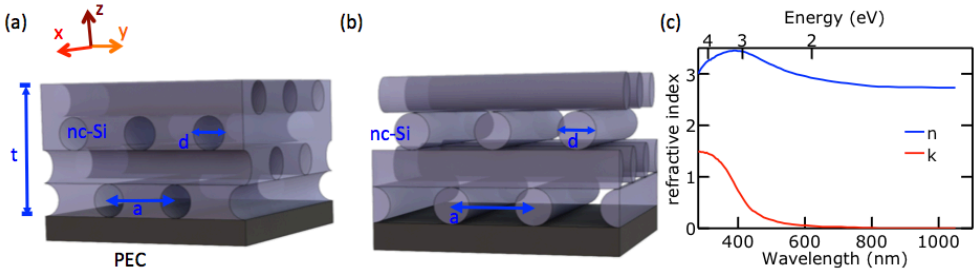

Figure 43: Schematic of the (a) inverse woodpile photonic crystal structure and (b) woodpile photonic crystal structure. (c) Optical constants of nanocrystalline silicon.

The parameters of the structures are the horizontal period a of the lattice, the diameter d of the cylinders, and the total thickness t. $t = Nd$. The diameters of the cylinders are smaller than or equal to the horizontal lattice period, $d \leq a$. The thickness L of a thin film with the same amount of nc-Si (or equivalent thickness) as the IWP and WP structures are

$$L = Nd - \frac{N}{a}\frac{\pi d^2}{4} \tag{5.7}$$

and

$$L = \frac{N}{a}\frac{\pi d^2}{4}, \tag{5.8}$$

respectively.

We employed the finite difference time domain method for solving Maxwell's equations. The optical constants of the nc-Si used in this work are shown in Figure 43(c) [100]. The solar absorption, ultimate efficiency, and short circuit current density were evaluated under the global 37° tilt Air Mass 1.5 spectrum [95] using the same formulas as those we have previously used. The ultimate efficiency describes the cell efficiency when each photon absorbed produces one electron-hole pair, and these photoexcited carriers are collected without recombination such as when the temperature of the cell is 0 K. The short circuit current is calculated under the same assumptions. The band gap of nc-Si is $E_g = 1.12$ eV.

We evaluated the optical properties of the IWP and WP structures over the energy range of the solar spectrum from 1.12 to 4.4 eV (wavelengths from 1100 to 280 nm). A uniform mesh of 10 nm $\times$ 10 nm $\times$ 10 nm was utilized where the ultimate efficiency was found

to have converged within 1%. Perfectly matched layer and PEC boundary conditions were used for the upper and lower boundary of the simulation cell, respectively [34]. Appropriate boundary conditions were used for the side boundaries to model the periodic nature of the arrays. The optical spectra of the photonic crystals were averaged for light polarized in the $x-$ and $y-$directions.

For this study, we first focused on the equivalent thickness $L = 200$ nm and optimized the number of layers N, pitch a, and diameter d of the IWP and WP structures for the maximum solar absorption or equivalently, ultimate efficiency. The constraint of comparing structures with the same equivalent thickness (as defined by Equations 5.7 and 5.8 for the IWP and WP structures, respectively) result in a series of contour lines as shown in Figure 44. The ultimate efficiency of the simulated structures is plotted on these contour lines for various number of layers N, diameters d, pitches a. The region of the parameter space that does not satisfy the constraint $d \leq a$ is shaded with gray. Figure 44(a) shows the results for the IWP structure for $N = 1$ to 4. The optimal IWP structure is $N = 2$, $a = 390$ nm, and $d = 140$ nm where the ultimate efficiency is 25.8%. Figure 44(b) shows the results for the WP structure, where the optimal structure is $N = 6$, $a = 1600$ nm, and $d = 260$ nm, where the ultimate efficiency is 30.1%. The IWP structure is very sensitive to number of layers and morphology, whereas the WP structure has a broad range of layers and morphologies which perform close to the optimum. The WP structures have ultimate efficiencies $> 27.0\%$ for $N = 2$ to 7 with a broad range of pitches and diameters. The ultimate efficiency is not very strongly dependent on pitch when the pitch is large as the cylinders are far from each other horizontally.

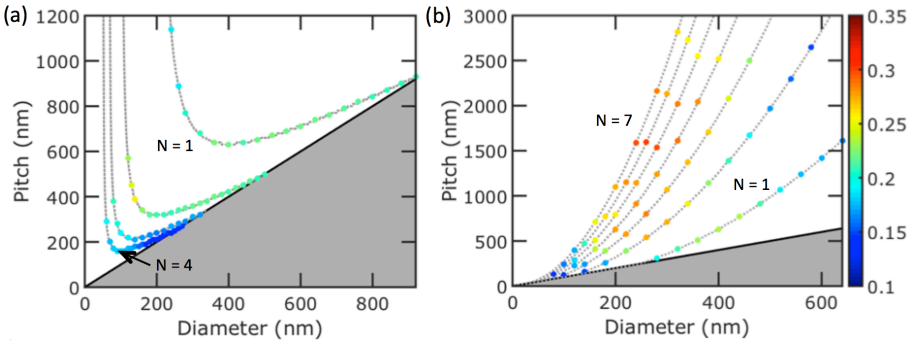

Figure 44: Scatter plots of ultimate efficiency for different (a) IWP and (b) WP structures subject to the constraint that $L = 200$ nm and $d < a$.

Figure 45 plots the absorption spectra as a function of energy, $A(E)$, for the (a) optimal IWP structure, (b) optimal WP structure, and (c) 200 nm nc-Si thin film. The absorption spectra was calculated by $A(E) = 1 - R(E)$. The IWP structure may be approximated as a thin film waveguide of thickness $t = Nd = 280$ nm on metal with an effective index of refraction. The effective index of refraction is the volumetric averaged index of refraction. For a thin film on metal, the leaky TE modes satisfy

$$k_{2x} \cot(k_{2x} t) = i k_{1x} \tag{5.9}$$

and the leaky TM modes satisfy

$$i k_{2x} \tan(k_{2x} t) = n_2^2 k_{1x} \tag{5.10}$$

where $k_{1x} = \left[k_0^2 - \beta^2\right]^{1/2}$ and $k_{2x} = \left[(n_2 k_0)^2 - \beta^2\right]^{1/2}$. k_{1x} is the transverse component of the wavevector outside the semiconductor, while k_{2x} is the transverse part of the wavevector inside the semiconductor. n_2 is the effective index of refraction of the nanocrystalline silicon based on its volumetric fill factor. k_0 is the free space wave number. The dispersion relation of various TE and TM leaky (or quasi-guided) modes are shown in Fig 45(a)(ii). The light lines for the air and the effective index of refraction material are also shown. The horizontal

gray dashed lines correspond to the magnitude of the reciprocal lattice vectors of the photonic crystal square lattice

$$k = \sqrt{\left(\frac{2\pi m}{a}\right)^2 + \left(\frac{2\pi p}{a}\right)^2} \tag{5.11}$$

where m and p are integers. When the wavevector of a leaky mode β is equal to the reciprocal lattice vector, normally incident light can couple into the leaky mode and there is an absorption peak. The photon energies where this occurs at for energies below 2.1 eV are shown with the green dashed lines at the bottom of Figure 45(a)(i).

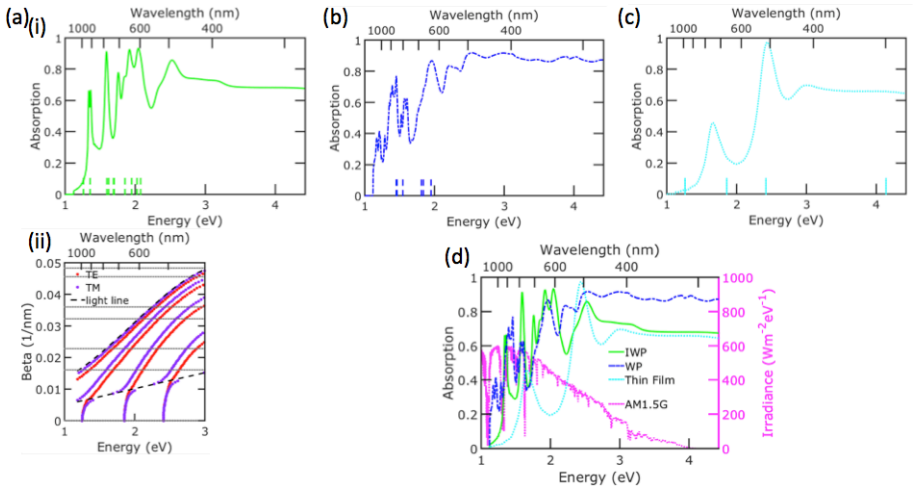

Figure 45: Absorption spectra of three different nc-Si structures: (a) IWP with $N = 2$, $a = 390$ nm, and $d = 140$ nm, (b) WP with $N = 6$, $a = 1600$ nm, and $d = 260$ nm, and (c) thin film with $L = 200$ nm. The dispersion relation of the leaky or quasiguided modes of a thin film with volumetric averaged index of refraction is shown in (a)(ii). (d) The three absorption spectra are plotted together with the irradiance of the Air Mass 1.5 global solar spectrum shown on the right y-axis.

In contrast, for the WP photonic crystal, the absorption peaks are related to the leaky resonant modes in a cylinder. The leaky TE modes may be calculated from

$$\frac{J'_m(n_2 k_0 d/2)}{n_2 J_m(n_2 k_0 d/2)} = \frac{H'_m(k_0 d/2)}{H_m(k_0 d/2)} \tag{5.12}$$

and the leaky TM modes may be calculated from

$$n_2 \frac{J'_m(n_2 k_0 d/2)}{J_m(n_2 k_0 d/2)} = \frac{H'_m(k_0 d/2)}{H_m(k_0 d/2)} \tag{5.13}$$

where J_m and H_m are the mth order Bessel and Hankel functions of the first kind, respectively [83]. The prime denotes differentiation with respect to the arguments. The location of the TE and TM modes below 2.1 eV are shown with blue dashed lines at the bottom of Fig 45(b). The lowest energy modes are the TE_{11} and TM_{01} modes at 1.45 and 1.54 eV, respectively. These modes couple to one another since the n-Si cylinders are stacked on top of one another, resulting in resonance modes that are closer to the band gap. This mode coupling is also mostly independent of pitch, as long as the cylinders are not that close to one another, since this is a horizontal pitch, and thus the absorption spectrum and ultimate efficiency is thus also largely independent of pitch, as shown in Figure 44(b).

Figure 45(c) plots the absorption spectrum for the 200 nm thick c-Si thin film. The absorption peaks are Fabry-Perot TEM modes which satisfy Eqs. 5.9 and 5.10 when $\beta = 0$. The location of the TEM are shown with cyan dashed lines at the bottom of Fig 45(c). The numerically simulated resonances correspond well to the analytical solution, but are slightly red-shifted due to numerical error. Figure 45(d) plots all the absorption spectra together for comparison. The irradiance of the Air Mass 1.5 global solar spectrum is shown in the right y-axis.

Table 5 lists the fraction of photons absorbed in different regions of the solar spectrum for the three structures shown in Figure 45. The infrared (IR) region (above the nc-Si band gap) is from 1.12 to 1.67 eV (1107 to 740 nm), the visible (Vis) region is from 1.67 to 3.1 eV (740 to 400 nm), and the ultraviolet (UV) region is from 3.1 to 4.43 eV (400 to 280 nm). The total absorption shown only includes the range above the nc-Si band gap energy from 1.12 to 4.43 eV (1100 to 280 nm). The IWP and WP structures have significantly improved performance in the IR region compared with the nc-Si thin film due to better light trapping. The photonic crystals also both have a lower effective index of refraction such that reflection is decreased. The WP structure also has almost double the absorption of the thin film in the ultraviolet region region due to better antireflection properties.

Table 5: % of absorption in different regions of the solar spectrum. The infrared and total solar regions are calculated only for energies above the nc-Si band gap ($E > 1.12$ eV).

Structure	**IR**	**Vis**	**UV**	**Total**
IWP	30.1	72.5	69.9	52.6
WP	44.6	75.3	88.0	61.3
Thin Film	11.3	66.9	44.5	29.7

Table 6 lists the total solar absorption, A_{sol} (%), short circuit current density J_{sc} (mA/cm^2), and the ultimate efficiency η (%) of these structures. The total solar absorption shown in this table is over the entire solar spectrum and not just over energies above the silicon band gap as shown in Table 5. The solar absorption of the silicon thin film ideal single pass is 18.8%. The best IWP structure has a solar absorption of 33.3%, which is a 77.1% enhancement over the thin film structure. The absorption of the WP is 106% higher than that of thin film structure.

Table 6: The total solar absorption, A_{sol} (%), short circuit current density J_{sc} (mA/cm^2), and the ultimate efficiency η (%).

Structure	$\boldsymbol{A_{sol}}$	$\boldsymbol{J_{sc}}$	$\boldsymbol{\eta}$
IWP	33.4	23.1	25.8
WP	39.0	26.9	30.1
Thin Film	18.8	13.0	14.6

And then we investigated other equivalent thicknesses, L = 400 nm, 600 nm and 800 nm on inverse woodpile, woodpile and thin film structures. The optimal results of three different structures against thickness is plotted in Figure 46

We next investigate the loss associated with a real back reflector metal by replacing the PEC boundary condition with a flat silver layer on the bottom of the inverse woodpile

structure. A real metal will introduce additional parasitic losses due to absorption in the metal as compared to a PEC. The position dependent absorption per unit volume was calculated from divergence of the Poynting vector normalized over the incoming radiation power, and the absorption in the nc-Si active region was obtained by integrating the position dependent absorption per unit volume over the Si volume. The absorption spectrum of the structure with the silver back contact is shown in Figure 47 along with that with the PEC boundary condition. The absorption is the average for light polarized in the x- and y-direction. As can be seen in this Figure, the absorption in the silicon photonic crystal with the silver back contact is similar to that with a PEC, except for some additional loss in the high energy (short wavelength) range. We observe only a small reduction in solar absorption from 20.9 to 19.1% with the utilization of silver.

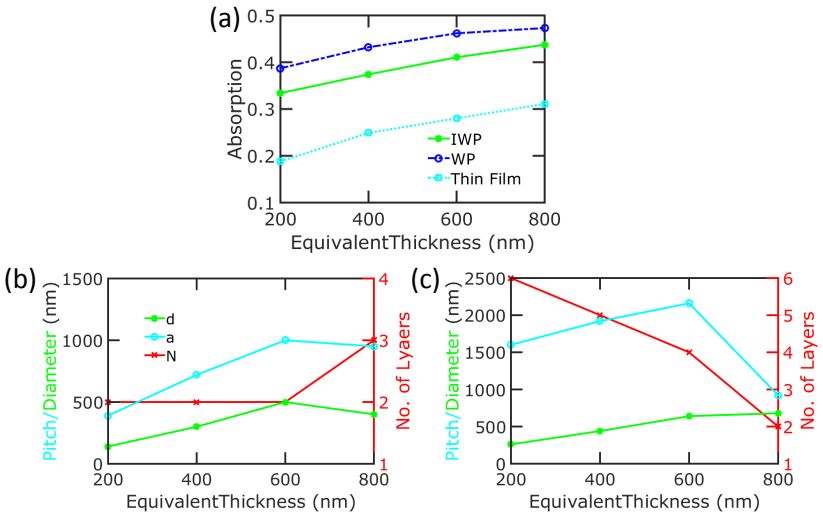

Figure 46: (a) Integrated absorption and (b)(c) optimal geometries of three different structures against equivalent thicknesses.

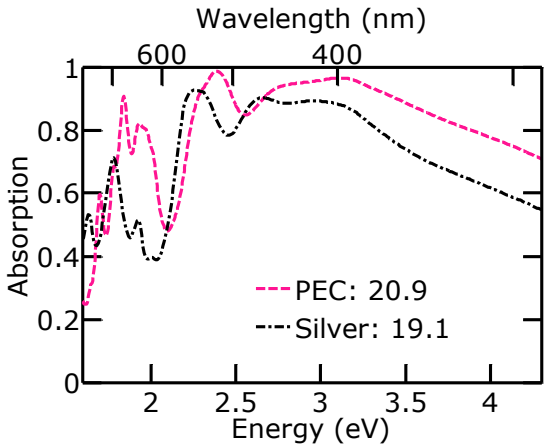

Figure 47: (a) Comparison of absorption in the inverse woodpile structure with antireflection coating with PEC and silver back contact. The solar absorption in the structure with PEC back contact is 20.9%. When the Ag back contact, the solar absorption is reduced to 19.1%.

Finally, we simulated the angular dependence of the absorption spectrum for the optimal thin film and inverse woodpile structure. Figure 48 plots the solar absorption for TE and TM polarized incident light for these two structures. For the inverse woodpile structure, the TE results are the average for the electric field fixed along the x-direction and the y-direction. Similarly, the TM results are the average for the magnetic field fixed along the x-direction and y-direction. It can be seen that there is little variation in absorption with zenith angle up to about 40°. The TM results are slightly better than the TE results except for very high incidence angles. The short circuit current density is shown on the right y-axis.

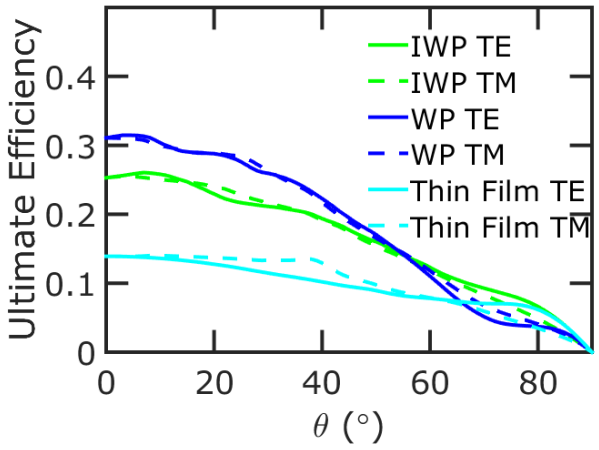

Figure 48: Solar absorption as a function of zenith angle θ for thin film and inverse woodpile structure with Si_3N_4 layer. The short circuit current density is shown on the right y-axis.

The scatter plots of ultimate efficiency for IWP and WP with other different equivalent thicknesses L = 400 nm, 600 nm and 800 nm are shown in Figure 49. It shows that IWP and WP strutures always have better performance than thin film structure.

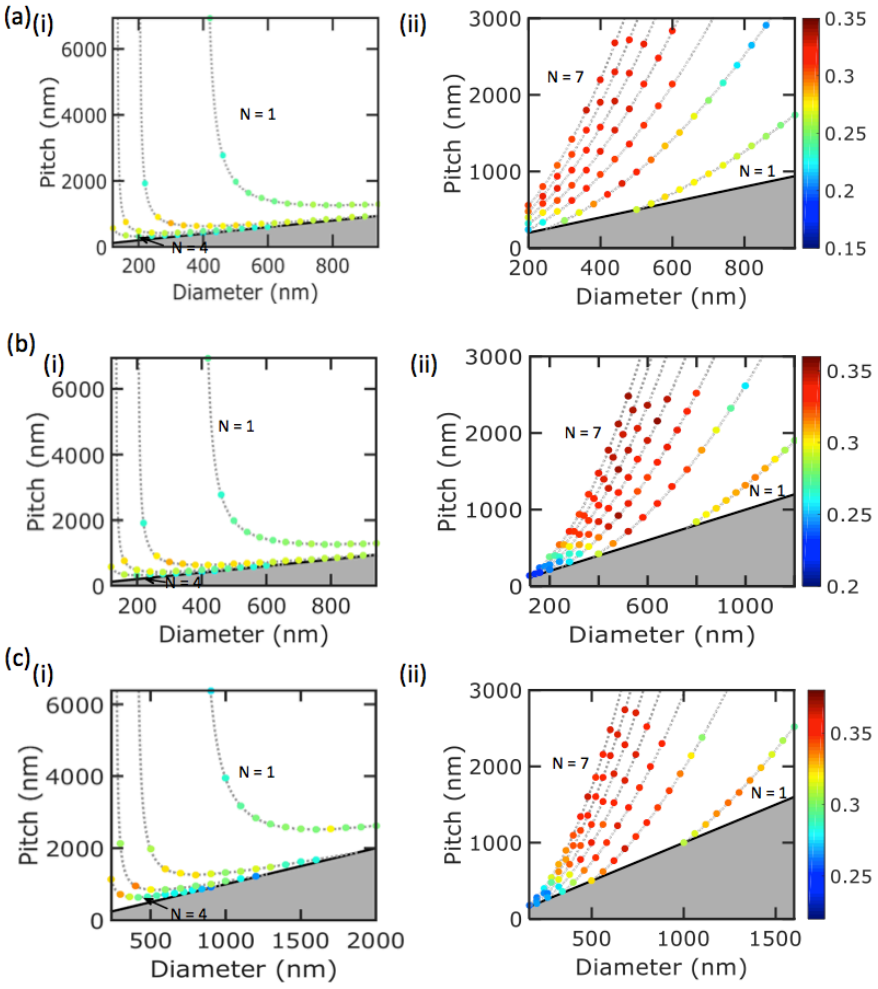

Figure 49: Scatter plots of ultimate efficiency for (i) IWP and (ii) WP structures subject to constraint that (a) L = 400 nm, (b), L = 600 nm, and (c) L = 800 nm.

In summary, we report that the solar absorption in nanocrystalline silicon may be improved by structuring the active region into an inverse woodpile photonic crystal. The photonic density of states may be engineered such that there is a strong absorption enhancement in the infrared range, where the absorption is about 3 times that in the thin film. We demonstrate that the performance with a real metal as opposed to a PEC is about the same and that the enhancement is over a broad range of incidence angles. This study demonstrates a new structure for light trapping over a broad range of photon energies and incidence angles.

6.0 PERFORMANCE ENHANCEMENT IN ULTRATHIN SILCON SOLAR CELLS

6.1 ULTRATHIN SILICON FILM FABRICATION

KOH etching is an approach to get ultrathin silicon films, with this method we can get large area silicon thin films with different thicknesses. Etch rate of KOH on (1 0 0) or (1 1 0) directions silicon is quite well studied. In my experiments, we use 45% KOH solution, and the etch rate is mainly dependent on temperature as shown in Figure 50, so through controlling the temperate of KOH solution, we can control the final thickness of silicon film by changing the etch time. The etch rate can be as slow as several nanometers per minute, so controlling the thickness of silicon thin film in nanometer scale is quite possible.

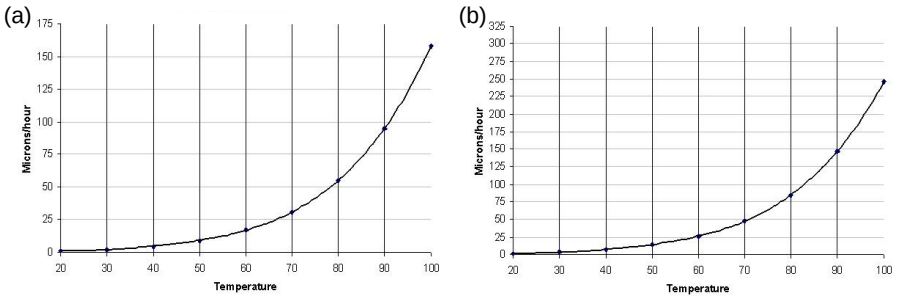

Figure 50: 45% KOH etch rate on (a) (1 0 0) and (b) (1 1 0) directions.

And Figure 51 shows the results from KOH etching. We get different thicknesses silicon thin film and the surface quality after etch is also shown.

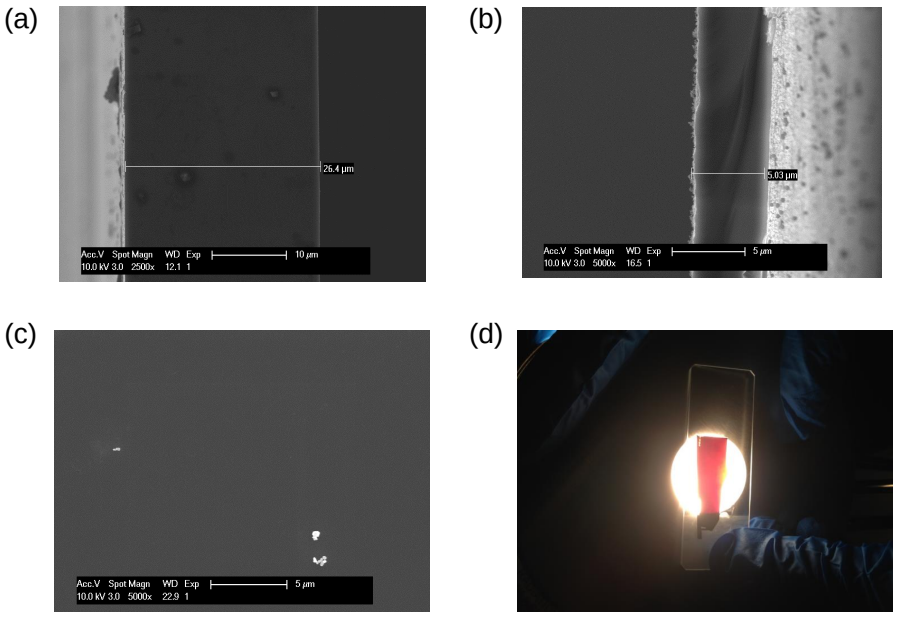

Figure 51: Etched silicon films with different thickness (a) 26.4 μm and (b) 5 μm. (c)Shows the good surface quality after KOH etch. (d) is the optical photo of silicon thin film with 5 μm thickness.

6.2 BROADBAND LIGHT ABSORPTION ENHANCEMENT IN ULTRATHIN FILM CRYSTALLINE SILICON SOLAR CELLS WITH HIGH INDEX OF REFRACTION NANOSPHERE ARRAYS

Based on what we have demonstrated through simulations that high index of refraction dielectric nanospheres (NSs) on the frontside of c-Si thin film structures can improve efficiencies substantially by coupling incident light into the underlying absorber layer [101]. This approach of light trapping differs from other approaches such as structuring the active material or using metal nanostructures in that no new surfaces or interfaces are created. Dielectric nanosphere arrays can be scalably coated onto large area solar cells with a variety of nanosphere lithography approaches as shown previously. Finally, we demonstrate significant

efficiency and external quantum efficiency (EQE) enhancement on ultrathin c-Si solar cells of 15 μm thickness via nanosphere coatings [102].

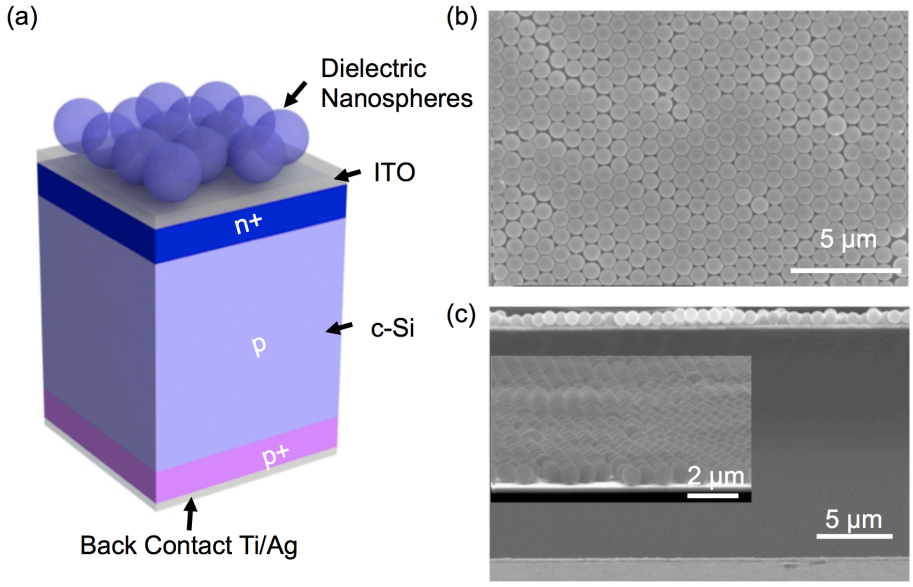

Figure 52: (a) Schematic of the dielectric nanosphere solar cell. A hexagonal close packed-monolayer of PS NSs lies on top of this solar cell. (b) Top view SEM image of the PS NSs on Si solar cell. (c) Cross section view of the solar cell with PS NSs monolayer on top. The inset shows a high magnification view of of the NSs at 80°.

Figure 52(a) shows a schematic of our ultrathin film c-Si solar cell structure which consists of a c-Si film between an indium tin oxide (ITO) front transparent electrode and a Ti/Ag back contact. The c-Si layer is doped n+, p, and p+ from top to bottom. In order to demonstrate the advantages of nanosphere arrays, a close packed hexagonal lattice monolayer of polystyrene (PS) NSs is coated on top of the c-Si thin film solar cell. Figure 52(b) shows a scanning electron microscope (SEM) image of the the top view of the PS NS hexagonal array. The NS layer is close packed and uniform over the solar cell. Figure 52(c) shows a cross section SEM image of the solar cell. The c-Si film is about 15 μm thick and the ITO thin film is about 200 nm thick. The ITO has about 85% transparency with sheet resistance $R_s \approx 30 - 40\ \Omega$/sq.

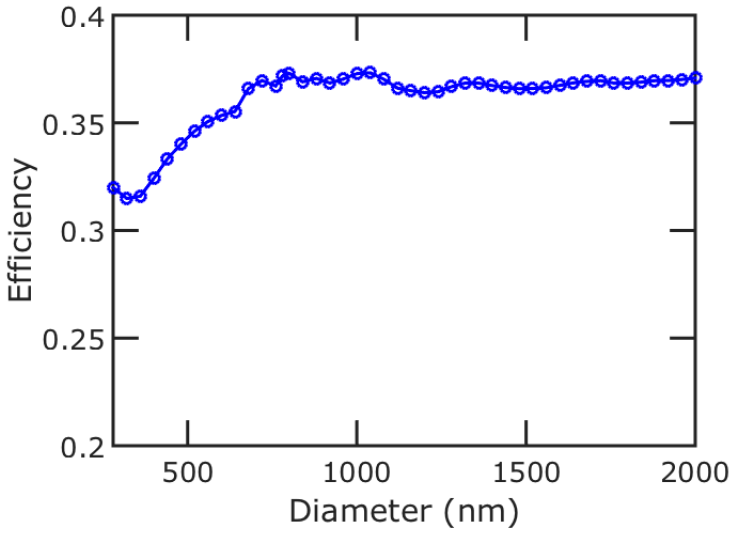

Figure 53: Simulated ultimate efficiencies of c-Si solar cells as a function of PS NS diameter.

We studied the effect of different diameter PS NS arrays from 280 nm to 2000 nm by simulations. The back contact is modeled with a perfectly electric conductor boundary condition and the PS NS array sits on top of the c-Si. We ignore the effect of the ITO thin film, which exhibits parasitic absorption, to simplify the simulations. The absorption spectra was calculated from $A(E) = 1 - R(E)$ where $R(E)$ is the energy dependent reflection. The ultimate efficiency is calculated from from

$$\eta = \frac{\int_{E_g}^{\infty} I(E)A(E)\frac{E_g}{E}dE}{\int_0^{\infty} I(E)dE} \tag{6.1}$$

where $E_g = 1.12$ eV is the band gap of c-Si and $I(E)$ is the solar irradiance under the global 37° tilt Air Mass 1.5 spectrum [95]. Figure 53 plots the simulated ultimate efficiency versus PS NS array diameter. The ultimate efficiency is near the maximum for NS diameter and largely independent of NS diameter above about 700 nm. So we used 800 nm diameter PS NSs on top of the ultrathin Si solar cell. Larger diameter NSs are difficult to coat uniformly on substrates and may also exhibit higher parasitic absorption from impurities.

The ultrathin c-Si film was fabricated from double-side polished p-type (100) Si wafers (100 mm diameter, 10 - 20 Ω-cm, 475 - 525 μm thickness). The wafer was immersed in 25% KOH solution at 90 °C for about 2.5 hours to obtain about 15 μm thick Si films [103]. The free standing ultrathin Si film was mounted onto a bulk Si wafer via heat release tape. To dope the substrate n+, phosphorus spin-on dopant (SOD) (P8545, Honeywell Accuspin) was spin coated onto the wafer at 4000 rpm for 1 min and then baked for 1 min at 150 °C. Then the Si film was released, flipped over and mounted on another bulk Si wafer. Boron SOD (B40, Honeywell Accuspin) was spin coated at 4000 rpm for 1 min and then baked for 1 min at 150 °C. The dopants were diffused into the ultrathin Si film by rapid thermal annealing at 900 °C for 15 min. After doping, the Si film was immersed in 7:1 BOE solution for 3 min to remove SOD residue on both sides of the film, and then washed with deionized water thoroughly. 200 nm of ITO was deposited on the n+ side of the Si film via radio frequency (RF) sputtering at 50 watts power and 16 mTorr pressure condition. Then 8 nm of Ti followed by 200 nm of Ag was evaporated on the back side of the Si film as back contact. For the PS monolayer fabrication, 4 wt% aqueous suspension (Life Technologies) of 800 nm diameter PS NSs was diluted with equal volume of anhydrous ethanol. A close-packed PS monolayer was fabricated on a water surface via self assembly method [104], transferred on top of the Si film solar cell, and then dried in air.

Figure 54 plots the current density versus voltage (J-V) curves of the solar cells measured under the illumination of an AM1.5 global solar simulator. The solar cell without the nanospheres (plain Si) has a short circuit current density J_{sc} of 16.2 mA/cm^2. After coating with PS NSs, the J_{sc} increased to 18.6 mA/cm^2. The short circuit current density increases by about 15%, which indicates an enhancement of incident light absorption in the Si film layer. Table 7 lists the J_{sc}, open circuit voltage (V_{oc}), fill factor (FF), and PCE of the solar cells consisting of plain c-Si and with PS NSs on top. Along with the increase in J_{sc}, the V_{oc} and FF both improve slightly as well. As a result, the PCE of Si solar cell with PS NSs coating increased from 4.9% for the plain Si film solar cell to 6.2%. This is an improvement of about 26.5%.

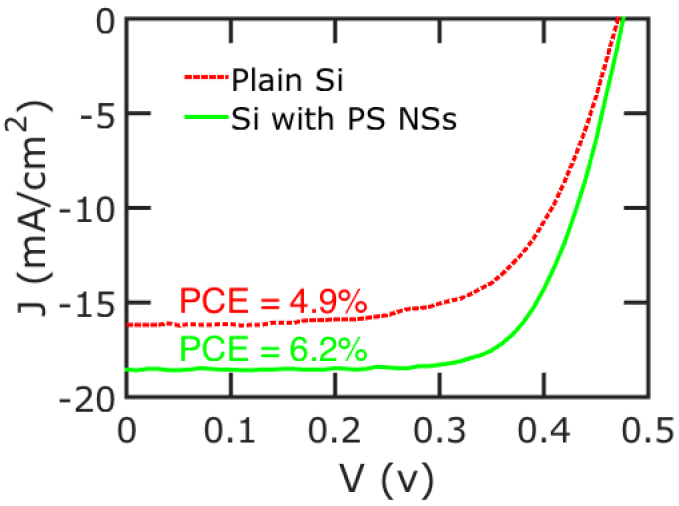

Figure 54: J-V characteristics measured on c-Si solar cells without and with PS NSs coating.

Table 7: Photovoltaic properties of the ultrathin c-Si solar cells without and with PS NSs.

	$\mathbf{J_{sc}}$ **(mA/cm^2)**	$\mathbf{V_{oc}}$ **(v)**	**FF (%)**	**PCE (%)**
Plain Si	16.2	0.47	64	4.9
With PS NSs	18.6	0.48	70	6.2

Based on our experiments, we found the best efficiency enhancements with nanospheres made of PS, which has an index of refraction of about 1.6 [105]. In our previous simulation paper, we found that higher index of refraction NSs exhibit better efficiency improvements [101]. Higher index of refraction NSs have an increased number of whispering gallery modes that can couple incident light to Fabry-Pérot-like resonances and higher order photonic waveguide modes in the Si thin film. However, TiO_2, which has an index of refraction of about 3 [78], also exhibits parasitic absorption in the ultraviolet [106]. Current synthesis methods for Si_3N_4 NSs, which have an index of refraction of about 2, result in very nonuniform

diameter NSs. Future improvements in the synthesis of high index of refraction nanospheres may enable further improvements in efficiency for NS coated solar cells.

Figure 55(a) plots the EQE for both the plain c-Si solar cell and c-Si solar cells with PS NSs on top. This EQE measurement is carried out under monochromatic illumination by a halogen lamp coupled to a monochromator. The ratio between the EQE of PS NS Si solar cells compared with plain Si solar cells is plotted as in Figure 55(b). There is an EQE enhancement in most of the spectrum measured. Furthermore, there are several distinct peaks for the PS NS coated solar cell EQE. Most notably, at the wavelengths of 470 nm and 1003 nm, the EQE enhancement is almost double that of the plain c-Si solar cell.

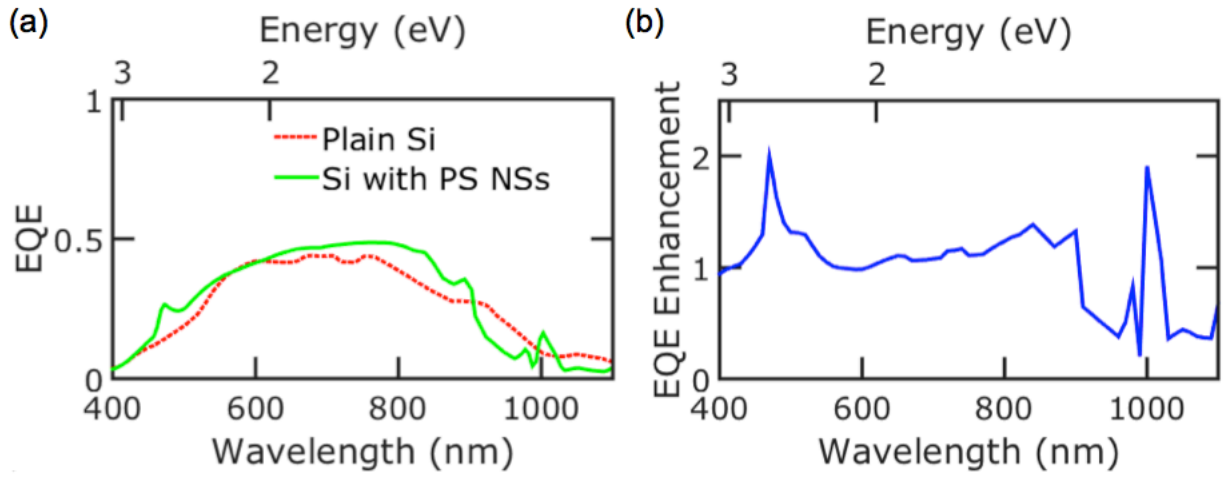

Figure 55: (a) EQE measured on flat silicon solar cells without and with PS NSs coating. (b) Ratio between EQE of plain Si and Si with PS NSs solar cells versus wavelength.

In order to better understand the results, we performed finite difference time domain (FDTD) simulations to investigate the absorption in c-Si layer. The simulated structure was like the experimental structure and consisted of 15 μm c-Si with a 200 nm layer of ITO on the front. The back contact was modeled as a perfect electric conductor boundary condition and appropriate symmetric and anti-symmetric boundary conditions are used to model the periodic nature of the NS array.

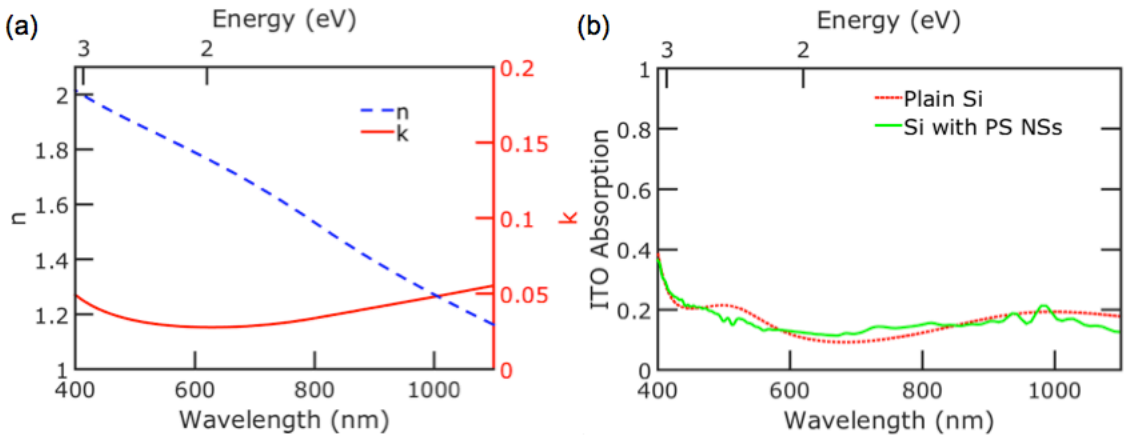

Figure 56: (a) Refractive index n and extinction coefficient k of ITO obtained from experiments that were subsequently used in simulations. (b) Parasitic absorption in the ITO film.

The refractive index n and extinction coefficient k of ITO used in simulations was acquired from the ellipsometry and displayed in Figure 56(a). An ITO film thickness of about 200 nm was sputtered and the optical constants were fitted by ellipsometry. The position dependent absorption per unit volume may be calculated from the divergence of the Poynting vector $\vec{P}$: $A(\mathbf{r}, E) = \frac{1}{2}\text{real}\{\vec{\nabla} \cdot \vec{P}\} = \frac{1}{2}\epsilon_i(E)\frac{E}{\hbar}|\mathbf{E}(\mathbf{r}, E)|^2$, where $\epsilon_i(E)$ is the imaginary part of the dielectric constant, $\hbar$ is the reduced Planck constant, and $\mathbf{E}(\mathbf{r}, E)$ is the energy and position-dependent electric field. The parasitic absorption in the ITO thin film was calculated by integrating the position dependent absorption per unit volume over the ITO and is plotted in Figure 56(b). The monolayer coating of PS NSs does not affect the amount of parasitic absorption.

The optical constants of PS [105] and the refractive index of c-Si [78] were both obtained from the literature. In the simulations, we obtained the absorption in the c-Si layers for both the plain c-Si and Si with PS NSs solar cells by integrating the position dependent absorption per unit volume over the Si volume. This omits the parasitic absorption that occurs in the ITO thin film, which is based on the ITO extinction coefficient. The addition of the PS NSs only changes the parasitic absorption in the ITO thin film negligibly. Figure 57 plots the absorption of the c-Si from the simulation. Similar to the our experimental EQE results, we

find that the absorption in the c-Si layer with PS NSs is higher than that of the plain Si over a broad wavelength range. Furthermore, there are several extra peaks in the absorption spectrum for the structure with PS array.

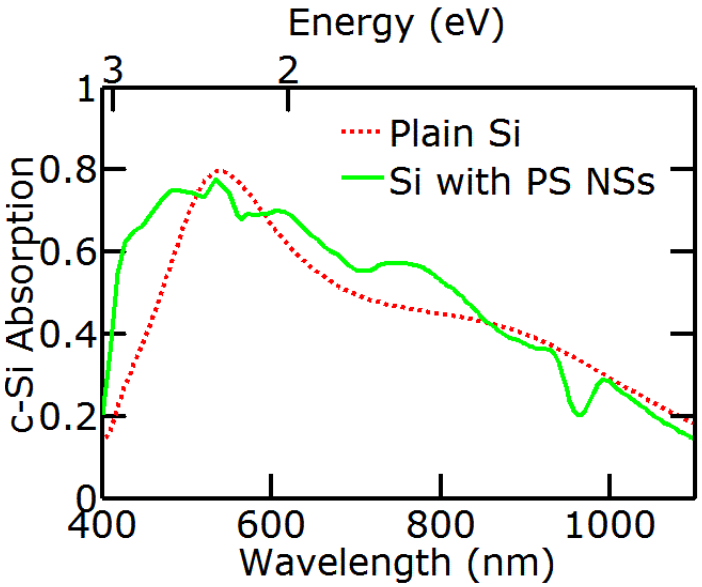

Figure 57: Simulated absorption spectra in c-Si thin film without and with PS nanospheres coating.

To understand the extra peaks in EQE and absorption for the structure with PS monolayer, we then investigated the electric field profile at these specific wavelengths for both structures. Figure 58 plots the electric field intensity $|\mathbf{E}|^2$ at the wavelengths (a) 481 and (b) 756 nm. The c-Si absorption of the plain Si solar cell is 0.57 and 0.46 at these wavelengths, respectively. In contrast, the c-Si absorption of the Si with PS NSs solar cell is 0.78 and 0.57 at these wavelengths, respectively. In Figure 58, part (i) and (ii) plot the electric field intensity for the plain Si solar cell, while part (iii) and (iv) plot the electric field intensity for the solar cell with PS NSs. Part (i) and (iii) plot the electric field intensity in the x-y plane at $z = -500$ nm. This is 500 nm below the top surface of the Si. Part (ii) and (iv) plot the electric field intensity in the x-z plane at $x = 0$. The edges of the nanospheres are shown with white solid lines and the edges of ITO are indicated by white dashed lines.

The ultrathin c-Si is underneath the ITO layer and only the top 1000 nm is shown. From part (iii), we can observe the modes of NSs couple to each other because the spheres are touching. These resonant modes exhibit high field intensity in the NSs and allow incident light to couple into the underlying Si across a broader range of wavelengths. The NSs also facilitates the lateral propagation of light due to its 2-dimensional structure.

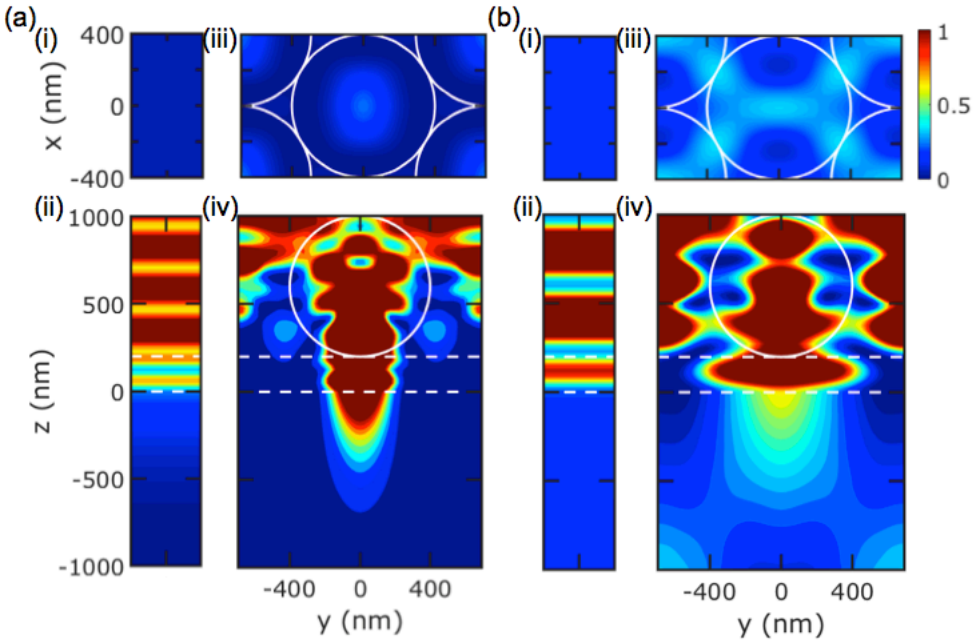

Figure 58: The electric field intensity $|\mathbf{E}|^2$ at $\lambda =$ (a) 481 and (b) 756 nm. At each wavelength, the electric field intensity for the (i, ii) plain Si and (iii, iv) Si with PS NS solar cell structures are plotted. Dashed lines show the boundary of the ITO and white lines show the boundaries of the PS NSs. The plain Si solar cell is plotted in (i) the x-y plane at $z = -500$ nm and (ii) the x-z plane cross section view. The Si solar cell with NSs is plotted in (iii) the x-y plane at $z = -500$ nm and (iv) the x-z plane cross section view at $x = 0$.

6.2.1 Conclusions

In conclusion, we demonstrate that with a monolayer of 800 nm diameter PS NSs, the light absorption can be enhanced over a broad wavelength range for 15 μm thickness ultrathin c-Si solar cells both in experiments and simulations. This light harvesting scheme results in a 26.5% PCE enhancement and an EQE enhancement of almost 2 times at several wavelengths. The NS array couples incident light into the underlying Si and facilitates wave propagation in lateral direction. The fabrication technique for this reported light harvesting structure is facile and easy to integrate with other light trapping and anti-reflection techniques. This light harvesting mechanism should be a promising path toward high efficiency and low cost solar cells and may be beneficial to other optoelectronic devices.

6.3 FLEXIBLE ULTRATHIN SILICON SOLAR CELLS WITH INTEGRATED METAL NANOMESH AND NANOSPHERES

In our previous work, [102] we showed that the PCE of 15 μm thick ultrathin c-Si solar cells can be improved by 26.5% by introducing a monolayer of 800 nm polystyrene (PS) NSs with indium tin oxide (ITO) as front contact. In this work, we use a metal nanomesh as front contact which is fabricated by microsphere lithography. [107] The metal nanomesh demonstrates lower sheet resistance than ITO while maintaining a comparable optical transmission. In addition, this type of metal nanomesh has a tunable haze factor which will be discussed in detail later. As a result, the PCE of c-Si solar cell with metal nanomesh is improved by 53% compared to that of c-Si solar cell with ITO. More importantly, the metal nanomesh has superior flexibility to ITO, which significantly enhances the flexibility and durability of the c-Si thin film solar cells. With the introduction of a dielectric nanosphere monolayer array on top of the metal nanomesh, the scattering of light is further enhanced, and as a result, the PCE of the c-Si solar cell can be increased by an additional 10.6%.

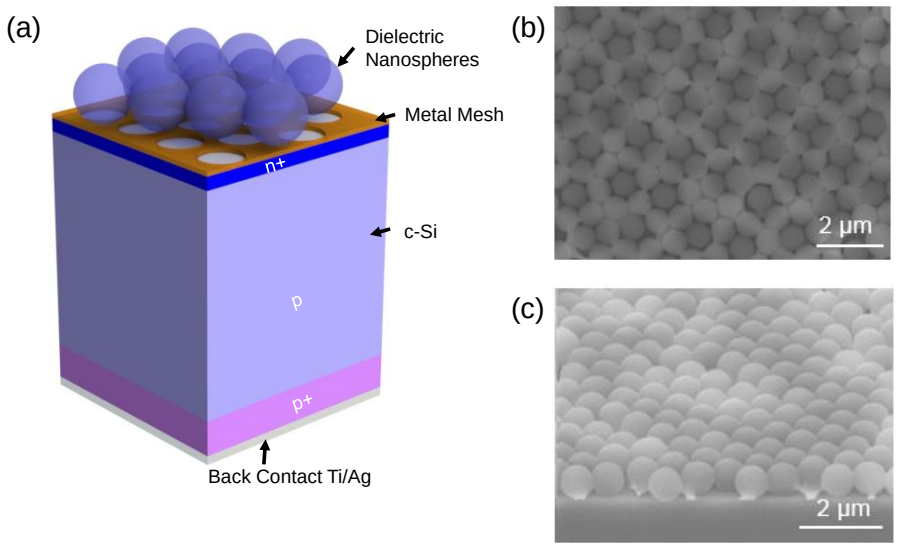

Figure 59: (a) Schematic of the integrated solar cell with the metal nanomesh and dielectric NSs. A hexagonal close packed-monolayer of 800 nm diameter PS NSs lies on top of this solar cell. (b) Top view SEM image of the PS NSs on c-Si solar cell. (c) Cross section view of the solar cell with PS NSs monolayer on top.

Figure 59(a) shows a schematic of our ultrathin film c-Si solar cell structure which consists of a c-Si film between a metal nanomesh front transparent electrode and a Ti/Ag back contact. The c-Si layer is doped n+, p, and p+ from top to bottom. A close packed hexagonal lattice monolayer of 800 nm diameter PS NSs is coated on top of the c-Si thin film solar cell. Figure 59(b) shows a scanning electron microscope (SEM) image of the the top view of the PS NS hexagonal array. The NS layer is close packed and uniform over the solar cell. Figure 59(c) shows a cross section SEM image of the solar cell. The c-Si film has thickness 14.7 μm slightly thinner than that in the previous work. [102] We used 800 nm diameter PS NSs on top of the ultrathin c-Si solar cell, because our simulation results [102] indicate that the ultimate efficiency is relatively insensitive to PS NS diameters higher than 800 nm. Larger diameter NSs are difficult to coat uniformly on substrates and may also exhibit higher parasitic absorption from impurities.

The ultrathin c-Si film was fabricated from double-side polished p-type (100) c-Si wafers (100 mm diameter, 10 - 20 Ω-cm, 475 - 525 μm thickness). The wafer was immersed in 25%

KOH solution at 90 °C for about 2.5 hours to obtain about 14.7 μm thick c-Si films. [108] The top side of the free standing ultrathin c-Si film was doped to n+ via phosphorus spin-on dopant (SOD) (P8545, Honeywell Accuspin) and the back side of the c-Si film was doped to p+ via boron SOD (B40, Honeywell Accuspin). The dopants were diffused into the ultrathin c-Si film by rapid thermal annealing at 900 °C for 15 min. After doping, the dopant reside was removed by buffered oxide enchant (BOE) solution, and then the sample was washed with deionized water thoroughly.

Figure 60(a) plots the current density versus voltage (J-V) curves of the solar cells measured under the illumination of an AM1.5 global solar simulator. The short circuit current density J_{sc} of the solar cell with ITO as front contact but without nanospheres (Si/ITO) is 16.2 mA/cm^2. The J_{sc} increased to 18.6 mA/cm^2 with the PS NSs coating (Si/ITO/PS). After the front contact was changed from ITO to metal nanomesh, J_{sc} increased to 21.2 mA/cm^2 and 23.4 mA/cm^2 for the solar cells without (Si/Nanomesh) and with PS NSs (Si/Nanomesh/PS) coating. Table 8 lists J_{sc}, open circuit voltage (V_{oc}), fill factor (FF), and PCE of the four different structures solar cells. As a result of the lower sheet resistance of the metal nanomesh, the fill factor of solar cell with metal nanomesh as front contact improved to 75% compared to 70% with ITO as front contact. For the plain Si solar cells, the power conversion efficiency improved from 4.9% with ITO to 7.5% with metal nanomesh, and it is improved by 53%. Figure 60(b) shows the external quantum efficiency (EQE) for solar cells with both types front contacts with and without PS NS on top. This EQE measurement is carried out under monochromatic illumination by a halogen lamp coupled to a monochromator. We can see, with metal nanomesh with contact, there is an EQE enhancement, especially in the short wavelength range.

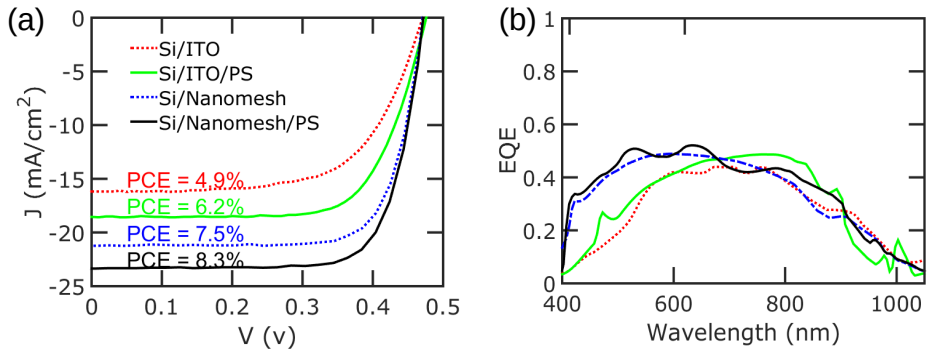

Figure 60: (a) J-V characteristics and (b) EQE measured on c-Si solar cells with different front contacts without and with PS NSs coating.

Table 8: Photovoltaic properties of the ultrathin c-Si solar cells without and with PS NSs with different types of contacts.

	$\mathbf{J_{sc}}$ $\mathbf{(mA/cm^2)}$	$\mathbf{V_{oc}}$ **(v)**	**FF (%)**	**PCE (%)**
Plain Si	16.2	0.47	64	4.9
With PS NSs	18.6	0.48	70	6.2
Plain Si with nanomesh	21.2	0.47	75	7.5
Nanomesh with PS NSs	23.4	0.47	75	8.3

The metal nanomesh is about 35 nm thick with a pitch of 1300 nm and hole diameter 1200 nm which is fabricated by the microsphere lithography method. [107] The metal nanomesh has a sheet resistance $R_s \approx 10\ \Omega$/sq compared to 30 - 40 Ω/sq for ITO. In order to understand the results, we measured both of the diffusive and specular transmission of three different structures using a spectrophotometer with and without integrating sphere, respectively. As shown in Figure 61(a), from which we can see the transmission of the metal nanomesh is just slightly below that of ITO. Table 9 lists the solar transmission, T_{sol} for the different types of front contacts, calculated from

$$T_{sol} = \frac{\int b(\lambda)T(\lambda)d\lambda}{\int b(\lambda)d\lambda}, \tag{6.2}$$

where λ is the free space wavelength, $b(\lambda)$ is the photo flux density, and $T(\lambda)$ is the optical transmission at wavelength λ, and the solar absorption, A_{solar} and solar haze factor, H_{sol} as discussed later are also caluclated with the same way. The T_{sol} for ITO is 77.1% while it is 70.6% for the metal nanomesh, which is 8.43% lower. Haze factor, in addition to transparency and sheet resistance, is another crucial factor for flat panel displays and solar cells. The haze factor is determined by the diffusive transmission (T_{diff}) and specular transmission (T_{spec}),

$$H = \frac{T_{diff} - T_{spec}}{T_{diff}} \tag{6.3}$$

Thus, the haze factor can be tuned by the diffusive and specular transmissions which can be tuned by controlling the geometries of the metal nanomeshes. Higher haze factor means higher diffusive transmission percentage, so light have longer optical path. Thus, a low haze factor is required for displays to avoid blurry imaging, while a high haze factor is desirable for solar cells to increase the optical path length in the absorber. The metal nanomesh used as front contact in this work is designed to have higher haze factor up to 0.4 over most of the spectrum as shown in Figure 61(d) while the haze factor of ITO is very small, nearly negligible. As shown in table 9, H_{sol} for metal nanomesh is 38.5%, 5.75 times higher than that of ITO. So combining the comparable transmission and much higher haze factor compared to ITO, the J_{sc} of solar cell with metal nanomesh is 31% higher than that of solar cell with ITO. By introducing the PS NS on top of metal nanomesh, the T_{sol} is dropped to around 63%, however, the H_{sol} is increased to 70%, thus, the J_{sc} could be further improved by 10.6% with PS NS on top. We also measured the reflection of the three different front structures as shown in Figure 61(b) and the absorption in Figure 61(c) is calculated from $A(\lambda) = 1 - R(\lambda) - T(\lambda)$ where $R(\lambda)$ is the wavelength dependent reflection and $T(\lambda)$ is the wavelength dependent transmission. A_{sol} is listed in table 9, and we can see that the absorption of metal nanomesh itself is very small, almost negligible, while when PS is introduced, the solar absorption increased to about 13.6%. As a result, the transmission with PS on top of metal nanomesh is decreased. However, due to the high haze factor resulting from strong scattering effect, the PS monolayer on top of metal nanomesh can still improve the PCE by 10.6% despite stronger parasitic absorption.

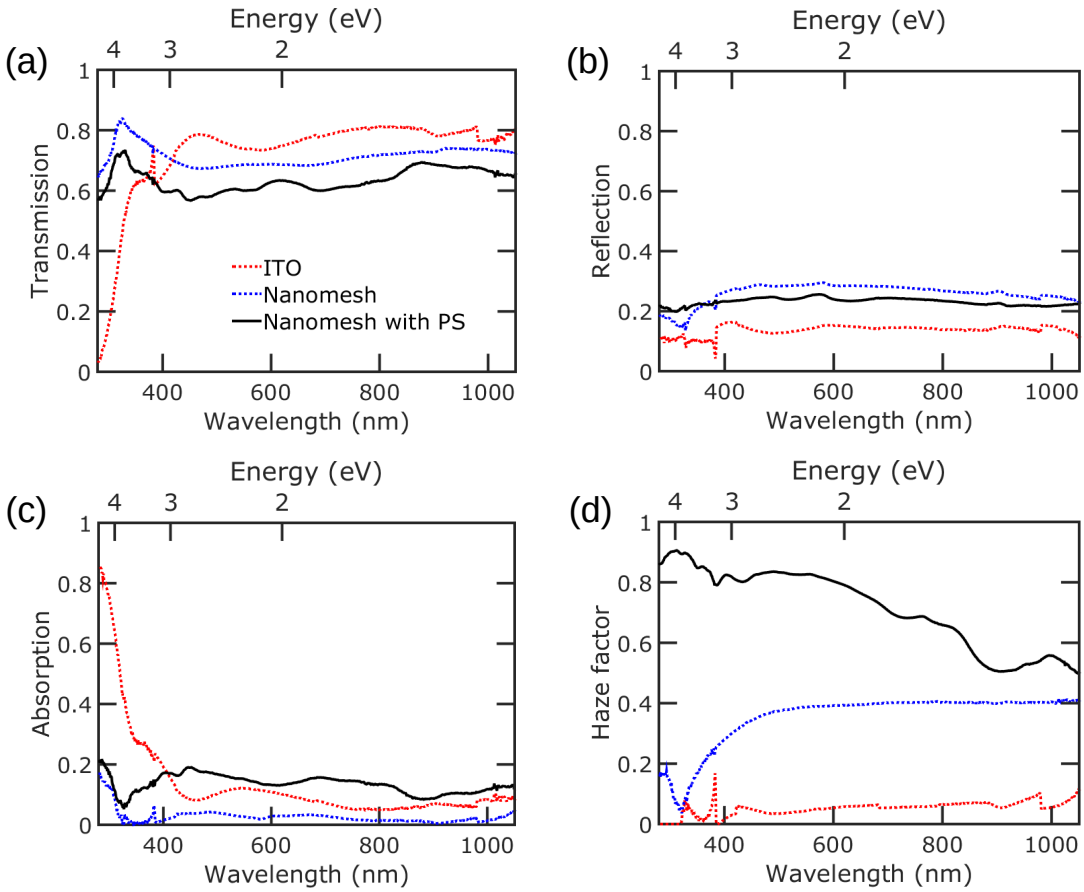

Figure 61: Measured (a) transmissions (b) reflection of three different transparent conductors, ITO, metal nanomesh, and metal nanomesh with PS on top. Calculated (c) absorption and (d) haze factor of three different transparent conductors.

Table 9: The total solar transmission, T_{sol} (%), solar absorption, A_{sol} (%), and solar haze factor, H_{sol} (%) of three different types of contacts.

	$\mathbf{T_{sol}}$ (%)	$\mathbf{A_{sol}}$ (%)	$\mathbf{H_{sol}}$ (%)
ITO	77.1	8.9	5.7
Nanomesh	70.6	2.3	38.5
Nanomesh with PS	63.0	13.6	70.0

To show the flexibility, we performed the bending a 10 μm thick c-Si solar cell with the Ag metal nanomesh with a geometry of t = 35 nm, a = 1300 nm and w = 10nm around a steel rod with 1 cm diameter. As shown in Figure 62, the efficiency almost does not change after 1200 cycles of bending while the resistivity of ITO will increase by up to 30 times after 25 cycles of bending. [109]

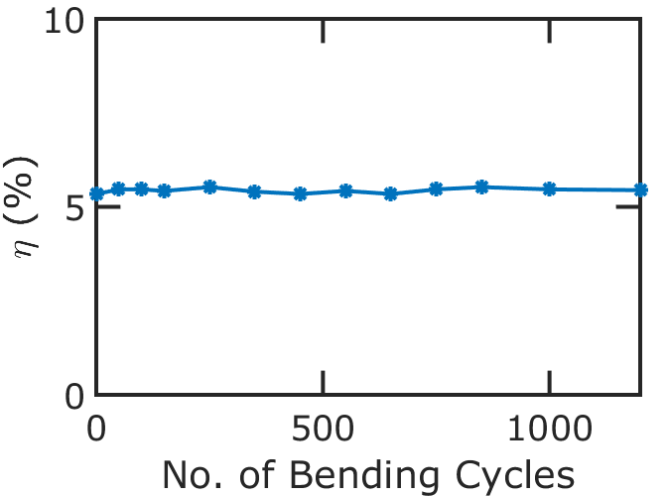

Figure 62: Power conversion efficiency against the number of bending cycles on a 10 μm c-Si thin film solar cell with metal nanomesh with a geometry of t = 35 nm, a = 1300 nm and w = 100 nm.

6.3.1 Conclusions

In conclusion, the metal nanomesh front contacts not only enhance the short circuit current of the solar cells due to the high haze factor but also increase the fill factor because of the low sheet resistance compared to ITO. As a result, the power conversion efficiency is improved by 53% compared to bare c-Si solar cell with ITO. Furthermore, we show that dielectric nanosphere arrays can further enhance the efficiency by 10.6% of ultrathin film crystalline silicon by scattering incident light into the underlying silicon layer. The 14.7 μm thick silicon solar cells exhibit an 8.3% power conversion efficiency and are robust under

repeated bending. So this strategy not only enhances the PCE of the solar cells which helps to reduce the material cost with higher energy but also opens up new applications due to the significantly flexibility property improvement.

7.0 CONCLUSIONS AND PROSPECTS

Nanostructures open up exciting opportunities for optoelectronic devices performance enhancement due to the light manipulation ability. In my work, I focused on two schemes of light management at the nanoscale: active layer texture and high refractive index nanospheres coupling. We showed that tapered nanocone structures combine the abilities of antireflection and light trapping across a broad band wavelength and a wide angle range numerically. We successfully fabricated wafer scale nanocone structures with different geometries and demonstrated the performance on black silicon solar cells with a metal network transparent electrode. Dielectric nanospheres have emerged as a promising candidate for enhancing absorption in thin film photovoltaics. We numerically and experimentally demonstrated that nanospheres can enhance the absorption in thin silicon solar cells by coupling incident light into waveguide modes without introducing new interfaces or surfaces. With metal nanomesh instead of indium tin oxide as front contact, this kind of device showed superior flexibility. So this strategy not only enhances the PCE of the solar cells which helps to reduce the material cost with higher energy but also opens up new applications due to the significantly flexibility property improvement.

So, there are new opportunities for low cost and high efficiency solar cells based these two schemes. However, there are still challenges. The fabrication of large scale ultrathin silicon with facile methods still needs more effort and research. And there is still room for the solar cells efficiency improvement.

BIBLIOGRAPHY

[1] International Energy Agency. *INTERNATIONAL ENERGY OUTLOOK 2013*. 2013.

[2] International Energy Agency. *Redrawing the energy climate map world energy outlook special report*. 2013.

[3] Worldwatch Institute. *State of the World 2009*. 2009.

[4] J. Chaves. *Introduction to Nonimaging Optics*. CRC Press, 2008.

[5] John Perlin. *From Space to Earth: The Story of Solar Electricity*. Harvard University Press, 2002.

[6] Matthias Loster. Total primary power density supply from sunlight. *Departemt of Physics. University of California*, 2006.

[7] Alexandre-Edmond Becquerel. Recherches sur les effets de la radiation chimique de la lumière solaire, au moyen des courants électriques. *CR Acad. Sci*, 9:145–149, 1839.

[8] L. O. Grondahl. The copper-cuprous-oxide rectifier and photoelectric cell. *Reviews of Modern Physics*, 5(2):141–168, April 1933. doi: 10.1103/RevModPhys.5.141. URL http://link.aps.org/doi/10.1103/RevModPhys.5.141.

[9] L Bergmann. Uber eine neue selen-sperrschicht-photozelle. *Physik. Zeitschr*, 32:286–288, 1931.

[10] Foster C Nix and Arnold W Treptow. A thallous sulphide photo-emf cell. *JOSA*, 29 (11):457–462, 1939.

[11] David C Brock. Useless no more: Gordon k. teal, germanium, and single-crystal transistors. *Chemical Heritage Newsmagazine (Chemical Heritage Foundation)*, 24(1), 2007.

[12] J Czochralski. Ein neues verfahren zur messung der kristallisationsgeschwindigkeit der metalle. *Zeitschrift fur Physikalische Chemie*, 92:219, 1917.

[13] D. M. Chapin, C. S. Fuller, and G. L. Pearson. A New Silicon p-n Junction Photocell for Converting Solar Radiation into Electrical Power. *Journal of Applied Physics*, 25: 676–677, May 1954. doi: 10.1063/1.1721711.

[14] D. C. Reynolds, G. Leies, L. L. Antes, and R. E. Marburger. Photovoltaic effect in cadmium sulfide. *Phys. Rev.*, 96:533–534, Oct 1954. doi: 10.1103/PhysRev.96.533. URL http://link.aps.org/doi/10.1103/PhysRev.96.533.

[15] D. E. Carlson and C. R. Wronski. Amorphous silicon solar cell. *Applied Physics Letters*, 28(11):671–673, 1976. doi: http://dx.doi.org/10.1063/1.88617. URL http://scitation.aip.org/content/aip/journal/apl/28/11/10.1063/1.88617.

[16] R.B. Hall, R.W. Birkmire, J.E. Phillips, and J.D. Meakin. Thin-film polycrystalline (cdzn)s/cu2s solar cells of 10efficiency. In W. Palz, editor, *Photovoltaic Solar Energy Conference*, pages 1094–1096. Springer Netherlands, 1981. ISBN 978-94-009-8425-7. doi: 10.1007/978-94-009-8423-3_184. URL http://dx.doi.org/10.1007/978-94-009-8423-3_184.

[17] AW Blakers and MA Green. 20 *Applied physics letters*, 48(3):215–217, 1986.

[18] K. Yamamoto. Thin film Si solar cell fabricated at low temperature. *Journal of Non Crystalline Solids*, 266:1082–1087, May 2000. doi: 10.1016/S0022-3093(99)00907-2.

[19] Brian Oregan and M Grfitzeli. A low-cost, high-efficiency solar cell based on dye-sensitized. *nature*, 353:737–740, 1991.

[20] Gavin Conibeer. Third-generation photovoltaics. *Materials Today*, 10(11):42 – 50, 2007. ISSN 1369-7021. doi: http://dx.doi.org/10.1016/S1369-7021(07)70278-X. URL http://www.sciencedirect.com/science/article/pii/S136970210770278X.

[21] Kenji Yamamoto, Masashi Yoshimi, Y Tawada, Y Okamoto, A Nakajima, and S Igari. Thin-film poly-si solar cells on glass substrate fabricated at low temperature. *Applied Physics A*, 69(2):179–185, 1999.

[22] Lu Hu and Gang Chen. Analysis of optical absorption in silicon nanowire arrays for photovoltaic applications. *Nano Letters*, 7(11):3249–3252, November 2007. doi: 10.1021/nl071018b. URL http://dx.doi.org/10.1021/nl071018b.

[23] Sang Eon Han and Gang Chen. Optical absorption enhancement in silicon nanohole arrays for solar photovoltaics. *Nano Letters*, 10(3):1012–1015, March 2010. doi: 10.1021/nl904187m. URL http://dx.doi.org/10.1021/nl904187m.

[24] Sang Eon Han and Gang Chen. Toward the lambertian limit of light trapping in thin nanostructured silicon solar cells. *Nano Letters*, 10(11):4692–4696, November 2010. doi: 10.1021/nl1029804. URL http://dx.doi.org/10.1021/nl1029804.

[25] Junshuai Li, HongYu Yu, She Mein Wong, Gang Zhang, Xiaowei Sun, Patrick Guo-Qiang Lo, and Dim-Lee Kwong. Si nanopillar array optimization on Si thin films

for solar energy harvesting. *Applied Physics Letters*, 95(3):033102, 2009. ISSN 00036951. doi: 10.1063/1.3186046. URL http://link.aip.org/link/APPLAB/v95/i3/p033102/s1&Agg=doi.

[26] Junshuai Li, HongYu Yu, She Mein Wong, Xiaocheng Li, Gang Zhang, Patrick Guo-Qiang Lo, and Dim-Lee Kwong. Design guidelines of periodic Si nanowire arrays for solar cell application. *Applied Physics Letters*, 95(24):243113, 2009. ISSN 00036951. doi: 10.1063/1.3275798. URL http://link.aip.org/link/APPLAB/v95/i24/p243113/s1&Agg=doi.

[27] Shrestha Basu Mallick, Mukul Agrawal, and Peter Peumans. Optimal light trapping in ultra-thin photonic crystal crystalline silicon solar cells. *Optics Express*, 18(6):5691–5706, March 2010. doi: 10.1364/OE.18.005691. URL http://www.opticsexpress.org/abstract.cfm?URI=oe-18-6-5691.

[28] Yeonsang Park, Emmanuel Drouard, Ounsi El Daif, Xavier Letartre, Pierre Viktorovitch, Alain Fave, Anne Kaminski, Mustapha Lemiti, and Christian Seassal. Absorption enhancement using photonic crystals for silicon thin film solar cells. *Optics Express*, 17(16):14312–14321, 2009. doi: 10.1364/OE.17.014312. URL http://www.opticsexpress.org/abstract.cfm?URI=oe-17-16-14312.

[29] Xing Sheng, Steven G. Johnson, Jurgen Michel, and Lionel C. Kimerling. Optimization-based design of surface textures for thin-film Si solar cells. *Optics Express*, 19 (S4):A841–A850, July 2011. doi: 10.1364/OE.19.00A841. URL http://www.opticsexpress.org/abstract.cfm?URI=oe-19-104-A841.

[30] Vivian E. Ferry, Albert Polman, and Harry A. Atwater. Modeling light trapping in nanostructured solar cells. *ACS Nano*, 5(12):10055–10064, 2011. ISSN 1936-0851. doi: 10.1021/nn203906t. URL http://dx.doi.org/10.1021/nn203906t.

[31] A. Taflove. Application of the finite-difference time-domain method to sinusoidal steady-state electromagnetic-penetration problems. *Electromagnetic Compatibility, IEEE Transactions on*, EMC-22(3):191–202, 1980. ISSN 0018-9375. doi: 10.1109/TEMC.1980.303879. URL http://ieeexplore.ieee.org/search/srchabstract.jsp?tp=&arnumber=4091372.

[32] Kane Yee. Numerical solution of initial boundary value problems involving maxwell's equations in isotropic media. *Antennas and Propagation, IEEE Transactions on*, 14 (3):302–307, 1966. ISSN 0018-926X. doi: 10.1109/TAP.1966.1138693. URL http://ieeexplore.ieee.org/xpls/abs_all.jsp?arnumber=1138693&tag=1.

[33] Lumerical Solutions Inc. URL http://www.lumerical.com/tcad-products/fdtd/.

[34] Jean-Pierre Berenger. A perfectly matched layer for the absorption of electromagnetic waves. *Journal of Computational Physics*, 114(2):185–200, October 1994. ISSN 0021-9991. doi: 06/jcph.1994.1159. URL http://www.sciencedirect.com/science/article/pii/S0021999184711594.

[35] William Shockley and Hans J. Queisser. Detailed balance limit of efficiency of p-n junction solar cells. *Journal of Applied Physics*, 32(3):510, 1961. ISSN 00218979. doi: 10.1063/1.1736034. URL http://link.aip.org/link/JAPIAU/v32/i3/p510/s1&Agg=doi.

[36] E. Yablonovitch and G.D. Cody. Intensity enhancement in textured optical sheets for solar cells. *Electron Devices, IEEE Transactions on*, 29(2):300–305, 1982. ISSN 0018-9383. URL http://ieeexplore.ieee.org/xpls/abs_all.jsp?arnumber=1482197&tag=1.

[37] Ping Sheng. Optical absorption of thin film on a lambertian reflector substrate. *IEEE Transactions on Electron Devices*, 31(5):634– 636, May 1984. ISSN 0018-9383. doi: 10.1109/T-ED.1984.21582. URL http://dx.doi.org/10.1109/T-ED.1984.21582.

[38] Jongseung Yoon, Alfred J. Baca, Sang-Il Park, Paulius Elvikis, Joseph B. Geddes, Lanfang Li, Rak Hwan Kim, Jianliang Xiao, Shuodao Wang, Tae-Ho Kim, Michael J. Motala, Bok Yeop Ahn, Eric B. Duoss, Jennifer A. Lewis, Ralph G. Nuzzo, Placid M. Ferreira, Yonggang Huang, Angus Rockett, and John A. Rogers. Ultrathin silicon solar microcells for semitransparent, mechanically flexible and microconcentrator module designs. *Nat Mater*, 7(11):907–915, November 2008. ISSN 1476-1122.

[39] V. Sivakov, G. Andr, A. Gawlik, A. Berger, J. Plentz, F. Falk, and S. H. Christiansen. Silicon nanowire-based solar cells on glass: Synthesis, optical properties, and cell parameters. *Nano Lett.*, 9(4):1549–1554, 2009. PMID: 19281253.

[40] L. Tsakalakos, J. Balch, J. Fronheiser, B. A. Korevaar, O. Sulima, and J. Rand. Silicon nanowire solar cells. *Appl. Phys. Lett.*, 91(23):233117, 2007. ISSN 00036951.

[41] T. H. Stelzner, M Pietsch, G Andrä, F Falk, E Ose, and S Christiansen. Silicon nanowire-based solar cells. *Nanotechnology*, 19(29):295203, 2008. ISSN 0957-4484.

[42] Kuiqing Peng, Ying Xu, Yin Wu, Yunjie Yan, Shuit-Tong Lee, and Jing Zhu. Aligned single-crystalline Si nanowire arrays for photovoltaic applications. *Small*, 1(11):1062–1067, 2005.

[43] Erik C. Garnett and Peidong Yang. Silicon nanowire radial p-n junction solar cells. *J.Am. Chem. Soc.*, 130(29):9224–9225, July 2008.

[44] Erik Garnett and Peidong Yang. Light trapping in silicon nanowire solar cells. *Nano Lett.*, 10(3):1082–1087, March 2010.

[45] Oki Gunawan and Supratik Guha. Characteristics of vapor-liquid-solid grown silicon nanowire solar cells. *Sol. Energy Mater. Sol. Cells*, 93(8):1388–1393, August 2009. ISSN 0927-0248.

[46] Michael D. Kelzenberg, Shannon W. Boettcher, Jan A. Petykiewicz, Daniel B. Turner-Evans, Morgan C. Putnam, Emily L. Warren, Joshua M. Spurgeon, Ryan M. Briggs,

Nathan S. Lewis, and Harry A. Atwater. Enhanced absorption and carrier collection in Si wire arrays for photovoltaic applications. *Nat. Mater.*, 9(3):239–244, March 2010. ISSN 1476-1122.

[47] Katherine E. Plass, Michael A. Filler, Joshua M. Spurgeon, Brendan M. Kayes, Stephen Maldonado, Bruce S. Brunschwig, Harry A. Atwater, and Nathan S. Lewis. Flexible polymer-embedded Si wire arrays. *Adv. Mater.*, 21(3):325–328, 2009. ISSN 09359648.

[48] Linyou Cao, Pengyu Fan, Alok P. Vasudev, Justin S. White, Zongfu Yu, Wenshan Cai, Jon A. Schuller, Shanhui Fan, and Mark L. Brongersma. Semiconductor nanowire optical antenna solar absorbers. *Nano Letters*, 10(2):439–445, February 2010. doi: 10.1021/nl9036627. URL http://dx.doi.org/10.1021/nl9036627.

[49] Michael D. Kelzenberg, Daniel B. Turner-Evans, Brendan M. Kayes, Michael A. Filler, Morgan C. Putnam, Nathan S. Lewis, and Harry A. Atwater. Photovoltaic measurements in Single-Nanowire silicon solar cells. *Nano Letters*, 8(2):710–714, February 2008. doi: 10.1021/nl072622p. URL http://dx.doi.org/10.1021/nl072622p.

[50] Bozhi Tian, Xiaolin Zheng, Thomas J. Kempa, Ying Fang, Nanfang Yu, Guihua Yu, Jinlin Huang, and Charles M. Lieber. Coaxial silicon nanowires as solar cells and nanoelectronic power sources. *Nature*, 449(7164):885–889, October 2007. ISSN 0028-0836. doi: 10.1038/nature06181. URL http://dx.doi.org/10.1038/nature06181.

[51] Bozhi Tian, Thomas J. Kempa, and Charles M. Lieber. Single nanowire photovoltaics. *Chemical Society Reviews*, 38(1):16–24, 2009. URL http://dx.doi.org/10.1039/b718703n.

[52] Jia Zhu, Zongfu Yu, George F. Burkhard, Ching-Mei Hsu, Stephen T. Connor, Yueqin Xu, Qi Wang, Michael McGehee, Shanhui Fan, and Yi Cui. Optical absorption enhancement in amorphous silicon nanowire and nanocone arrays. *Nano Letters*, 9(1):279–282, January 2009. doi: 10.1021/nl802886y. URL http://dx.doi.org/10.1021/nl802886y.

[53] Ching-Mei Hsu, Stephen T. Connor, Mary X. Tang, and Yi Cui. Wafer-scale silicon nanopillars and nanocones by Langmuir–Blodgett assembly and etching. *Appl. Phys. Lett.*, 93(13):133109, 2008. ISSN 00036951.

[54] Kui-Qing Peng, Xin Wang, Li Li, Xiao-Ling Wu, and Shuit-Tong Lee. High-Performance silicon nanohole solar cells. *J.Am. Chem. Soc.*, 132(20):6872–6873, May 2010.

[55] Ounsi El Daif, Emmanuel Drouard, Guillaume Gomard, Anne Kaminski, Alain Fave, Mustapha Lemiti, Sungmo Ahn, Sihan Kim, Pere Roca i Cabarrocas, Heonsu Jeon, and Christian Seassal. Absorbing one-dimensional planar photonic crystal for amorphous silicon solar cell. *Opt. Express*, 18(S3):A293–A299, 2010.

[56] L. Zeng, P. Bermel, Y. Yi, B. A Alamariu, K. A Broderick, J. Liu, C. Hong, X. Duan, J. Joannopoulos, and L. C Kimerling. Demonstration of enhanced absorption in thin film Si solar cells with textured photonic crystal back reflector. *Applied Physics Letters*, 93(22):221105–221105–3, December 2008. ISSN 00036951. doi: doi:10.1063/1.3039787. URL http://apl.aip.org/resource/1/applab/v93/i22/p221105_s1.

[57] R. Biswas, J. Bhattacharya, B. Lewis, N. Chakravarty, and V. Dalal. Enhanced nanocrystalline silicon solar cell with a photonic crystal back-reflector. *Solar Energy Materials and Solar Cells*, 94(12):2337–2342, December 2010. ISSN 0927-0248. doi: 10.1016/j.solmat.2010.08.007. URL http://www.sciencedirect.com/science/article/pii/S0927024810004642.

[58] Benjamin Curtin, Rana Biswas, and Vikram Dalal. Photonic crystal based back reflectors for light management and enhanced absorption in amorphous silicon solar cells. *Applied Physics Letters*, 95(23):231102–231102–3, December 2009. ISSN 00036951. doi: doi:10.1063/1.3269593. URL http://apl.aip.org/resource/1/applab/v95/i23/p231102_s1.

[59] Harry A. Atwater and Albert Polman. Plasmonics for improved photovoltaic devices. *Nat Mater*, 9(3):205–213, March 2010. ISSN 1476-1122. doi: 10.1038/nmat2629. URL http://dx.doi.org/10.1038/nmat2629.

[60] Dayu Zhou and Rana Biswas. Photonic crystal enhanced light-trapping in thin film solar cells. *Journal of Applied Physics*, 103(9):093102, 2008. ISSN 00218979. doi: 10.1063/1.2908212. URL http://link.aip.org/link/JAPIAU/v103/i9/p093102/s1&Agg=doi.

[61] Simone Zanotto, Marco Liscidini, and Lucio Claudio Andreani. Light trapping regimes in thin-film silicon solar cells with a photonic pattern. *Optics Express*, 18(5):4260–4274, March 2010. doi: 10.1364/OE.18.004260. URL http://www.opticsexpress.org/abstract.cfm?URI=oe-18-5-4260.

[62] Yun-Chih Lee, Chian-Fu Huang, Jenq-Yang Chang, and Mount-Learn Wu. Enhanced light trapping based on guided mode resonance effect for thin-film silicon solar cells with two filling-factor gratings. *Optics Express*, 16(11):7969–7975, May 2008. doi: 10.1364/OE.16.007969. URL http://www.opticsexpress.org/abstract.cfm?URI=oe-16-11-7969.

[63] Alongkarn Chutinan, Nazir P. Kherani, and Stefan Zukotynski. High-efficiency photonic crystal solar cell architecture. *Optics Express*, 17(11):8871–8878, May 2009. doi: 10.1364/OE.17.008871. URL http://www.opticsexpress.org/abstract.cfm?URI=oe-17-11-8871.

[64] L. Zeng, Y. Yi, C. Hong, J. Liu, N. Feng, X. Duan, L. C. Kimerling, and B. A. Alamariu. Efficiency enhancement in Si solar cells by textured photonic crystal back reflector. *Applied Physics Letters*, 89(11):111111, 2006. ISSN 00036951. doi: 10.1063/1.2349845. URL http://link.aip.org/link/APPLAB/v89/i11/p111111/s1&Agg=doi.

[65] Ning-Ning Feng, J. Michel, Lirong Zeng, Jifeng Liu, Ching-Yin Hong, L.C. Kimerling, and Xiaoman Duan. Design of highly efficient light-trapping structures for thin-film crystalline silicon solar cells. *Electron Devices, IEEE Transactions on*, 54(8):1926–1933, 2007. ISSN 0018-9383. doi: 10.1109/TED.2007.900976. URL http://ieeexplore.ieee.org/xpls/abs_all.jsp?arnumber=4277956.

[66] Peter Bermel, Chiyan Luo, Lirong Zeng, Lionel C. Kimerling, and John D. Joannopoulos. Improving thin-film crystalline silicon solar cell efficiencies with photonic crystals. *Optics Express*, 15(25):16986–17000, December 2007. doi: 10.1364/OE.15.016986. URL http://www.opticsexpress.org/abstract.cfm?URI=oe-15-25-16986.

[67] Paul G. O'Brien, Nazir P. Kherani, Alongkarn Chutinan, Geoffrey A. Ozin, Sajeev John, and Stefan Zukotynski. Silicon photovoltaics using conducting photonic crystal Back-Reflectors. *Advanced Materials*, 20(8):1577–1582, 2008. ISSN 09359648. doi: 10.1002/adma.200702219. URL http://onlinelibrary.wiley.com/doi/10.1002/adma.200702219/abstract.

[68] Anthony Centeno, Jonathan Breeze, Badar Ahmed, Hari Reehal, and Neil Alford. Scattering of light into silicon by spherical and hemispherical silver nanoparticles. *Opt. Lett.*, 35(1):76–78, Jan 2010. doi: 10.1364/OL.35.000076. URL http://ol.osa.org/abstract.cfm?URI=ol-35-1-76.

[69] K. R. Catchpole and S. Pillai. Absorption enhancement due to scattering by dipoles into silicon waveguides. *Journal of Applied Physics*, 100(4):044504, 2006. doi: http://dx.doi.org/10.1063/1.2226334. URL http://scitation.aip.org/content/aip/journal/jap/100/4/10.1063/1.2226334.

[70] K. R. Catchpole and A. Polman. Design principles for particle plasmon enhanced solar cells. *Applied Physics Letters*, 93(19):191113, 2008. ISSN 00036951. doi: 10.1063/1.3021072. URL http://link.aip.org/link/APPLAB/v93/i19/p191113/s1&Agg=doi.

[71] Cayley. A theorem in spherical trigonometry. *Proceedings of the London Mathematical Society*, s1-11(1):48–51, November 1879. ISSN 0024-6115, 1460-244X. doi: 10.1112/plms/s1-11.1.48. URL http://plms.oxfordjournals.org/content/s1-11/1/48.full.pdf+html.

[72] William H Southwell. Gradient-index antireflection coatings. *Optics letters*, 8(11):584–586, 1983.

[73] JA Dobrowolski, Daniel Poitras, Penghui Ma, Himanshu Vakil, and Michael Acree. Toward perfect antireflection coatings: numerical investigation. *Applied optics*, 41(16):3075–3083, 2002.

[74] Daniel Poitras and JA Dobrowolski. Toward perfect antireflection coatings. 2. theory. *Applied optics*, 43(6):1286–1295, 2004.

[75] Yi-Ruei Lin, KY Lai, Hsin-Ping Wang, and Jr-Hau He. Slope-tunable si nanorod arrays with enhanced antireflection and self-cleaning properties. *Nanoscale*, 2(12):2765–2768, 2010.

[76] Yi-Ruei Lin, Hsin-Ping Wang, Chin-An Lin, and Jr-Hau He. Surface profile-controlled close-packed si nanorod arrays for self-cleaning antireflection coatings. *Journal of applied physics*, 106(11):114310, 2009.

[77] Hsin-Ping Wang, Kun-Yu Lai, Yi-Ruei Lin, Chin-An Lin, and Jr-Hau He. Periodic si nanopillar arrays fabricated by colloidal lithography and catalytic etching for broadband and omnidirectional elimination of fresnel reflection. *Langmuir*, 26(15):12855–12858, 2010.

[78] Edward D. Palik. *Handbook of Optical Constants of Solids*. Academic Press, November 1997. ISBN 0125444257.

[79] W Q Xie, J I Oh, and W Z Shen. Realization of effective light trapping and omnidirectional antireflection in smooth surface silicon nanowire arrays. *Nanotechnology*, 22:065704, February 2011. ISSN 0957-4484, 1361-6528. doi: 10.1088/0957-4484/22/6/065704. URL http://iopscience.iop.org/0957-4484/22/6/065704.

[80] Jonathan Grandidier, Dennis M Callahan, Jeremy N Munday, and Harry A Atwater. Light absorption enhancement in thin-film solar cells using whispering gallery modes in dielectric nanospheres. *Adv. Mater.*, 23(10):1272–1276, March 2011. ISSN 1521-4095.

[81] Jin-Young Jung, Zhongyi Guo, Sang-Won Jee, Han-Don Um, Kwang-Tae Park, and Jung-Ho Lee. A strong antireflective solar cell prepared by tapering silicon nanowires. *Optics Express*, 18(S3):A286–A292, 2010. doi: 10.1364/OE.18.00A286. URL http://www.opticsexpress.org/abstract.cfm?URI=oe-18-103-A286.

[82] Baomin Wang and Paul W Leu. Enhanced absorption in silicon nanocone arrays for photovoltaics. *Nanotechnology*, 23(19):194003, 2012.

[83] Linyou Cao, Justin S. White, Joon-Shik Park, Jon A. Schuller, Bruce M. Clemens, and Mark L. Brongersma. Engineering light absorption in semiconductor nanowire devices. *Nat Mater*, 8(8):643–647, 2009. ISSN 1476-1122. doi: 10.1038/nmat2477. URL http://dx.doi.org/10.1038/nmat2477.

[84] Baomin Wang, Erica Stevens, and Paul W Leu. Strong broadband absorption in GaAs nanocone and nanowire arrays for solar cells. *Optics Express*, 22(S2):A386–A395, 2014. URL http://www.opticsinfobase.org/oe/abstract.cfm?uri=oe-22-102-A386.

[85] Ningfeng Huang, Chenxi Lin, and Michelle L. Povinelli. Broadband absorption of semiconductor nanowire arrays for photovoltaic applications. *Journal of Optics*, 14(2):024004, February 2012. ISSN 2040-8986. doi: 10.1088/2040-8978/14/2/024004. URL http://iopscience.iop.org/2040-8986/14/2/024004.

[86] Baomin Wang and Paul W. Leu. Tunable and selective resonant absorption in vertical nanowires. *Optics Letters*, 37(18):3756–3758, September 2012. URL http://ol.osa.org/abstract.cfm?URI=ol-37-18-3756.

[87] Allan W Snyder and J Love. *Optical waveguide theory*, volume 190. Springer, 1983.

[88] John D. Joannopoulos, Steven G. Johnson, Joshua N. Winn, and Robert D. Meade. *Photonic Crystals: Molding the Flow of Light*. Princeton University Press, 2 edition, February 2008. ISBN 0691124566.

[89] D. M. Schaadt, B. Feng, and E. T. Yu. Enhanced semiconductor optical absorption via surface plasmon excitation in metal nanoparticles. *Appl. Phys. Lett.*, 86(6):063106, 2005. ISSN 00036951.

[90] S. Pillai, K. R. Catchpole, T. Trupke, and M. A. Green. Surface plasmon enhanced silicon solar cells. *J. Appl. Phys.*, 101(9):093105, 2007. ISSN 00218979.

[91] Wei Wang, Shaomin Wu, Kitt Reinhardt, Yalin Lu, and Shaochen Chen. Broadband light absorption enhancement in Thin-Film silicon solar cells. *Nano Lett.*, 10(6):2012–2018, June 2010.

[92] Ragip A Pala, Justin White, Edward Barnard, John Liu, and Mark L Brongersma. Design of plasmonic thin-film solar cells with broadband absorption enhancements. *Adv. Mater.*, 21(34):3504–3509, September 2009. ISSN 1521-4095.

[93] Tongchuan Gao, Erica Stevens, Jung kun Lee, and Paul W. Leu. Designing metal hemispheres on silicon ultrathin film solar cells for plasmonic light trapping. *Opt. Lett.*, 39(16):4647–4650, Aug 2014.

[94] Vivian E. Ferry, Luke A. Sweatlock, Domenico Pacifici, and Harry A. Atwater. Plasmonic nanostructure design for efficient light coupling into solar cells. *Nano Lett.*, 8 (12):4391–4397, 2008.

[95] Solar spectral irradiance: Air mass 1.5. URL http://rredc.nrel.gov/solar/spectra/am1.5/.

[96] Yuankun Lin, David Rivera, and KP Chen. Woodpile-type photonic crystals with orthorhombic or tetragonal symmetry formed through phase mask techniques. *Optics express*, 14(2):887–892, 2006.

[97] Zsolt Poole, Di Xu, Kevin P Chen, Isai Olvera, Kris Ohlinger, and Yuankun Lin. Holographic fabrication of three-dimensional orthorhombic and tetragonal photonic crystal templates using a diffractive optical element. *Applied Physics Letters*, 91(25): 251101, 2007.

[98] Xian-Shi Lin and Xu-Guang Huang. Tooth-shaped plasmonic waveguide filters with nanometeric sizes. *Optics Letters*, 33(23):2874–2876, December 2008. doi: 10.1364/OL.33.002874. URL http://ol.osa.org/abstract.cfm?URI=ol-33-23-2874.

[99] A.V Shah, J Meier, E Vallat-Sauvain, N Wyrsch, U Kroll, C Droz, and U Graf. Material and solar cell research in microcrystalline silicon. *Solar Energy Materials and Solar Cells*, 78(1â??):469 – 491, 2003. ISSN 0927-0248. doi: http://dx.doi.org/10.1016/S0927-0248(02)00448-8. URL http://www.sciencedirect.com/science/article/pii/S0927024802004488. Critical review of amorphous and microcrystalline silicon materials and solar cells.

[100] D. Amans, S. Callard, A. Gagnaire, J. Joseph, G. Ledoux, and F. Huisken. Ellipsometric study of silicon nanocrystal optical constants. *Journal of Applied Physics*, 93(7):4173–4179, 2003. doi: http://dx.doi.org/10.1063/1.1538344. URL http://scitation.aip.org/content/aip/journal/jap/93/7/10.1063/1.1538344.

[101] Baomin Wang and Paul W. Leu. High index of refraction nanosphere coatings for light trapping in crystalline silicon thin film solar cells. *Nano Energy*, 13(0):226 – 232, 2015. ISSN 2211-2855.

[102] Baomin Wang, Tongchuan Gao, and Paul W Leu. Broadband light absorption enhancement in ultrathin film crystalline silicon solar cells with high index of refraction nanosphere arrays. *Nano Energy*, 19:471 – 475, 2016. ISSN 2211-2855. doi: http://dx.doi.org/10.1016/j.nanoen.2015.10.039. URL http://www.sciencedirect.com/science/article/pii/S2211285515004188.

[103] Shuang Wang, Benjamin D. Weil, Yanbin Li, Ken Xingze Wang, Erik Garnett, Shanhui Fan, and Yi Cui. Large-area free-standing ultrathin single-crystal silicon as processable materials. *Nano Lett.*, 13(9):4393–4398, 2013.

[104] Geon Dae Moon, Tae Il Lee, Bongsoo Kim, GeeSung Chae, Jinook Kim, SungHee Kim, Jae-Min Myoung, and Unyong Jeong. Assembled monolayers of hydrophilic particles on water surfaces. *ACS Nano*, 5(11):8600–8612, 2011.

[105] Xiaoyan Ma, Jun Q Lu, R Scott Brock, Kenneth M Jacobs, Ping Yang, and Xin-Hua Hu. Determination of complex refractive index of polystyrene microspheres from 370 to 1610 nm. *Phys. Med. Biol.*, 48(24):4165, 2003.

[106] James M. Ball, Samuel D. Stranks, Maximilian T. Horantner, Sven Huttner, Wei Zhang, Edward J. W. Crossland, Ivan Ramirez, Moritz Riede, Michael B. Johnston, Richard H. Friend, and Henry J. Snaith. Optical properties and limiting photocurrent of thin-film perovskite solar cells. *Energy Environ. Sci.*, 8:602–609, 2015.

[107] Tongchuan Gao, Baomin Wang, Bo Ding, Jung-kun Lee, and Paul W. Leu. Uniform and ordered copper nanomeshes by microsphere lithography for transparent electrodes. *Nano Letters*, 14(4):2105–2110, 2014. doi: 10.1021/nl5003075. URL http://pubs.acs.org/doi/abs/10.1021/nl5003075.

[108] Shuang Wang, Benjamin D. Weil, Yanbin Li, Ken Xingze Wang, Erik Garnett, Shanhui Fan, and Yi Cui. Large-area free-standing ultrathin single-crystal silicon as processable

materials. *Nano Letters*, 13(9):4393–4398, September 2013. ISSN 1530-6984. doi: 10.1021/nl402230v. URL http://dx.doi.org/10.1021/nl402230v. 00001.

[109] Xin He, Ruihui He, A'lei Liu, Xiangyuan Chen, Zhilong Zhao, Sheng Feng, Ning Chen, and Mei Zhang. A highly conductive, flexible, transparent composite electrode based on the lamination of silver nanowires and polyvinyl alcohol. *J. Mater. Chem. C*, 2: 9737–9745, 2014. doi: 10.1039/C4TC01484G. URL http://dx.doi.org/10.1039/C4TC01484G.